HATRX: a new method for time-resolved structural studies

Briony Alissa Yorke

Submitted in accordance with the requirements for the degree of

Doctor of Philosophy

The University of Leeds

Faculty of Biological Sciences

May 2014

“The candidate confirms that the work submitted is his/her own, except where work which has formed part of jointly authored publications has been included. The contribution of the candidate and the other authors to this work has been explicitly indicated below. The candidate confirms that appropriate credit has been given within the thesis where reference has been made to the work of others.”

Chapter 2

Dr. Robin Owen and Professor Arwen Pearson provided the spectroscopic data recorded from thin films of horse myoglobin, bovine cytochrome *c* and crystals of horse cytochrome *c*. The sample preparation and data collection are described in sections 2.3.1 and 2.3.2. All data analysis was performed by myself and is described in section 2.3.3.

The work described in this chapter has been published in the following paper: Owen, R.L., Yorke, B.A., Gowdy, J.A., Pearson, A.R., (2011) Revealing low dose radiation damage using single crystal spectroscopy, *J. Synch. Rad*., **18** 367-373

Chapter 3

Dr. Robin Owen and Professor Arwen Pearson constructed the spectrophotometers that were used in these experiments and collected initial spectral data on the test proteins and cryoprotectants. During subsequent beamtimes I then collected the rest of the data presented in this chapter. I performed the spectroscopic data processing and analysis described in this chapter and Dr Owen analysed the diffraction data.

The work described in this chapter has been published in the following paper: Owen, R.L., Yorke, B.A. & Pearson, A.R. (2012) X-ray excited optical luminescence of protein crystals: a new tool for studying radiation damage during diffraction data collection. *Acta Cryst.* **D68** 505-510

Chapter 4

Dr Michael Webb designed the nitrobenzyl-aspartate photocage. The photocage synthesis, protein production, crystallization and structure determination described in this chapter are entirely my own work. I also refined the structure of the T57V ADC mutant described in the introduction which has been published in the following paper: Webb, M.E., Yorke, B.A., Kershaw, T., Lovelock, S., Lobley, C.M.C., Kilkenny, M.L., Smith, A.G., Blundell, T.L., Pearson, A.R., Abell, C. (2014) Threonine 57 is required for the post-translational activation of *Escherichia coli* aspartate α-decarboxylase. *Acta Cryst.* **D70** 1166-1172

Chapter 5

The original suggestion of applying Hadamard transforms to time-resolved experiments was made by Prof. G.S. Beddard. I proposed the use of this method for time-resolved X-ray crystallography and demonstrated its application. Dr R.L. Owen and Prof. A.R. Pearson assisted with data collection and processing.

This work has been accepted for publication in Nature Methods: Yorke, B.A, Beddard, G.S., Owen, R.L., Pearson, A.R. (2014) A new approach to time-resolved X-ray crystallography: removing flux limitations using the Hadamard Transform. *Nature Methods. In press.*

Acknowledgements

I have a rather considerable number of people to thank, so I will start at the beginning. Thank you to Professor Beddard, without his mentorship I would have not even begun the voyage into scientific research, and certainly never come across the Hadamard transform, which has come to play a central role in our research. He has set a fine example through his enthusiasm, stoicism and good humour. Another inspiring example of enthusiasm is my friend, confidant and of course scientific superior, Prof. Dr. Arwen Pearson. Her energy has been contagious and vital on those long nights at the beamline. I can't imagine there is anyone else in the world that could engage me in a discussion about crystallography after a 24-hour synchrotron shift followed by a transatlantic flight. I have to admit that I probably fall into the category of 'nightmare student', however, Arwen's support has been unwavering and under her guidance I have been given the skills and freedom to develop my own ideas, including my little side project. I long to one day have an opportunity to pass on the baton that I feel Prof. Dr. Pearson has passed to me. Dr. Robin Owen's humour has also kept us going during those long data collections, he is an outstanding beamline scientist and without his knowledge (and connections) this project would not have been possible. His willingness to take the time to explain complex ideas and his patience has not gone unappreciated. Dr. Michael Webb's influence in this project has mainly been through his ability to instantly understand any problem thrown at him, and not be shy about offering solutions. Again, I think I need to mention patience, thanks Mike! I must also offer my thanks to all of the beamline scientists that have trusted us to do things a little differently, especially those on i24 at Diamond Light Source. I would also like to thank my family. Mum and Dad, you always wanted me to do my best, I hope that you can see that I really have tried to make you proud. Finally, Bella and Bod, this has been quite a journey. Your willingness to stick with it, through everything, is astounding. I love you

both more than I ever realised was possible and I will do everything I can to make sure it was worth it.

Abstract

Structural biology aims to elucidate the relationship between the function of biological molecules and their structure. In addition, time-resolved methods are used to characterise the contribution of structural dynamics to biological processes, such as protein folding, force transfer, ligand binding and catalysis.

Numerous time-resolved methods are available, with each being particularly suitable for the study of different set of biological processes. To observe the structural and chemical changes accompanying enzyme catalysis it is necessary to use techniques that combine atomic spatial resolution with fast-time resolution, such as X-ray crystallography. Time-resolved X-ray crystallographic methods have existed for several decades, but are not widely used. A major challenge is the need for an X-ray source that is bright enough to provide a measurable signal in very short times. Laue crystallography can be used to reach 100s of pico-second time-resolutions, however, at fast time-scales, this method is only applicable to reversible reactions. More recently the use of free-electron lasers has been proposed .to directly observe atomic positions in proteins with femto-second time-resolution. However, these experiments require the use of a free-electron laser, an expensive and limited resource. A more general approach is therefore needed to perform time-resolved crystallography on irreversible systems and increase the achievable time-resolution using flux-limited, but widely available monochromatic synchrotron beamlines,

Here we propose a novel application of the Hadamard transform to time-resolved experiments and demonstrate its use for X-ray crystallography by measuring the X-ray induced breaking of the eight disulfide bonds of thaumatin. The technique is applicable to a range of diffraction and spectroscopic methods, where the probe can be

encoded. The use of the Hadamard transform increases the achievable time-resolution of a time-resolved experiment using a monochromatic synchrotron beamline by orders of magnitude, enabling the observation of short-lived intermediate species in chemical and biological reactions. This will provide unprecedented information regarding the relationship between structure and function.

Table of contents

Glossary

MX – Macromolecular crystallography

ADC - L-Aspartate α-decarboxylase

NZD – o-Nitrobenzyl-L-aspartate

PYR – Pyruvoyl group

IMN – Imminium intermediate

PDB– Protein Data Bank

NMR – Nuclear Magnetic Resonance

LC-MS – Liquid Chomatography Mass Spectrometry

EPR – Electron Paramagnetic Resonance

HATRX – Hadamard transform time-resolved X-ray crystallography

SVD – Singular value decomposition

SAXS – Small-angle X-ray scattering

DLS - Diamond light source, Harwell

SRS – Synchrotron Radiation Source, Daresbury

APS – Advanced Photon Source, Chicago

ESRF – European Synchrotron Radiation Facility, Grenoble

LCLS – Linear Coherent Light Source

SLAC – Stanford Linear Accelerator Center

Amino acid three letter codes

Ala – alanine

Arg – arginine

Asn – asparagine

Asp – aspartic acid

Cys – cysteine

Glu – glutamine

Gly – glycine

His – histadine

Ile – isoleucine

Lys – lysine

Met – methionine

Phe – phenylalanine

Pro – proline

Ser – serine

Thr – threonine

Trp – tryptophan

Tyr – tyrosine

Val – valine

Chapter 1 Introduction

Over the last sixty years structural biology has provided a wealth of information that has led to a greater understanding of the way biological structures are related to function. Electron microscopy (EM), nuclear magnetic resonance (NMR) and X-ray crystallography are routinely used to determine the structure of biological macromolecules, each technique providing specific advantages over the others. One shortcoming pertinent to the traditional application of all EM and X-ray crystallography approaches is that they provide "static" images of the structure in a single time-averaged ensemble conformation. This level of detail is not sufficient when probing the details of biological mechanisms, as it is the functionally related motions of biological macromolecules that enable them to control the energy landscapes of chemical reactions. Without observing how these systems change with time, we cannot truly understand the primary processes underlying life. The time-scales of biological mechanisms range from femtoseconds to hours and so it is desirable to be able to probe them using techniques with time-resolutions that cover this entire range. Time-resolved experiments have been carried out using all of the aforementioned techniques[1–9], however, technical limitations have precluded them from general use. This thesis focuses on the development of time-resolved X-ray crystallography as a method for obtaining 'real-time' structural information with atomic resolution.

1.1 Historical Perspective

In 1957 Max Perutz and John Kendrew determined the first high-resolution protein structures of myoglobin and haemoglobin[10]. They and other pioneers in the field realised it was necessary to prove that the crystalline structure of proteins is biologically relevant, if the structures they were determining were to provide insight into biological function[11–13]. Richards and Doscher's approach to this problem was to use spectroscopy to analyse the catalytic activity of enzymes when in the crystalline state and compare this to the solution state. The rate of hydrolysis of uridine and cytidine 2',3'-phosphate by crystalline and

solution state Ribonuclease S* was measured spectrophotometrically and revealed that the enzyme was still active in the crystalline state, although the kinetics were slightly altered.

The combination of spectroscopy and crystallography to analyse the relationship between structure and function was pivotal in the development of time-resolved X-ray crystallography. At this time, time-resolved spectroscopy was well established in the chemical and biological sciences. It was frequently used in the study of enzyme kinetics and pump-probe spectroscopy had been used to measure the formation and decay of short-lived intermediates in chemical reactions[14–18]. The desire to observe the structure of these transient species was an obvious progression, however, in the late 1960s the intensity of X-ray sources was such that a full dataset could take weeks to record. In 1969 Keith Moffat concluded that it would be impossible, with the technology available at the time, to perform time-resolved crystallography using similar methods to those developed for spectroscopy[19]. Collecting diffraction data requires the crystal to be rotated in the beam over a minimum angle determined by the space group of the crystal. This means that the time-resolution is limited, not by the time of a single exposure, but by the total time of all exposures required during rotation of the crystal. Instead, it was more sensible to try to determine the structure of reaction intermediates by increasing their lifetime using a variety of methods including cryo-trapping[20,21], 'pseudo-substrates'[22,23] or mutagenesis[24,25]. The symbiosis between spectroscopy and X-ray crystallography still exists. Crystallography provides a structural link between the indirect time-resolved observations made using spectroscopy and the changes observed in chemical and biological crystals, and time-resolved spectroscopy has been used to analyse changes in crystals as they are exposed to X-radiation[26-29].

1.1.1 Cryo-trapping

Once it was established that enzymatic activity was preserved in the crystal and that the reaction rates were not necessarily affected by

crystallization but rather by the accessibility of the active site to the substrate through solvent channels and changes in conformation during turn-over[11,27,28], it became apparent that it would be possible to determine the structures of intermediate species. As intermediate species in enzymatic reactions generally have lifetimes far shorter (ps – s) than the time it would take to collect a full dataset from pre-synchrotron X-ray sources (from days to weeks), the first experiments aimed to elucidate active "substrate-enzyme" complexes from stable complexes of the enzyme with an inhibitor or "pseudo-substrate". Douzou *et al.*[29] realised that, although relatively long-lived intermediate species (ms – s) could not be observed by contemporary X-ray crystallographic experiments, their lifetime could be increased by lowering the temperature according to the Arrhenius equation (1.1)

$$k = Ae^{-\frac{E_a}{RT}} \qquad (1.1)$$

The relationship between the rate constant and temperature is such that if the temperature is lowered the rate constant decreases and so the lifetime of the intermediates must also increase. To test this hypothesis it was necessary to develop solvents that would remain liquid upon cooling and also not interfere with the enzymatic reaction. Using such solvents Douzou *et al*.[29] were able to show that, in the case of lysozyme hydrolysis of bacterial cell walls, the lifetime of the enzyme-substrate complex was increased by 3 orders of magnitude when cooled from 300 to 175 K. They postulated that with the development of suitable crystal cooling systems this method would easily transfer to X-ray crystallography, enabling the structure of reactive intermediates to be determined. In 1976, crystal cooling was used to trap the enzyme-substrate complex of γ-chymotrypsin with its substrate acetyl-L-tryptophan-*p*-nitrophenyl ester[30] and the structure of the enzyme-substrate intermediate of elastase with the N-carboxybenzoxy-L-alanyl-*p*-nitrophenyl ester was also solved[31].

This technique is now widely known as cryo-trapping[32]. The time-resolution is limited by the time between reaction initiation (diffusion of

the substrate into the crystal)[33] and flash-cooling (ms – s)[34,35]. Therefore, although the structures of some intermediates can be determined in this way, the time- resolution is not fast enough to capture all intermediates along the reaction pathway, nor can it be used to probe protein dynamics during enzymatic reactions.

1.1.2 Synchrotron Radiation and the birth of time-resolved crystallography

Due to the complexity of proteins it is necessary to use structural techniques in order to fully understand their function, this cannot be achieved using the indirect spectroscopy which provides only local structural information, or sparse distance data. The changes in protein structure and the dynamics accompanying the formation and decay of intermediate structures must be determined in order to unambiguously determine the relationship between structure and function. The development of synchrotron radiation has provided crystallographers with increasingly higher intensity X-ray beams, resulting in shorter data collection times and making the idea of time-resolved crystallography more feasible than ever before. Bartunik *et al*[36]*.* provided the first proof-of-principle data for pump- probe crystallography by investigating the rebinding of CO to myoglobin after laser dissociation. A time-resolution of 500 μs was achieved by recording a single frame of data at a linear selection of time points after laser initiation and analysing the intensity of just three reflections. They showed, by analysing the change in intensity of these reflections, that the rebinding of CO occurred in 3 milliseconds and concluded that, with improvements in the detectors used for these studies, it would be possible to collect time-resolved X-ray diffraction data[36].

The feasibility of these proof-of-principle experiments was entirely dependent on the higher intensities provided by synchrotron radiation. The introduction of the second generation of synchrotron sources (SRS, Daresbury[37] and CHESS, Cornell[38]) transformed time-resolved X-ray crystallography from a technique limited to the observation of long lived intermediate states, trapped in their conformation by cooling, to a way of observing atomic motion in real-time. The intensity of the X-ray beam was increased by three orders of magnitude (from 10^{12} to 10^{15} photons s^{-1} m^{-2}) and the collection time of a full crystallographic dataset was reduced from days to hours. In their 1982 review of the uses of synchrotron radiation in molecular biology, John Helliwell and

Trevor Greenhough[39] discussed how the increase in intensity should enable the determination of multiple intermediate structures along the reaction pathway from the same crystal. They also envisioned how B-factor analysis[40] could be used to investigate changes in protein dynamics at different points along reaction co-ordinate. However, although changes in the crystal could be observed using changes in the intensity of diffraction on microsecond timescales[30], it still required hours to obtain a full structural dataset.

The answer was to change the way X-ray diffraction data were collected. In 1984 Keith Moffat showed that, by using a polychromatic X-ray beam, the exposure time required to collect a frame of data could theoretically be reduced from 1 s deg^{-1} (as the crystal must be oscillated during monochromatic X-ray data collection) to 120 ps deg^{-1}, theoretically increasing the time-resolution by 11 orders of magnitude[41,42].

1.1.3 The Laue pump-probe method

The first X-ray diffraction experiment was designed by von Laue and was carried out by Friedrich and Knipping in 1912[43]. The Laue experiment consisted of recording diffraction images using polychromatic radiation and a stationary crystal. The use of monochromatic X-radiation was developed later by Bragg to overcome the limitations of the Laue method caused by the low intensity of polychromatic radiation sources[44]. Synchrotron electron beams, however, emit a high flux of X-ray photons with a broad range of wavelengths[45], and so with the introduction of synchrotron radiation came a revival of interest in the Laue method. The Laue data collection method was designed to overcome the limited time resolutions available due to the photon flux of X-ray sources. The time needed to deliver enough photons to produce a measureable signal from monochromatic X-radiation was on the order of milliseconds for 2nd generation synchrotron sources, and so the time-resolution of these experiments was limited to milliseconds[41]. Using polychromatic X-radiation utilises more of the X-ray photons emitted from the electron

beam and therefore results in a much higher useable photon flux. Collecting multiple wavelengths also removes the need to oscillate the crystal to sample the whole of the Bragg peak, and this further reduces the time required to collect a single frame of data.

The first Laue experiments by Keith Moffat at CHESS, using conventional X-ray detectors, resulted in single Laue diffraction images of haemoglobin recorded with exposures as short as 10 milliseconds[46]. Hadju *et. al.*[47] produced the first definitive time-resolved results using the Laue method to analyse maltoheptose binding to phosphorylase *b*. The time resolution was on the order of milliseconds and the reaction was initiated using a flow cell to introduce the substrate to the enzyme crystal[47]. These experiments showed that with further developments in detectors and synchronization between the pump and probe it could be possible to record structural data with time-resolutions as fine as 100 picoseconds. This triggered a slew of technical developments focused on making the theoretical experiment a reality.

1.1.3.1 Photoactivation, timing control and detectors

The structures obtained from X-ray diffraction experiments are averaged over the time taken to collect the data and also over all the molecules in the crystal. When observing the formation of intermediates it is therefore important that the initiation of the reaction occurs at the same time in every molecule in the crystal. If initiation is slower than the rate of reaction, then the structure obtained will be the average of a large distribution of states. To initiate a reaction by diffusion-limited processes, *i.e.* flowing a ligand solution through the crystal[44,48] is only appropriate in systems where the intermediate of interest has a half-life of over 10 minutes[45]. When trying to obtain time-resolved structures with a time-resolution of ~100 picoseconds it is necessary to initiate the reaction within this timescale. The only way to achieve this is by photoactivation[6]. Laser pulses of length < 1 picosecond are readily available and so photoactive reactions have made up the bulk of systems studied by time-resolved crystallography (see table 1.1).

Light initiation is not without limitations. Visible light is scattered from the surface of the crystal and protein molecules absorb light in the UV region, so the penetration depth of a laser into a crystal is significantly lower than the penetration of an X-ray beam[45]. When using a large single crystal, a compromise must be made between light absorption and diffraction intensity. Another limitation is the quantum yield of the photoactivatable reaction. The absorption of a photon may not result in the desired reaction but instead cause damage to the crystal. If the quantum yield is too low, light activation is unfeasible. Most enzymatic reactions are not photoactive and so photocaged substrates and amino acids are required. The development and synthesis of photocaged compounds is non-trivial and since the uncaging event is generally a dark-process which proceeds after light initiated isomerization, the speed of the initiation is slow when compared to naturally photosensitive systems, limiting achievable time-resolutions[49–53].

Macromolecular System	Timescales
Myoglobin	100 ps - 3 ms[54–60]
Photoactive yellow protein	150 ps – 1 s[63–72]
Photosynthetic reaction centre	3 ms[71,72]
Haemoglobin	100 ps – 80 μs[73]
3-isopropylmalate dehydrogenase	40 ms[74]
FixL	1 μs – 10 ms[75]
Trypsin	10 ms – 1s[76]
Isocitrate dehydrogenase	10 ms [7]
Dehaloperoxidase haemoglobin	100 ps [77]

Table 1.1 : Summary of sub-second time-resolved Laue experiments

When carrying out a time-resolved experiment it is important to know the time separation between initiation and activity to a level of accuracy beyond the time-resolution of the experiment. The synchronization of laser and X-ray beams was achieved by designing fast shutters capable of isolating X-ray pulses from a single electron bunch in the synchrotron storage ring and designing triggering schemes to link the laser and X-ray shutters to the detector initialization[78,79].

The speed and quality of the X-ray detector is another limiting factor in time-resolved experiments. The readout time limits how many structures along the course of the reaction scheme can be measured in a single run of the experiment and the noise level of the detector (which includes point spread function and background) determines how many times a diffraction image has to be recorded to obtain a

useable signal-to-noise ratio. The development of charge-coupled devices (CCD) provided faster readout times than image plates, however, the high background of these detectors and resulting poor signal-to-noise ratio meant that many diffraction images had to be collected at each time point along the reaction co-ordinate, lengthening the time required to collect a full dataset but not necessarily affecting the time-resolution of the experiment. The PILATUS[80,81] photon counting detector is essentially noiseless and so the number of photons required to produce a recordable signal is reduced.

1.1.3.2 Data collection strategy

The pump-probe data collection method was designed to account for the limited photon flux produced by second-generation synchrotron X-ray sources.[39,42] The general methodology imposes limitations on which systems can be studied. In a pump-probe experiment the reaction is initiated in the crystal using a short laser pulse and, after a well-defined time-delay, a diffraction image is collected from a single crystal, which is held stationary during data collection. The system is allowed to relax back to its starting state and the crystal is rotated, the reaction is initiated again and diffraction data are collected from the new orientation. This is repeated until enough data has been collected to determine a structure. The number of repeats at a single time-point depends on the space group (the angular range of reciprocal space that must be sampled) and the diffraction quality of the crystals (the signal-to-noise ratio of diffraction data). The experiment is then repeated for each time point along the reaction co-ordinate until a full time-resolved dataset has been collected.

The limitations associated with this strategy are:

1. The reaction being probed must be reversible - structural data for each intermediate is collected from as few crystals as possible to avoid noise associated with non-isomorphism.
2. The system must be radiation hard – each crystal is exposed to a large dose during the data collection and the experiment is carried out above 100 K to allow the reaction to proceed. This

has the unfortunate side effect of allowing both primary and secondary radiation damage to occur[82,83].

Processing Laue data is not as straight forward as monochromatic data, many stages require specialist knowledge and are not as well automated as normal crystallographic data processing. The use of multiple wavelengths introduces the problem of overlapping reflections that must be deconvolved during indexing. Auto-indexing programs exist to assist with this process[84,85], however, datasets are still often indexed by hand. Since high intensity pulses are used to collect large wedges of data from single crystals, at room temperature, the effects of radiation damage must be carefully considered during data processing.

Despite these limitations the pump-probe Laue method used at the European synchrotron radiation facility (ESRF, Grenoble) and Advanced Photon Source (APS, Chicago) has provided unprecedented information about the mechanism and dynamics of a number of proteins. Table 1 contains an overview of systems that have been probed at sub-second time-resolutions using the Laue diffraction method. Data processing is based on the comparison of difference Fourier maps. The functionally related changes in structure are extracted using principal component analysis and the time-dependent trajectories and time-independent structural data are differentiated using singular value decomposition (SVD)[63,86,87].

1.1.4 Radiation Damage

When a protein crystal of thickness 100 μm is placed into the path of a 12.4 keV X-ray beam, only 2% of the incident X-rays interact with the crystal[83]. The photoelectric effect accounts for most of the interaction (85%) and this is the major cause of radiation damage in protein crystals. An atomic electron absorbs the total photon energy and the electron is ejected from the atom. This solvated photoelectron can then interact with other atoms in the crystal, causing further ionisation and secondary radiation damage. Compton (inelastic) scattering accounts

for 7.5% of the interaction, here a portion of the photon energy is deposited into the crystal via an interaction with an atomic electron, causing the scattered photon to be lower in energy and the energy to be deposited in the crystal, again resulting in damage. Only 0.15% of the incident X-rays are scattered elastically (with no energy deposited in the crystal) and it is these photons that produce the diffraction pattern[88].

The effect of radiation damage is most commonly observed as a decrease in the total diffraction intensity from a crystal. This is thought to be due to structural changes occurring which propagate disordered regions though the crystal, resulting in a reduction in the number of diffracted photons[89]. The formation of hydrogen gas, by the cleavage of C-H bonds has also been attributed to the propagation of damage, it is thought that the presence of gas bubbles trapped in the crystal causes the unit cell dimensions to increase[90], although primary ionisation events still occur.

When data collection is carried out at room temperature radiation damage can prevent the collection of complete datasets from single crystals. With the advent of high-powered synchrotron sources in the early 1990s, cryocooling of samples gained popularity[91–96]. Collecting data at 100 K, slows down the effects of radiation damage by preventing the diffusion of radical species through the crystal[83].

The highly reactive radical species are formed by three processes: i) when a photoelectron is ejected from an atom due to the absorption of an X-ray, ii) when the liberated photoelectron interacts with an atom and iii) when a radical formed in the solvent diffuses through the crystal and interacts with an atom[83]. Cryocooling does not completely prevent radiation damage, even at 100 K the solvated electrons can tunnel along the protein backbone causing site-specific damage.[97] Specific damage occurs in a well-defined order in a protein crystal. First, disulphide bonds are broken. This is followed by the decarboxylation of glutamates and aspartates. Then tyrosine groups lose their hydroxyl groups and, finally, the C-S bonds in methionines

are broken[98–100]. These changes can cause structural changes that may adversely affect the conclusions drawn about biological function. Although the order in which site specific damage occurs is well characterised, the mechanisms leading to this damage are not. To ensure that the structural changes observed during time-resolved experiments are biologically relevant, it is important to understand the mechanisms of radiation damage.

Complementary methods, such as UV-vis absorption[101–103], Raman[104,105], and X-ray spectroscopies[106-109] as well as electron paramagnetic resonance[110] are extremely useful to probe radiation damage and provide detailed insight into the physio-chemical origin of this phenomenon.

1.1.5 The future

Over the past five years there have been major advances in the techniques available to perform time-resolved X-ray crystallography. The major development has been the completion of the Linear Coherent Light Source free electron laser (LCLS, Stanford)[111]. This $420 million facility is the first of its kind to produce X-rays with wavelengths suitable for macromolecular crystallography (down to 1.5 Å). The intensity of the X-ray pulses generated by these machines is up to 10^9 times higher than those produced by modern synchrotrons, producing 10^{13} photons within tens of femtoseconds[112]. The high flux of the source means that within a few femtoseconds sufficient X-rays can be diffracted from nanocrystals to produce a useable diffraction pattern. In addition to this, a surprising consequence of using such a high intensity X-ray beam is that the effects of radiation damage can be completely avoided[113]. Although the protein crystals are completely destroyed in the high intensity beam, the diffraction pattern is produced so quickly that radiation damage is not observed in the data. The time-resolution of the experiment 'out-runs' radiation damage.

The first demonstration of a X-ray free electron laser (XFEL) time-resolved experiment sprayed a nanocrystalline slurry through a small

nozzle to produce a jet[114]. First the jet was passed through a laser beam to initiate the reaction, and then through the path of the X-ray beam. The XFEL beam is pulsed, with the pulse length only a few tens of femtoseconds. When the X-ray pulse is incident on a nanocrystal in the jet, a diffraction pattern is produced. These experiments have opened up the femtosecond time regime to X-ray crystallography, however, there are still many experimental and data processing challenges that need to be addressed.

Due to the difficulty of timing the pulses to the position of crystals in the jet, very few crystals in the jet are actually used; most photons and crystals are wasted. However, as nanocrystals are much easier to produce than high-quality large single crystals this is not considered to be an insurmountable drawback. The nanocrystals are orientated randomly as they pass through the path of the X-rays and so by collecting many single images the whole of reciprocal space can be sampled[115–117]. Due to the nature of this data collection, the crystals cannot be oscillated in the beam and so the Bragg peak is only partially recorded for each reflection.[116] This means it is necessary to construct the total integrated Bragg peak by merging together a large number of images from different crystals with unknown orientational relationship. The crystFEL program suite[118] uses a Monte Carlo method in which the mean of many individual intensities of the same reflection, recorded from a series of crystals, is calculated. This method enables the angular integration of reflections during post-processing of data, without recording full reflections and pre-convoluting angular information into the dataset. However, it requires a very large number of diffraction patterns (10,000s) to be compared in order to estimate the partiality of individual reflections.

This method relies on the use of good model phases in order to successfully solve structures; the Monte Carlo method is not yet capable of determining accurate amplitude measurements. Experimental phasing has been demonstrated for hen egg white lysozyme using a gadolinium derivative[119,120,] however, the data

processing for this simple system was challenging. Major developments in data processing must therefore be implemented before the time-resolved experiment is viable for novel systems.

1.1.6 Modern synchrotron based time-resolved crystallgraphy

Despite the technical limitations of the Laue and serial crystallography methods the major drawback of both methods is the limited availability of beam time at FEL and Laue facilities. Ideally a system should be well characterised and the experimental design complete before attempting data collection in such a limited time frame. To do this, it is beneficial to have access to preliminary time-resolved data. For example, femtosecond time-resolved spectroscopic techniques can be used to elucidate the time-scales on which intermediate chemical species are produced[120].

The main aim of my work has been to develop methodology that is accessible to the wider scientific community (not just X-ray crystallography specialists) that yields fast time-resolved structural data with atomic spatial resolution. It is possible to carry out a synchrotron version of the XFEL serial crystallography time-resolved method, by using many micro-crystals to collect structural data at known time-delays after an initiation event, such as photo-initiation of an enzymatic reaction using a laser pulse, (Figure 1.1). Although similar in concept to XFEL serial crystallography, at a synchrotron the X-ray beam is stable and well defined *and* crystals are held in the beam on a traditional goniometer set-up and can therefore be oscillated during data collection, avoiding the XFEL problem of integrating Bragg peaks recorded from still images. Merging data from many (100-1000) microcrystals, as opposed to collecting as much data as possible from a large single crystal, also provides several practical advantages over the established Laue method. Each crystal is used only once to collect a small amount of structural data from a single time-point. This means that non-reversible reactions can be studied and the radiation absorbed by each crystal is reduced, thus limiting the

radiation damage across the entire dataset. Another advantage of using microcrystals is that the formation of microcrystals is frequently observed during the early stages of identifying crystallisation conditions. Using these for data collection can thus, in some instances, reduce the time required for sample optimisation.

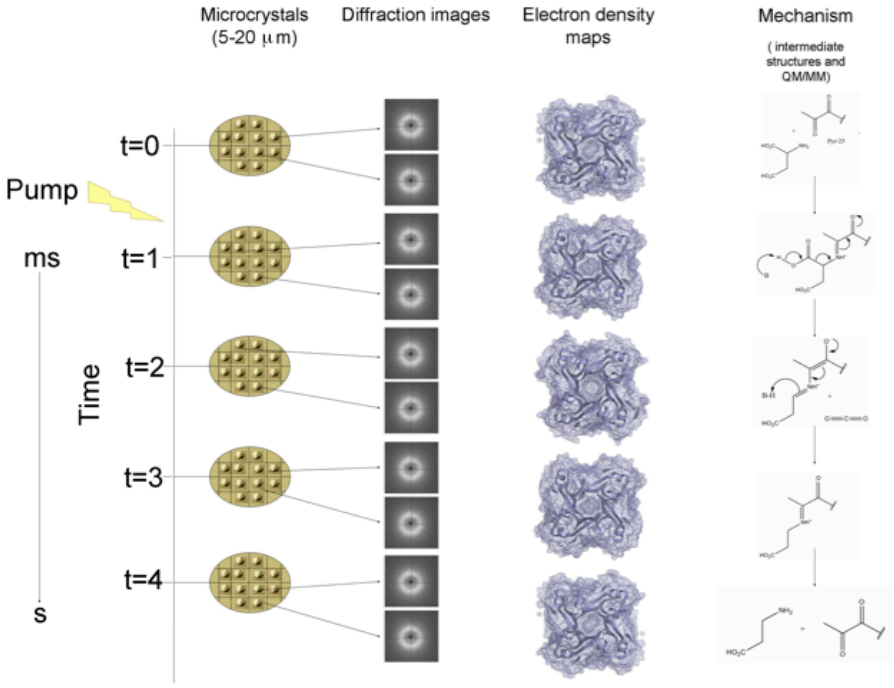

Figure 1.1 Schematic showing the proposed multi crystal method, multiple crystals are mounted using a micromesh, diffraction is measured from each crystal individually and then merged to give a full dataset. The dataset is then processed to give an electron density map, the crystal structures along the reaction pathway can then be used to characterise the enzyme mechanism.

Collecting data from such a large number of microcrystals would not be possible if this method was not developed alongside the improvements in facilities at synchrotron sources. During this project a number of improvements to MX beamlines have resulted in an increase in the speed at which datasets can be collected. The integration of Pilatus detectors has decreased the average time taken to collect a full dataset from the order of minutes to seconds, indeed an image can be acquired in a few milliseconds[121]. Another significant

factor in reducing the time required to collect a multi-crystal datset has been the implementation of sample changing robots. At the I24 beamline at Diamond Light Source the Irelec CATS robot can exchange a sample in 45 seconds, whereas changing a sample by hand requires at the least a few minutes, with an additional delay imposed by the need to secure the hutch before and after each sample change. By reducing the time taken to load samples into the beam and collect data, the major limitation to the amount of data that can be collected during a beamtime shift becomes the sample quality and the time required to identify the position of the crystal and align it in the beam.

Alongside this project, the 'grid scan' method of crystal identification and quality assessment was implemented as an effective way to quickly screen large numbers of microcrystals[122]. This method uses the diffraction of an attenuated X-ray beam to identify the position and quality of microcrystals and is particularly useful for aligning very small crystals (which may be invisible to the online microscope optics) and light sensitive samples. To perform the grid scan and to collect data with minimal background noise the X-ray beam size is matched to the size of the crystal. At the time of starting this project the beam at I24 (DLS) could be focused to 25 × 25 μm (1.5×10^{12} ph s^{-1}). Continuous improvements to the beamline have resulted in a focused beam size of 10 × 10 μm (2×10^{12} ph s^{-1}) and a minimum beam size of 5 × 5 μm (1×10^{11} ph s^{-1}), achieved by slitting down the beam.

1.2 Remaining challenges & scope of this thesis

Despite the advances in X-ray sources and detectors, as well as in protein sample production and characterisation, time-resolved structural experiments remain a niche technique with considerable challenges. At synchrotrons these include the unavoidable radiation damage effects that are always convolved with the recording of functionally related structural changes as well as the flux limitations on

achievable time-resolution. Finally, in any fast time-resolved experiment reaction initiation remains a significant challenge.

This thesis describes investigations into the site-specific radiation damage occurring at low doses (Chapter 2) and the testing of a novel complementary method to monitor radiation damage (Chapter 3). Chapter 4 describes the development of a photocaging strategy for aspartate decarboxylase and initial structural characterisation of both photocage binding and activation as well as demonstrating that multi-microcrystal data do provide sufficiently good data for the identification of light induced changes. Finally, Chapter 5 describes the development and demonstration of a novel approach to time-resolved crystallography that will allow the collection of fast time-resolved data on standard monochromatic synchrotron beamlines, and even in house.

Chapter 2 Revealing low dose radiation damage

2. 1 Introduction

Structural biology aims to provide detailed insight into biological function at the molecular and atomic level. However, in extrapolating from the static average structures obtained from X-ray crystallography, care must be taken to ensure that radiation damage has not affected the structure determined. As soon as a macromolecular crystal is exposed to X-ray radiation, photoelectrons and radicals are formed though the absorption and inelastic scattering of X-ray photons[88]. If an X-ray is absorbed by an atom in the protein molecule the damage is referred to as direct or primary damage. However, solvent molecules surrounding the protein also absorb energy, resulting in the formation of radicals, (Figure 2.1). These highly reactive species diffuse though the crystal causing indirect or secondary damage. The propagation of damage through the crystal causes disorder within the lattice that manifests as a loss in diffraction intensity.

$$H_2O \xrightarrow{\text{Ionizing radiation}} H_2O^{+\bullet} + e^- \text{ (ionization)}$$

$$H_2O \xrightarrow{\text{Ionizing radiation}} H_2O^{*} \text{ (electronic ionization)}$$

$$H_2O^{+\bullet} + H_2O \rightarrow H_3O^{+} + {}^{\bullet}OH$$

$$e^- + nH_2O \rightarrow e^-_{aq}$$

$$H_2O^{*} \rightarrow H^{\bullet} + {}^{\bullet}OH$$

$$e^-_{aq} + H^{+} \rightarrow H^{\bullet}$$

Figure 2.1: The mechanism of the formation of hydroxide radicals and solvated electrons, modified from Southworth-Davies and Garman[123].

The decay of diffraction intensity during macromolecular X-ray experiments was first investigated in 1962[124]. Room temperature measurements of the diffraction intensity of sperm whale myoglobin were recorded over 300 hours of continuous exposure, analysis of the intensity found that the decay was dependent on dose (dose is defined as the energy absorbed per unit mass of a sample where 1 Gy = 1 J kg^{-1}). To address the effects of radiation damage, cryocooling techniques were developed to coincide with the routine use of high intensity synchrotron sources[125]. A stream of cool nitrogen gas is used

to cool crystals to 100 K, at this temperature the diffusion of radicals is slowed down. However, radiation damage is still observed at cryo temperatures and is attributed to electrons tunnelling along the protein backbone. The study of radiation damage therefore aims to explain the processes occurring and specify the ideal data collection strategy from which undamaged structures can be obtained[91,98,126].

Attempts have been made to quantify the maximuum dose beyond which data quality is affected. The X-radiation dose limit in macromolecular crystallography is classically defined as the dose required for the total diffracted intensity to reach half of its initial value[127].

In 1990, studies of the dose causing half of the diffraction to be lost in two dimensional electron microscopy experiments at cryo-temperatures led to an estimated X-radiation dose limit of 20 MGy. Experimental measurements taken between 2005[128] and 2006[85,130] found that the relationship between dose and diffraction is linear and this relationship was used to calculate a new dose limit of 43 MGy. However, these limits only describe global damage and so are not useful metrics when designing data collection strategies. At far lower doses, specific damage may already be apparent within the protein structure. The formation of solvated photoelectrons occurs at doses below 1 kGy, followed by specific structural damage to amino acids at doses in the kGy – MGy range, finally the decay in diffraction intensity is observed between 1 – 100 MGy.

Specific damage affects particular amino acids in a well-defined order;

1. Disulphide bonds are broken.
2. Aspartate and Glutamate residues are decarboxylated.
3. Tyrosines are dehydroxylated.
4. The C-S bonds in methionine are broken.

Low-dose site specific damage also affects electron-affinic sites such as metals and cofactors. Metalloproteins are particularly susceptible to radiation damage due to the large X-ray absorption coefficient of metal atoms combined with the redox potential of the metal centre. The redox properties of metalloproteins are crucial to their function;

however, the reduction of metal centres is inevitable when exposed to X-ray radiation, due to the formation of solvated electrons. The half-life of oxidised species in metalloproteins is one order of magnitude less than the dose limit of the crystal[107,129–131].

This low dose damage is not immediately apparent in diffraction images or initial data processing statistics and may only be revealed during examination of the electron density map during downstream data processing. Calculation of electron density map is not usually completed until the experiment is over and the opportunity to collect data has passed. It is therefore important to understand radiation damage processes and time-scales in order to design data collection strategies that result in minimal damage contamination to the electron density map.

Although the X-ray crystal structure cannot be used to directly detect the REDOX state of metalloproteins or cofactors, this can be determined using complementary methods such as UV-vis, Raman and X-ray spectroscopies (XAFS, XAS)[103,106,108,109,132]. Such complementary methods are essential to determine the redox state of the cofactor during X-ray experiments so that reliable conclusions can be drawn about the oxidation state of the protein and the relationship between structure and function. Tracking the oxidation state using such methods during the X-ray data collection allows any changes in structure corresponding to different oxidation states to be observed.

Radiation damage, does not simply reduce diffracted intensity (and with it, spatial resolution of the data). Specific damage to amino acids and cofactors can cause significant structural and chemical changes within the crystal, that if not properly identified can have a serious impact on the conclusions drawn about biological function.

This chapter describes an investigation of the effect of the composition of crystallisation solution on the lifetime of oxidised haemproteins. Crystallisation solutions often contain species with large X-ray

absorption cross sections (such as halides and metal atoms), which increase the rate at which dose is accumulated in the crystal (the ‘dose rate’). This study has combined the use of UV-Vis spectroscopy with X-ray data collection to monitor the rate of reduction of the haem group as a function of dose rate.

2.2 Contributions to this chapter

Dr. Robin Owen and Professor Arwen Pearson provided the spectroscopic data recorded from thin films of horse myoglobin, bovine cytochrome *c* and crystals of horse cytochrome *c*. The sample preparation and data collection are described in sections 2.3.1 and 2.3.2. All data analysis was performed by myself and is described in section 2.3.3.

The work described in this chapter has been published in the following paper:

Owen, R.L., Yorke, B.A., Gowdy, J.A., Pearson, A.R., (2011) Revealing low dose radiation damage using single crystal spectroscopy, *J. Synch. Rad*., **18** 367-373

2.3 Materials and Methods

2.3.1 Sample preparation

2.3.1.1 Thin Films

Solutions of horse myoglobin (Sigma) at 20 mg ml^{-1} in 50% (v/v) 2-methyl-2,4-pentanediol (MPD) were doped with increasing amounts of NaBr (0-1.0 M in 0.1 M steps), and solutions of bovine cytochrome *c* (Sigma) at 20 mg ml^{-1} in 50% (v/v) MPD were doped with NaCl (0-1.0 M in 0.1 M steps). No additional buffer components were added. The solutions were prepared from stocks such that the concentration of protein was constant in all samples. Thin films of the solutions were cryo-cooled in 0.2-0.5 mm-diameter nylon (20 μm thick) loops at 100 K using a cryojet (Oxford Instruments). Visual inspection indicated the film thickness to be less than the thickness of the loops.

2.3.1.2 Crystals

Horse cytochrome *c* (Sigma) crystals were grown according to the method of Sanishvili *et al.*[133], using drops containing 40 mg ml^{-1} cytochrome *c*, 50 mM potassium phosphate pH 6.8 and 22% PEG 1000 (w/v) equilibrated against a reservoir of 30% (w/v) PEG 1000 and 50 mM potassium phosphate pH 6.8. Crystals ($\sim$100 × 100 × 300 μm) were soaked for 2 min in mother liquor containing increasing amounts of NaCl (0-0.6 *M*) or Na_2MoO_4 (0-0.6 M), harvested in nylon loops and directly cryo-cooled at 100 K in a cryojet without any additional cryoprotectant.

2.3.2 Spectroscopic data collection

The on-axis spectrophotometer at beamline X10SA at Swiss Light Source (SLS) was used for all X-ray experiments[102]. The X-ray beamsize was 50 x 50 μm with a flux of 1.1 x 10^{11} photons s^{-1} and energy of 12.4 keV and the focal spot of the spectrophotometer light source (Xenon lamp) was ~35 μm. On-axis UV-Vis spectra were recorded over 30 s (53.6 spectra per second) with an acquisition time of 10 ms per spectrum. The X-ray reduction was initiated by opening

the X-ray shutter a short time <4 s after the accumulation of the first spectrum. The spectra were recorded in triplicate for thin films of each halide doped myoglobin and cytochrome *c* solution. The experiment was repeated for the cytochrome *c* crystals doped with NaCl and Na_2MoO_4. The X-ray flux was reduced to 5 x 10^{10} photons s^{-1} before a second set of spectra were recorded for thin films of myoglobin doped with NaBr.

2.3.3 Data Analysis

To characterise the X-ray induced reduction of the haem, single-wavelength time courses were extracted from the data, following the shift in the Soret band (from 413 to 426 nm for myoglobin and 411 to 415 nm for cytochrome *c*), the appearance of the α-peak characteristic of reduced haem (557 nm myoglobin, 535 nm cytochrome *c*) and the formation of solvated electrons (600 nm). Myoglobin peaks were assigned based on spectra for myoglobin reduced by ^{60}Co γ-radiation at 77 K (where myoglobin cannot undergo the conformational rearrangements that normally accompany reduction[134]). Cytochrome *c* peaks were assigned based on literature values[135]

The time courses were extracted and converted to ASCII format using *Solis* (Andor Technology). Kinetic parameters were determined using *Gnuplot*, *Biokine* (Biologic) and *OriginPro* (Origin Lab) then further analysed using *OriginPro*. Absorbed-dose calculations for the protein samples were carried out using *RADDOSE*[136], assuming a constant sample volume and a non-rotating sample.

Rate constants for myoglobin and cytochrome *c* reduction by X-rays were determined for two features in the spectra: the shift in the Soret band and the increase in the α-band. Also fitted were the time courses for absorbance changes at 600 nm for both proteins in 50% (*v*/*v*) MPD as well as for 50% (*v*/*v*) MPD alone. All data were best fitted with a double exponential, as has previously been reported for met-myoglobin X-ray reduction as a function of incident X-ray energy[131]. This function is of the form:

$$y = A_1 \exp(-k_1 D) + A_2 \exp(-k_2 D) + y_0 \quad (2.1)$$

Where y is the absorbance of the Soret band or α-peak, k_1 and k_2 are the fast and slow rates, respectively, A_1 and A_2 are the amplitudes of the two exponents and D is the absorbed dose. The rate constants were therefore calculated in units of dose^{-1}. The function is constrained so that the fast process described by k_1 occurs first.

2.4 Results

2.4.1 Effect of cryoprotectant used on spectral changes

To ensure that the spectral changes observed, and the rates calculated from these observations were reliable, it was essential to quantify the contribution of all absorbing species to the spectra. The addition of cryoprotectants prevents the formation of crystalline ice and preserves the sample at 100 K, however, when exposed to X-rays some cryoprotectants absorb visible light, making them unsuitable for spectroscopic studies. The irradiation of glycerol by X-rays has been reported to produce a strong absorption peak centred at 600 nm[101], attributed to the formation of solvated electrons. This makes it unsuitable as a cryoprotectant for the studies of haem containing proteins, since the reduction of the haem group results in a splitting of α and β-peaks in the 500-600 nm range and this will be masked by the glycerol solvated electron peak.

McGeehan *et. al.*[137] reported that no absorbance peak is observed when MPD is exposed to X-ray radiation making it a more suitable choice for spectroscopic experiments. To test this the spectrum of a thin film of 50 % v/v MPD was recorded during a 25 s exposure to X-ray radiation (flux 1.1 x 10^{11} photons s^{-1}). A small but well resolved absorbance was observed at 600 nm when 50% (v/v) MPD was exposed to X-ray radiation. This effect is more than 10 times smaller in MPD than in glycerol and thus does not mask the temporal evolution of the haem protein and α and β-bands between 500 and 560 nm at the haem concentrations used here. MPD was therefore chosen as a suitable cryoprotectant for these studies.

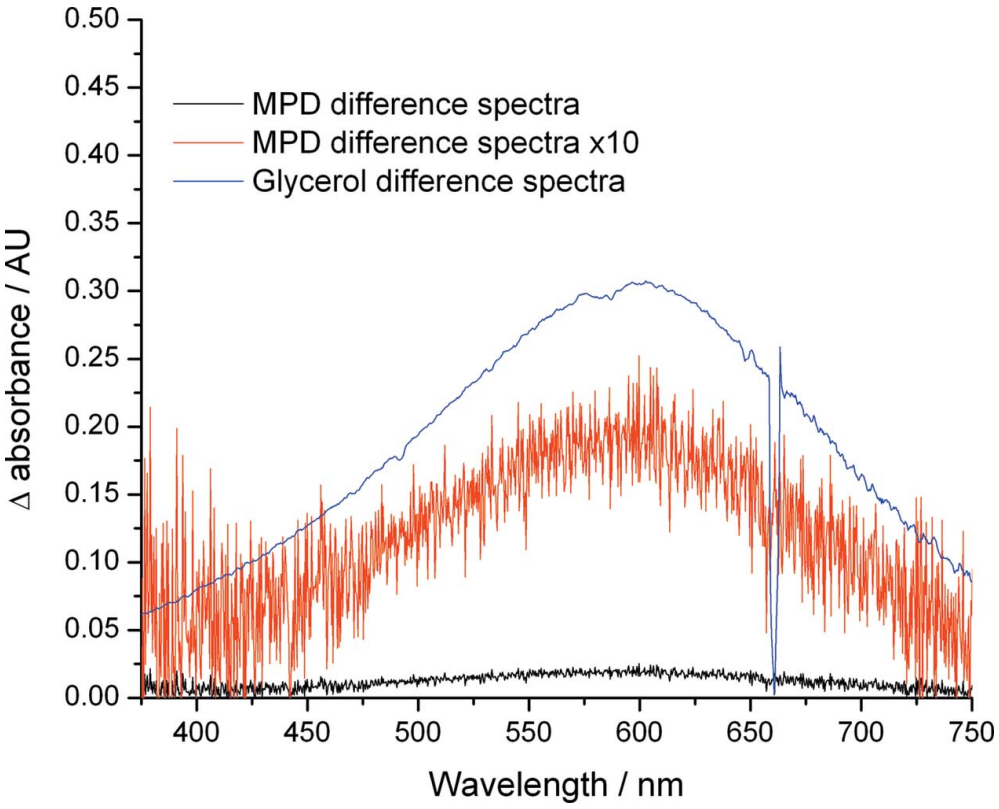

Figure 2.1: X-ray Difference spectra (shutter open - shutter closed) of MPD (50% v/v) and Glycerol (40% v/v)[101] recorded at 100 K during X-ray exposure. The sharp drop in intensity in the glycerol spectrum at ~660 nm is due to a deuterium lamp artefact. For ease of comparison of the spectral features around 600 nm, the MPD difference spectrum is multiplied by 10.

2.4.2 Dose rate dependence of radiation induced reduction of haem centres

Classical radiation damage processes such as the loss of diffracted intensity, unit cell changes, the breakage of disulphide bonds and decarboxylations are understood to be independent of the dose rate at cryo-temperatures[83]. To determine if there is any relationship between the dose rate and the reduction of haem centres by X-rays at 100 K, the rate of haem reduction was recorded during continuous X-ray exposure of thin films of both myoglobin and cytochrome *c*. The dose rate was modulated by doping solutions of both proteins with increasing concentrations of NaBr and NaCl. Adding heavy atoms in the protein solution causes the X-ray absorption cross section to increase and hence increases the absorbed dose rate. Increasing the concentration of NaBr in the protein solution from 0 to 1 M changes the absorbed dose rate from 19 to 28 kGy s^{-1}. Similarly for an increase of NaCl concentration from 0 to 1 M the dose rate will increase from 16 to 26 kGy s^{-1}. The effect was also tested in cytochrome *c* crystals, here increasing concentrations of NaCl, NaBr and Na_2MoO_4 were added to the crystallisation solution and soaked into the crystals. The doped thin films and crystals were monitored spectroscopically during X-ray irradiation.

Radiation induced spectral changes such as the red shift in the Soret band and the splitting of the broad $\alpha\beta$-band (~520-560 nm) into two distinct peaks were observed for both proteins indicating that the haem group was reduced in both cases (Figure 2.2). The time courses for the shift in the Soret band, formation of the α-peak and the formation of solvated electrons in MPD at 600 nm show biphasic behaviour, best described by a double exponential, indicating that two kinetically distinct processes occurred in all samples (Figure 2.3). This is contradictory to the existence of isosbestic points in the spectral time courses, which are indicative of a simple two state system.

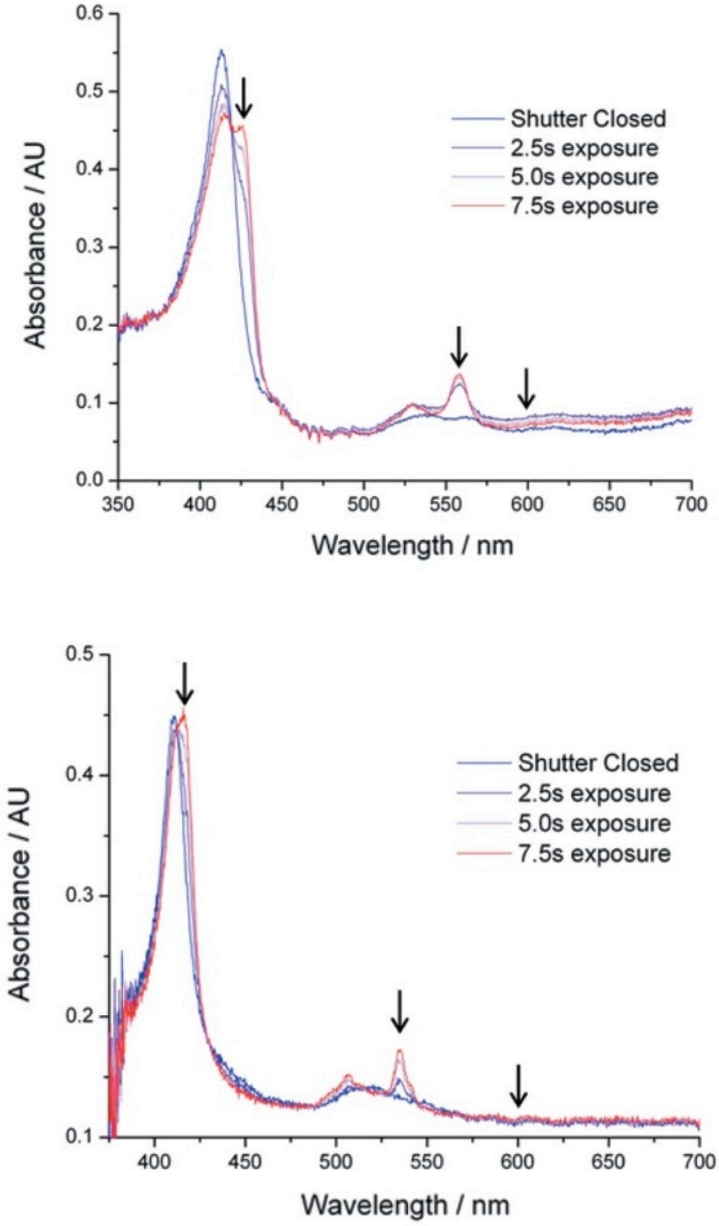

Figure 2.2: (Top) Myoglobin spectra before and after X-ray exposure. The blue line shows the oxidised myglobin spectrum before X-ray exposure and the reduced spectrum is shown in red. Two intermediate spectra recorded after 2.5 and 5 seconds of X-ray exposure are shown to highlight the isosbestic points. Arrows indicate the shift in the Soret band at 426 nm, the α-peak at 557 nm and the peak attributed to the formation of solvated electrons at 600 nm. (Bottom) Cytochrome *c* spectra before (blue) and after (red) X-ray exposure. Intermediate spectra are shown for 2.5 and 5 seconds of X-ray exposure. The arrows indicate the Soret band (415 nm), the α-peak (535 nm) and the peak attributed to solvated electrons (600 nm).

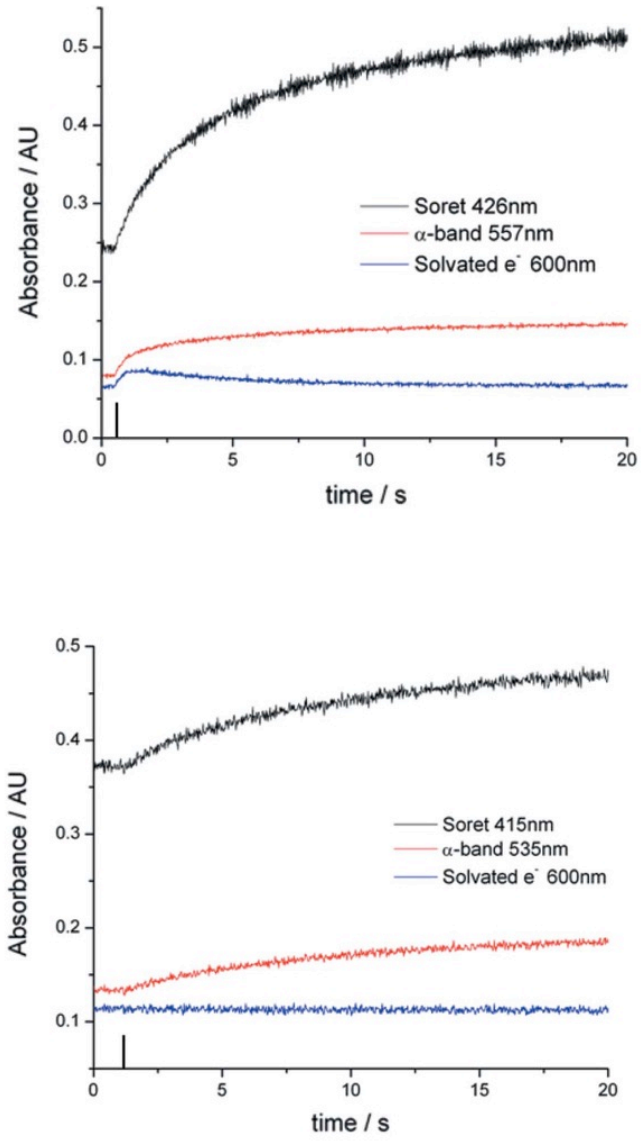

Figure 2.3: (Top) Extracted time courses from the myoglobin thin-film spectra at three wavelengths; the Soret band (426 nm), the α-band (557 nm) and the solvated electron peak (600 nm). (Bottom) Extracted time courses from the cytochrome *c* thin-film spectra at three wavelengths; the Soret band (415 nm), the α-band (535 nm) and the solvated electron peak (600 nm). In both cases the vertical line indicates the time at which the X-ray shutter was opened.

The rate constants, k_1 and k_2 for all three spectral features in myoglobin and cytochrome *c* thin films are shown in figures 2.4 and 2.5, where each point is the mean of three observations. The cytochrome *c* crystal data were saturated at the Soret band and the 600 nm feature was very noisy and thus only the α-peak time course was analysed (Figure 2.6).

The observed rate constants k_1 and k_2 (Gy^{-1}) are each similar at all three wavelengths studied and are essentially constant with absorbed dose, indicating that, like classical radiation damage, the X-ray-induced rapid reduction of the haem centres and the rate of solvated electron generation is independent of dose rate. The degree of haem reduction is dependent therefore only on the total absorbed dose.

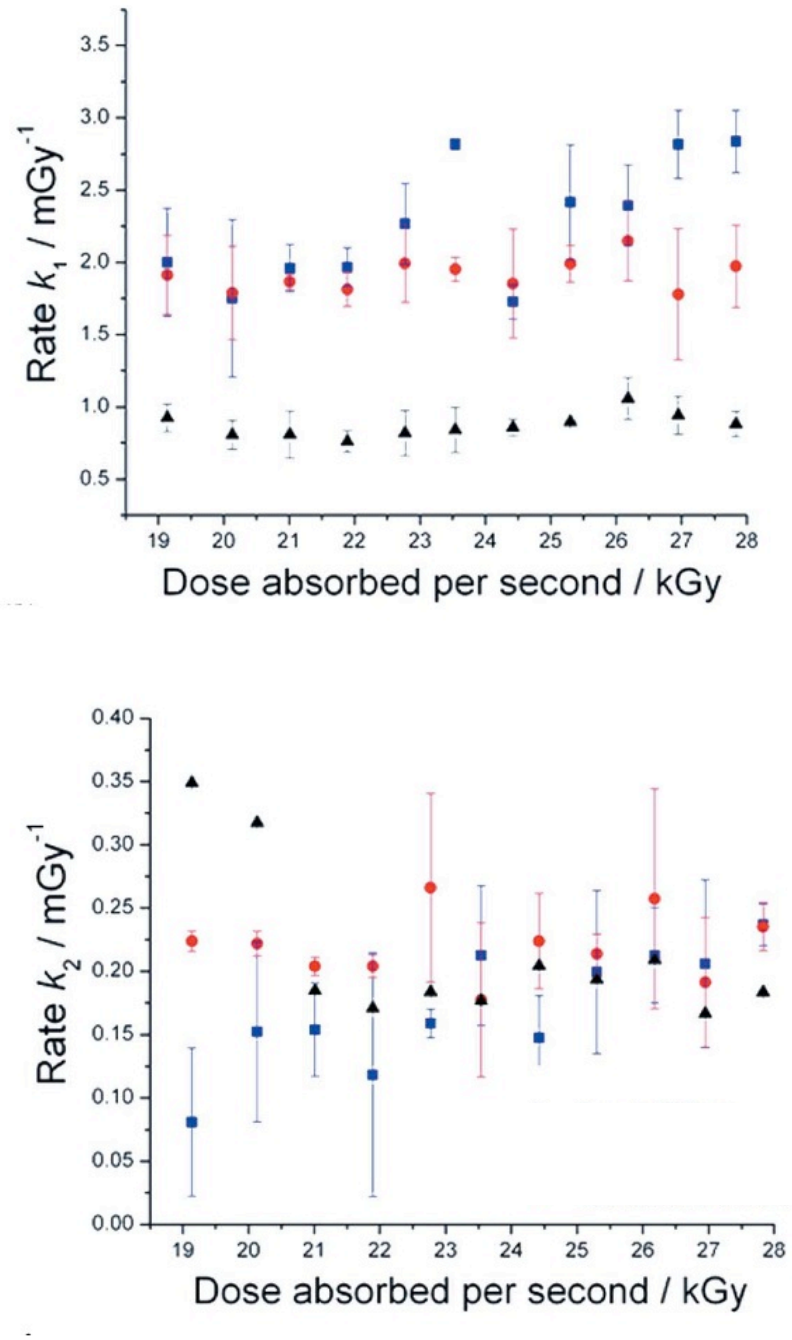

Figure 2.4: Rate constants for myoglobin thin-films doped with increasing concentrations of NaBr (0-1.0 M in 0.1 M steps from left to right). Each point is the mean value of three observations. Rate constants for the Soret peak (426 nm) are shown with black triangle, for the α-band (557 nm) with red circles and for the solvated electrons (600 nm) with a blue square.

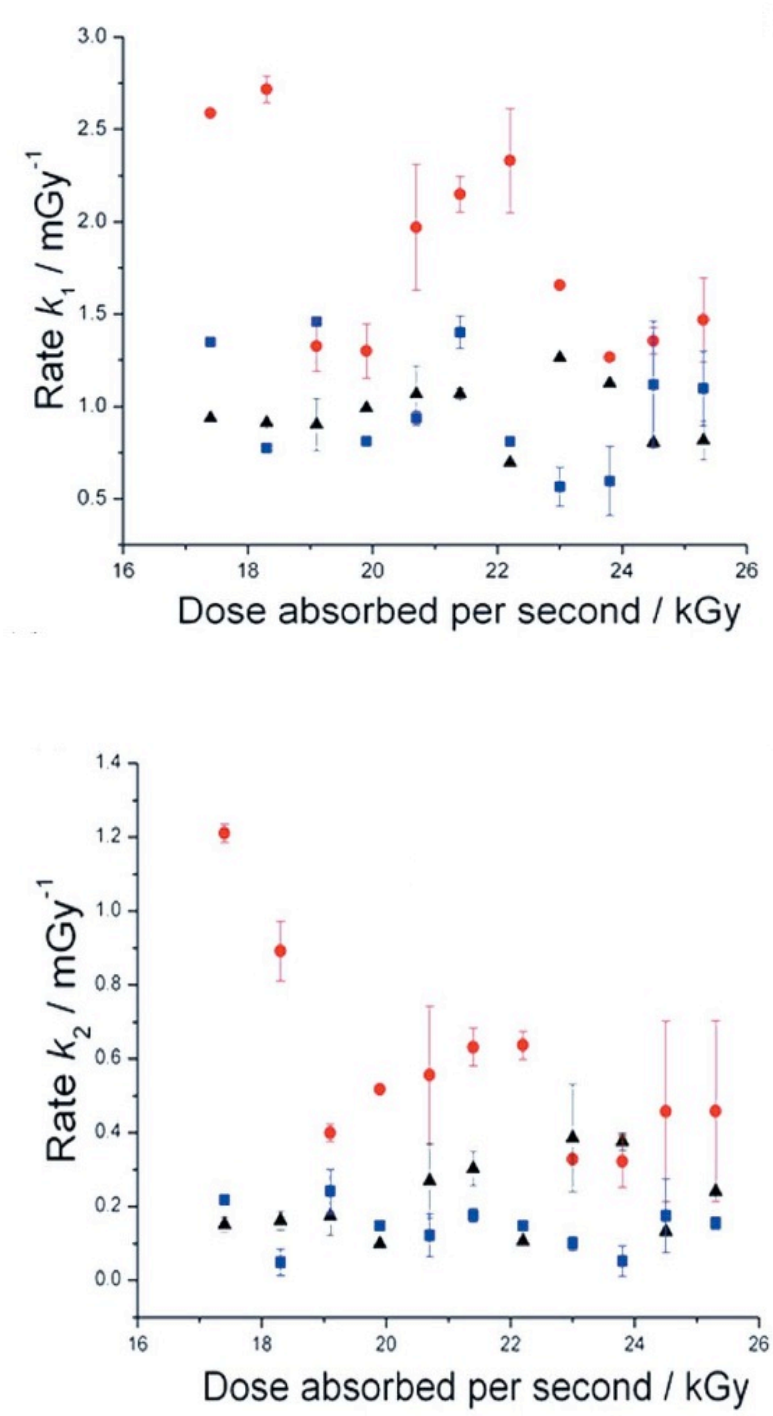

Figure 2.5: Rate constants for cytochrome *c* thin-films doped with increasing concentrations of NaCl (0-1.0 M in 0.1 M steps from left to right). Each point is the mean value of three observations. Rate constants for the Soret peak (416 nm) are shown with black triangle, for the α-band (535 nm) with red circles and for the solvated electrons (600 nm) with a blue square.

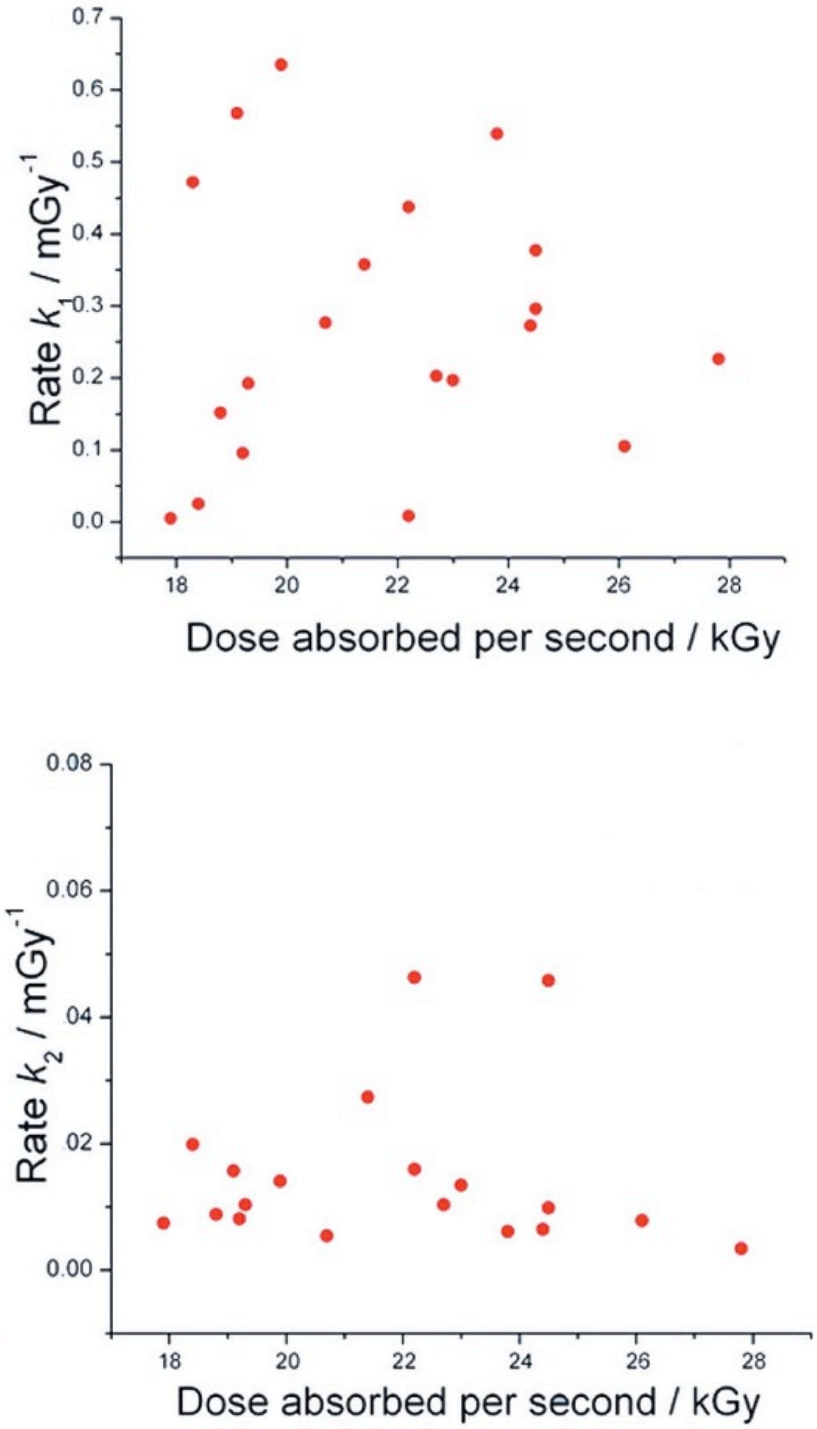

Figure 2.6: Rate costants for horse heart cytochrome *c* crystals doped with NaBr, NaCl and Na_2MoO_4. Each point is the mean value of three observations. Cytochrome *c* crystal k_2 data have been scaled to exclude a single outlier at 0.23 mGy^{-1}. Owing to saturation effects and the difficulty in tracking the weak solvated electron signal in crystals, only the α-band has been tracked for the cytochrome *c* crystal data (shown as red circles).

The dose at which the solvated electron population reaches a maximum ("turn over dose") was calculated by differentiation of equation 2.1 using the exponential fit parameters (A_1, k_1, A_2 and k_2) of the myoglobin thin film time courses at 600 nm for two incident fluxes over the range of NaBr concentrations (Figure 2.7). The turn over dose was slightly higher for the data collected at a higher flux; however, it showed no dependence on the halide concentration. The mean turn over dose was 45 kGy.

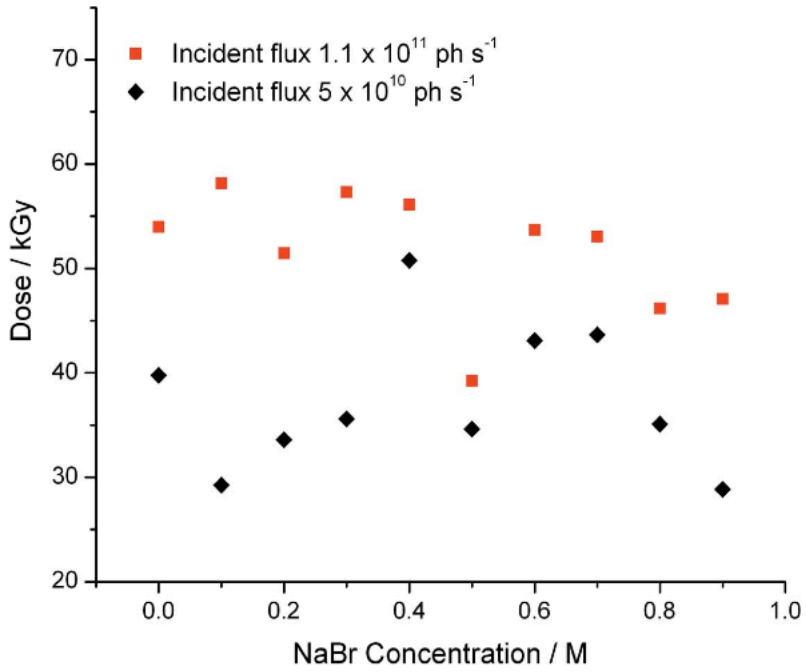

Figure 2.7: The absorbed dose at which the solvated electron population reaches a maximum in thin films of myoglobin (as determined from the change in absorption at 600 nm) as a function of both sodium bromide concentration and incident flux rate. Each point is the average of three measurements.

2.5 Discussion

Extensive studies of radiation damage by several groups have demonstrated that classical radiation damage (loss of diffracted intensities, changes in unit-cell dimensions, disulfide bond breakages, decarboxylations, *etc.*) is purely a function of the cumulative absorbed dose[83,88]. The cumulative absorbed dose is dependent on the X-ray absorption cross section of the illuminated volume (which can include the crystal itself as well as surrounding mother liquor and the mount). A comprehensive study by Kmetko *et al.*[138] showed clearly that the composition of the mother liquor, and hence the absorption cross section of the sample, does affect the rate of accumulation of classical radiation damage, and suggested that attempts to reduce the X-ray absorption cross section of the mother liquor should extend crystal life-time at 100 K because the dose is reduced.

Here we have investigated whether the rapid X-ray reduction of the haem centre in myoglobin and cytochrome *c* at low cumulative X-ray doses is also independent of dose rate. Our data show clearly that the rate of accumulation of this low-dose damage is independent of dose rate at 100 K.

A relatively small increase and subsequent decrease in absorbance was observed at 600 nm upon irradiation of myoglobin, cytochrome *c* and also of MPD alone. By comparison with the better characterised absorption maximum of glycerol upon X-ray irradiation [141,101] this was attributed to solvated electrons. Interestingly this peak grows and decays with rate constants that are strikingly similar to the two rate constants required to fit the X-ray-driven reduction of the haem proteins reported here. Beitlich *et al.*[131], who studied changes at 557 nm (nominally the α-band of myoglobin, but where the contribution of the absorbance of solvated electrons can also be significant) upon X-irradiation of myoglobin, suggested that k_1 (the faster rate) is representative of the formation of solvated electrons upon X-ray illumination. They assigned the slower k_2 as representative of the

haem reduction rate when the concentration of solvated electrons had reached a steady state. The similarity of the k_2 for both myoglobin and cytochrome *c* reduction to that observed here for the decay of the 600 nm feature, which presumably reflects the decay to a steady-state level of solvated electrons, supports this hypothesis.

In view of this, we determined the dose at which the population of solvated electrons reaches a maximum (*i.e.* the maximal absorbance at 600 nm), before decaying to its steady state was determined and found to occur at ~45 kGy. This value is a function only of the absorbed dose and not the mother liquor composition (other than in the way this composition affects the absorption cross sections) or incident flux. This dose is somewhat smaller than the dose limits previously reported for site specific damage at 100 K by synchrotron X-ray irradiation (Table 3.1). However, it is comparable with dose limits observed spectroscopically during γ-radiolysis of myoglobin at relatively low dose rates (yield of 50% reduced myoglobin generated at an absorbed dose of 20 kGy with an incident dose rate of 220 Gy min^{-1} [140].

Site	Method used	Dose Limit	Citation
Disordering of selenomethionine side chains	XANES	2 MGy	Holton[107]
Reduction of copper nitrate reductase	UV-Vis, XAS	1.5 MGy	Hough et al.[129]
Cleavage of anomalous scatterers	XAS	0.5 MGy	Oliéric et al.[130]
Photoreduction of putida redoxin	XAS	0.3 MGy	Corbett et al.[106]
Reduction of met-myoglobin	UV-Vis	0.21 MGy	Beitlich et al.[131]

Table 2.1: Dose limits reported for site specific damage

Taken together, these observations suggest that reducing the absorption cross section of the crystallization mother liquor, either by

transferring the crystal into a weakly absorbing mother liquor/cryoprotectant solution or by backsoaking to remove non-bound anomalous scatterers, will somewhat extend the lifetime of oxidised redox centres in the X-ray beam. However, this gain is likely to be small, as the rate of the haem centre reduction appears to be strongly coupled to the generation of solvated electrons that, in myoglobin in MPD, reaches a maximum at an absorbed dose of only 45 kGy. With the beamline fluxes available at third-generation synchrotron sources, such a dose can easily be reached within the time required to collect a single diffraction image.

Therefore, a composite data collection strategy in which small wedges of data are collected from several crystals (or several points on a large single crystal) remains the best, and possibly the only, approach to obtaining the structures of fully oxidized and partially oxidized species.

To successfully collect a composite dataset it is imperative to characterise the susceptibility of the system to site-specific radiation damage, in order to determine how much useful data can be collected from each crystal. Where complementary methods are available on the beamline this can be monitored directly during data collection. However, where this is not possible, preliminary experiments must be performed where crystals are sacrificed to determine when damage occurs.

The use of complementary methods during the diffraction experiment is therefore extremely useful in establishing the structural state of the recorded diffraction data, and is essential for the recognition and tracking of low-dose radiation damage. The installation of complementary experiments on the beamline can enable data quality to be monitored during X-ray experiments and therefore reduce the sample consumption and preparation time for such experiments.

Chapter 3 XEOL – A new tool for studying radiation damage during diffraction data collection

3.1 Introduction

Complementary spectroscopic techniques have had a major impact in the macromolecular crystallography radiation damage field, allowing the monitoring of radiation induced changes. However, many of these methods require a reporter chromophore (*i.e*. UV-Vis, fluorescence) and, even when a chromophore is not required (*i.e*. IR, Raman), the spectroscopic instrumentation required to monitor the sample during X-ray exposure is often bulky and limits the diffraction experiment by blocking certain sample/detector geometries[141].

Here, a relatively unexplored phenomenon in macromolecular crystallography: the glowing, or luminescence, of macromolecular crystals upon X-ray irradiation is investigated. Luminescence during irradiation is a phenomenon that is common to all molecules and that occurs during all X-ray data collections. Crystals emit visible light during, and for a short time subsequent to, X-ray exposure. This phenomenon, known as X-ray excited optical luminescence (XEOL), is due to the excitation of core electrons by X-rays, via the photoelectric effect, to the lowest unoccupied molecular orbital (LUMO) and LUMO +1. This excitation is followed by the radiative recombination of the excited electrons in the LUMO and holes in the highest occupied molecular orbital (HOMO). In protein crystals the relaxation of electrons from the lowest lying singlet and triplet energy levels of the π-system of aromatic amino acids gives rise to emission of photons in the visible range of the electromagnetic spectrum[142–144]. Importantly, in principle XEOL can be recorded from any crystal, with no requirement for a reporter chromophore, and also requires only a collection optic connected to a spectrograph and detector, reducing the need for additional bulky equipment around the sample position during the diffraction experiment.

XEOL intensity is proportional to the intensity of the incident X-rays and the form of the spectra is a function of both the atomic number of the constituent elements within the sample and the local chemical

structure[145]. XEOL is commonly used in the physical and material sciences to provide information on elemental composition, coordination geometry and electronic properties and is the basis of scintillator methods of X-ray detection[145]. Applications include the detection of local structural defects in crystalline silicon and the identification of trace impurities in solid state chemistry (crystals of small molecules)[145,146]. A particularly interesting application is the study of the mechanisms of radiolysis, whereby the lifetime of luminescence is proportional to the concentration of free radicals present[147,148].

Light atoms ($Z \leq 16$) emit a very weak XEOL signal and therefore it is rarely observed in macromolecular samples. Early work estimated luminescence yields from dried powders of both amino acids and proteins, and also investigated the effect of solvent quenching on spectra[143,144,149]. More recently, tuneable soft X-rays have been used to probe the optical properties of proteins conjugated to an extrinsic fluorophore[35].

Since XEOL is the result of the absorption of energy from X-ray radiation it is clearly related to radiation damage Indeed, the use of XEOL as a tool for studying radiation damage in biomolecules was first suggested in 1965[144]. Recently, McGeehan and coworkers reported the measurement of XEOL from a trypsin crystal using the online single-crystal spectrometer at ID14-2, ESRF (McGeehan *et al.*, 2009). Interestingly, this signal bleached with increasing X-ray dose. This raised the intriguing possibility that XEOL studies of macromolecular crystals may shed light on the specific changes that occur during X-ray illumination. Although the initial physical processes (direct and secondary ionizations, generation of solvated electrons and radical species) and the resultant effects of radiation damage (redox-centre reduction, disulfide-bond cleavage, decarboxylation *etc.*) are well known,[83] the chemistry of radiation damage in a macromolecular sample remains poorly defined. Radiation damage is the major limitation on the resolution and quality of diffraction data that can be obtained from a macromolecular crystal. Therefore, understanding

how, why, when and where damage processes occur is key to the design of data-collection and processing protocols that enable us to determine undamaged and biologically relevant structures.

3.1.1 The physical origin of XEOL

When macromolecular crystals are exposed to X-ray radiation only 2% of the X-ray photons interact with the sample, of this 1.7 % interact via the photoelectric effect[83]. When an X-ray interacts with an electron in an inner orbital of an atom, the absorbed energy can either eject an electron to produce a solvated photoelectron. Or it can promote an electron to the LUMO (lowest unoccupied molecular orbital) or LUMO +1 (Yates *et al*. 2001). When the electron is excited to a higher energy level a hole is formed in the core orbital. The excited state has a lifetime of a few femtoseconds before it relaxes via one of two mechanisms. The first is known as the Auger process, in which an electronic relaxes from a higher energy level to the inner shell. This results in electron hole recombination and the ejection of an Auger electron through coupling of the transition energy to an outer shell electron[150]. The second mechanism is X-ray fluorescence, here the transition energy is not coupled to an electron but is released as a photon. Both of these processes may lead to XEOL and are illustrated in figure 3.1.

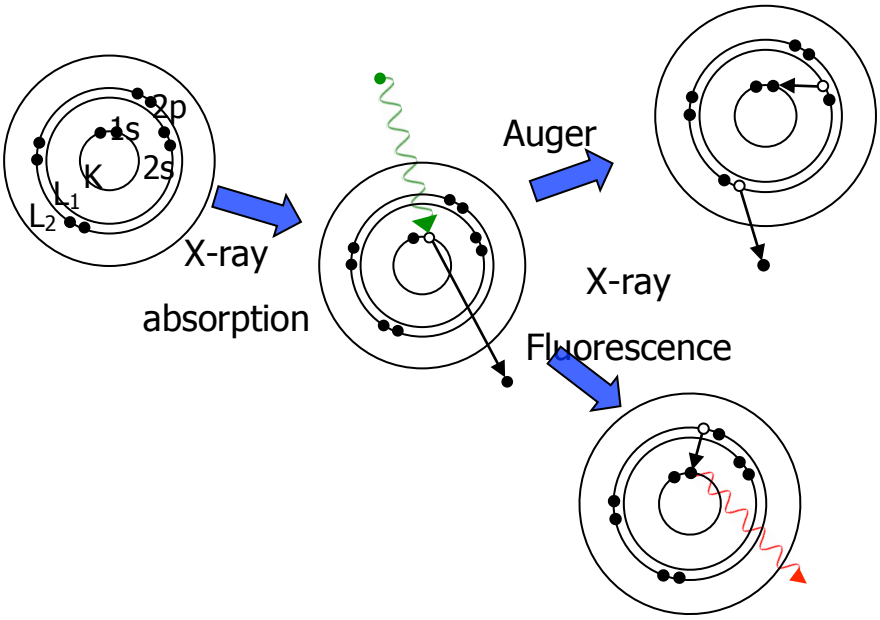

Figure 3.1: Illustration showing the possible relaxation mechanisms after the absorption of an X-ray photon.

The relaxation event iterates many times with the emitted photon continually decreasing in energy until the recombination occurs between an electron in the LUMO and a hole in the HOMO (highest occupied electronic orbital), this results in the emission of a photon in the visible region of the electromagnetic spectrum which can be measured to produce a XEOL spectrum. The intensity of XEOL is proportional to incident X-ray intensity and the spectra are a function of elemental composition and the local chemical structure of the sample.

3.2 Contributions to this chapter

Dr. Robin Owen and Professor Arwen Pearson constructed the spectrophotometers that were used in these experiments and collected initial spectral data on the test proteins and cryoprotectants. During subsequent beamtimes I then collected the rest of the data presented in this chapter. I performed the spectroscopic data processing and analysis described in this chapter and Dr Owen analysed the diffraction data.

The work described in this chapter has been published in the following paper:

Owen, R.L., Yorke, B.A. & Pearson, A.R. (2012) X-ray excited optical luminescence of protein crystals: a new tool for studying radiation damage during diffraction data collection. *Acta Cryst.* **D68** 505-510

3.3 Materials and Methods

3.3.1 Measurement of XEOL spectra

XEOL spectra were collected at both the Swiss light source (SLS, beamline X10SA) and Diamond light source (DLS, beamline I24).

At SLS the spectra were collected using the on-axis microspectrophotometer[102] in a 180^{o} scattering geometry. The spectral resolution was <1 nm using a grating with 150 lines per mm blazed at 300 nm. All ambient lighting was excluded from the experimental hutch to prevent interference with the collection of the weak luminescence. The focal spot at the sample was ~60 mm. XEOL were collected between 300 and 900 nm (Shamrock 303i spectrograph, Newton CCD, Andor Technology) with an accumulation time of 0.5 s. The X-ray energy was 12.4 keV and the beamsize was 50 x 50 mm (1 x 10^{12} photons s^{-1}). There was no synchronisation of the X-ray and spectrometer shutters so the accumulation times of the spectrographs were set to half the X-ray exposure time to ensure the X-ray shutter was open for at least one spectral accumulation.

At DLS the spectra were collected off-axis. The X-ray energy was 12.68 keV and the beam size was defocused to 30 x 30 mm (1 x 10^{12} photons s^{-1}) at the sample. The optical focal spot at the sample was ~60 mm in diameter. Luminescence spectra were collected between 200 and 750 nm (Shamrock 303i spectrograph, Newton CCD, Andor Technology).

3.3.2 Sample preparation

3.3.2.1 Amino acid crystals

Crystalline powders of chromatographically homogenous amino acids (DL-alanine, L-arginine, L-cysteine, L-cystine, L-glutamate, L-histidine, L-leucine, DL-methionine, DL-phenylalanine, L-proline, DL-tryptophan and L-tyrosine) were purchased from BDL (Amino Acid Reference Collection for Paper and Thin Layer Chromatography). Amino-acid crystals larger than or equal to the beam size were mounted in a nylon loop,

suspended in a thin film of dimethylsulfoxide (DMSO) and flash-cooled to 100 K in a nitrogen cryostream. XEOL spectra were accumulated over 10 s. For each amino acid tested an initial spectrum was recorded with the X-ray shutter closed, followed by a series of spectra with the X-ray shutter open.

3.3.2.2 Protein crystals & diffraction data collection

Hen egg-white lysozyme (HEWL), thermolysin and equine spleen apoferritin and holoferritin were obtained from Sigma and were crystallized using standard techniques without further purification. Crystallization conditions and fractional aromatic amino-acid compositions of all samples used are summarized in Table 3.1.

Crystal	Crystallization conditions	Amino acid composition (%,No.)				
		His	Phe	Trp	Tyr	No. of disulphides
Ferritin	0.6 *M* $(NH_4)_2SO_4$, 10 m*M* $CdSO_4$	3.4% (6)	1.1% (2)	0.57% (1)	3.4% (6)	0
HEWL	7%(*w*/*v*) NaCl, 0.1 *M* sodium acetate pH 4.7, 20% ethylene glycol	0.78% (1)	1.6% (2)	4.7% (6)	2.3% (3)	4
NAL	100 m*M* Tris-HCl pH 8.2, 200 m*M* ammonium acetate, 18% PEG 3350	3.6% (11)	3.6% (11)	0.33% (1)	4.3% (13)	0
Thermolysin	50 m*M* MES, 1 *M* NaCl, 45%(*v*/*v*) DMSO	2.5% (8)	2.5% (8)	0.94% (3)	8.9% (28)	0

Table 3.1: Crystallization conditions and fractional aromatic amino-acid compositions of the crystals used.

Crystals of *Escherichia coli N*-acetyl-D-neuraminic acid lyase (NAL[151]) were kindly supplied by Ivan Campeotto (University of Leeds). The crystals of apoferritin and holoferritin were grown in identical crystallization conditions and were cryoprotected in mother liquor

containing 40% glycerol; the crystallization conditions of other crystals were such that no additional cryoprotectant was required. All data were collected with protein crystals held at 100 K. SLS diffraction data were recorded using a MAR 225 detector. For each sample, the same 1° oscillation image was collected repeatedly in order to monitor changes in the integrated intensity of the same reflections with increasing X-ray dose.

3.3.2.3 Cryoprotectants

XEOL data were also collected from thin films of cryoprotectants (glycerol, 2-methyl-2,4-pentanediol, DMSO and paraffin oil) which were mounted in nylon loops and cooled to 100 K in a nitrogen cryostream. The XEOL spectra for each cryoprotectant were accumulated over 5 s, before exposure to X-rays and at a series of time points during exposure. These results were used to characterise the contribution of the cryoprotectant to the XEOL spectra of the amino acid or protein crystals.

3.3.3 Data processing

3.3.3.1 X-ray diffraction data

Diffraction data were analysed using LABELIT[152,153]. The diffracting power of each crystal was defined as the integrated signal strength in pixel-ADC units (where ADC stands for analogue to digital conversion, this unit is used where photons are counted directly and the recorded value is converted into an electric signal, which is digitised using an analogue to digital convertor. The resulting 'count' therefore represents an exact number of photons per pixel). This was calculated above the local background for all Bragg candidates for each image. This value was determined using DISTL[152] and was normalised to the first image in each dataset to enable comparison of the decay in diffracting power and XEOL of different crystals. The dose absorbed by each sample was calculated using RADDOSE[136]. The iron content of holoferritin was assumed to be 1760 Fe atoms per 24-mer[154]. The crystals used in all experiments were larger than the X-ray beam size and the rotation

of the crystal was only 1^{o}, so the beam size was used to calculate the absorbed dose.

3.3.3.2 XEOL data processing

The signal-to-noise ratio of XEOL spectra recorded from short (<1 s) X-ray exposures was extremely low. The raw spectrum of apoferritin is shown in figure 3.2; the spectral features are not easily identifiable.

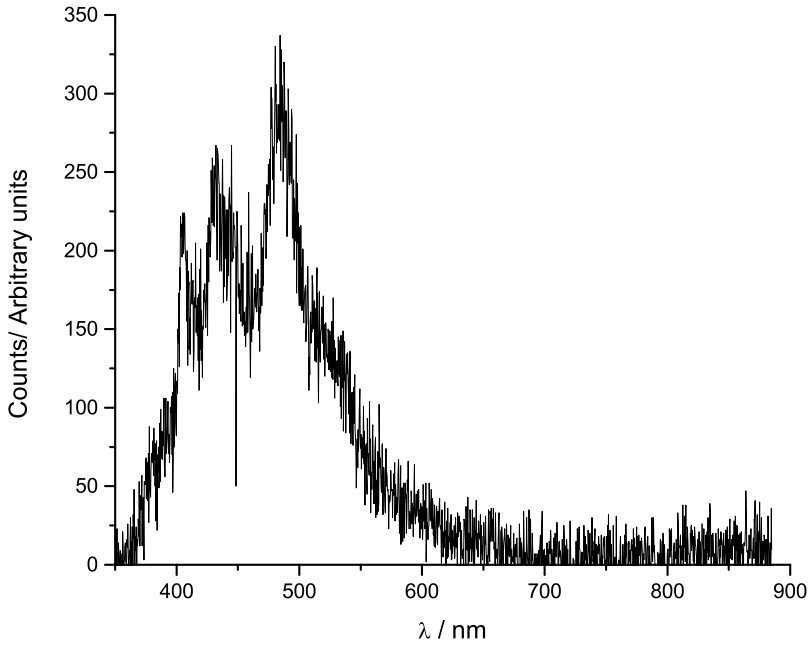

Figure 3.2: Raw XEOL spectrum of apoferritin, the poor signal-to-noise ratio is due to the short accumulation time of the spectrum (0.5 s) chosen to correspond to general X-ray exposure times used at synchrotron sources.

One possible way to increase the signal-to-noise ratio would be to increase the time of the X-ray exposures and spectral accumulation times but this is not a satisfactory solution. This is because the decay in XEOL signal is non-uniform over longer time(dose)-scales and longer exposure times (> 1 s) are not typical of macromolecular crystallography X-ray diffraction data-acquisition times at 3^{rd} generation synchrotrons.

Instead post-processing of the spectra was performed to improve data quality. Four smoothing methods were tested on the noisy XEOL spectra using OriginPro8.

Adjacent averaging: The average of a predefined number of data points around a particular point is calculated and the original data point is replaced by the average value.

Moving point averages: This is similar to adjacent averaging, however the window of averages is moved by one point along the data set each time and the mid point is calculated using the following equation:

$$s_i = \frac{1}{2n+1} \sum_{j=i-n}^{i+n} y_j$$

(4.1)

Where *2n+1* is the size of the window, *i* is the data point running from *i = n* to *n-1* points from the end of the data set.

Both of these smoothing techniques are best used when trying to eliminate low frequency high intensity spikes in a data set. These can be caused glitches in mains power or instrumentation being turned on elsewhere in the lab.

Savitzky-Golay: This is a method of filtering data in which a window size is defined in which a polynomial regression is performed (successive calculations are carried out to determine the best approximation of a curve fitting the data). The polynomial curve is then used to determine a value to replace the original data point.

Fast Fourier transform filtering: The data is transformed using a discrete function shown in equation 4.2.

$$g(v) = \frac{1}{\sqrt{N}} \sum_{t=0}^{N-1} f(t) \exp^{-i2\pi(v/N)t} \qquad (4.2)$$

Where *g(v)* is the discrete transform of signal *f(t)* which is sampled at points *t*, *N* is the number of data points and *v* and *t* are integers. After

the signal is transformed it can then be filtered to remove high frequency noise above a predefined threshold. The data is then reverse transformed and the filtered signal is recovered[155].

These two smoothing techniques are best used when there is high frequency noise present, as in the XEOL spectra.

The techniques were judged based on the knowledge of how each calculated a smoothed plot, the resulting smoothness after an acceptable level of refinement and what changes were observed from the raw spectrum (Figure 3.3).

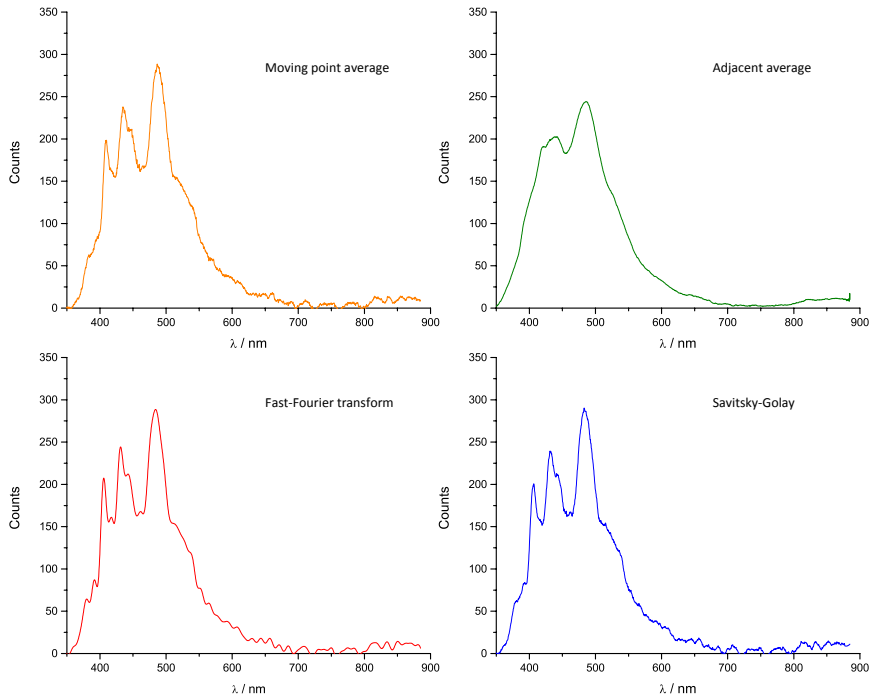

Figure 3.3: The four smoothing methods tested, demonstrated on the Apoferritin XEOL spectrum. Moving point averaging (orange) resulted in a red shift of the spectral features and adjacent averaging (green) resulted in the smoothing out of peaks. The fast-Fourier transform (FFT, red) and Savitsky-Golay (blue) signal processing methods preserved the spectral features to produce satisfactory spectra.

The low pass FFT filter was selected as optimal. This method filters out high frequency noise rather than using a weighted polynomial fitting technique, as with the Savitzky Golay method. Optimization of the FFT mask was performed by finding the lowest possible filter frequency that did not result in significant loss of detail in the spectrum.

A low pass filter frequency of 0.09 was used to remove all high frequency noise and leave a spectrum with a satisfactory amount of detail, shown in figure 3.4.

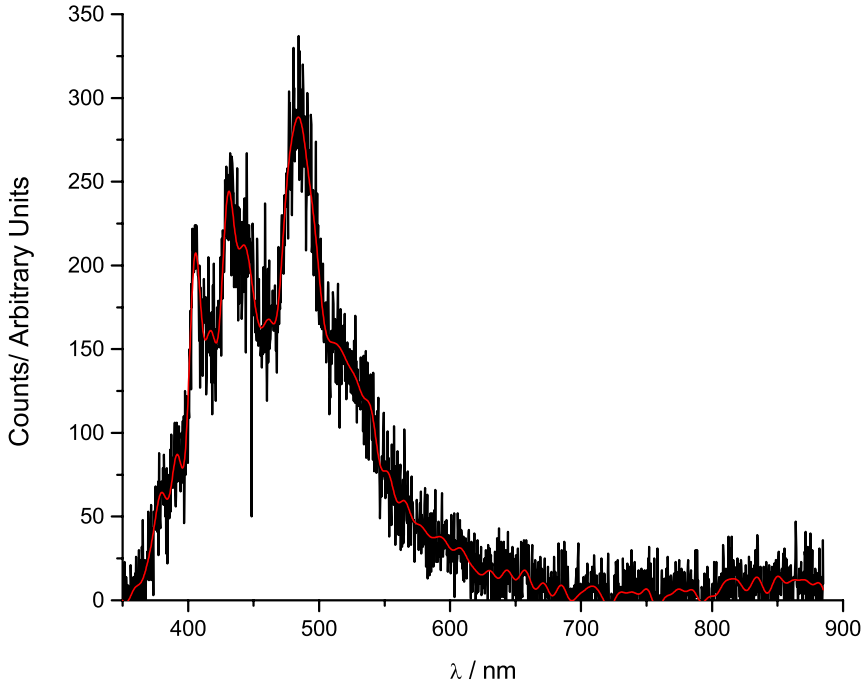

Figure 3.4: Apoferritin XEOL spectrum with the raw data shown in black and the FFT filtered data shown in red.

After smoothing the positions of λ_{max} were identified and the total yield of luminescence was calculated by integration of the smoothed XEOL spectra between 300 and 805 nm. The rate of decay in the XEOL signal was analysed by plotting the integrated XEOL intensity against the absorbed X-ray dose. The XEOL decay rates were then calculated by fitting an exponential decay to the data.

3.4 Results

4.4.1 XEOL Spectra

4.4.1.1 Amino Acids

XEOL spectra from crystalline powders of single amino acids suspended in DMSO are shown in Figure 3.5. Those containing aromatic groups emitted luminescence with λ_{max} between 380 and 537 nm. A weak XEOL signal was observed for cystine with λ_{max} at 808 nm, which is likely to arise due to the disulphide bonds formed between the cystine thiol groups. The XEOL spectra bleached after continued exposure to X-rays, as previously observed in other inorganic systems[145]. The spectra were not observed to change as a function of crystal orientation. No XEOL signal was observed for any other amino acid between 300 and 900 nm. These results suggest that the XEOL of amino acids can be attributed to delocalised π-electrons in the aromatic amino acids and the electrons involved in the formation of disulphide bonds.

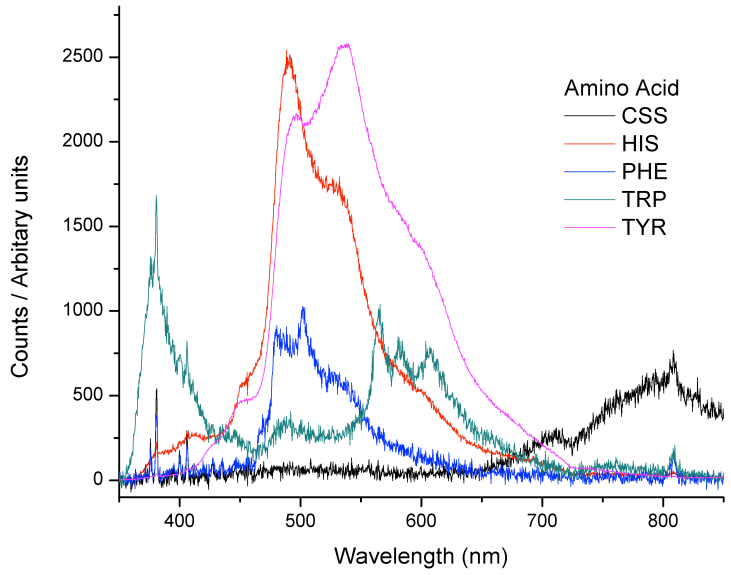

Figure 3.5: XEOL spectra of individual aromatic amino acids and cystine. The histidine and tyrosine spectra were scaled down by a factor of 2 and 10 respectively to allow direct comparison between all samples.

The Tyrosine, Tryptophan and Phenylalanine spectra were compared to those previously reported from powders or tryptophan dissolved in a mixture of 1:1 water:ethylene glycol[142–144,156,157], Table 3.2. The spectral shapes were found to be consistent, however, the λ_{max} values were not identical, this difference was attributed to changes in solvent polarity, sample state (powder, solution, crystalline), the flux density of incident X-rays and the sample temperature.

Sample	Crystalline λ_{max} / nm (this study)	Literature λ_{max} / nm
Tyrosine	537	458 (powder)[142]
Tryptophan	379	315 ± 3 (powder)[142] 335 ± 3 (aqueous glass)[156] 360 (powder)[157]
Phenylalanine	502	527 (powder)[142]
Histidine	491	-
Cysteine	808	-

Table 3.2: Comparison of λ_{max} values for data collected from crystalline samples and literature values from powder or solution.

3.4.1.2 Cryoprotectants

Glycerol, MPD and DMSO were found to produce no luminescence signal after irradiation by X-rays, consistent with the lack of any delocalised electrons in their structures. Paraffin oil, however, was found to emit a broad spectrum over the same range of wavelengths as protein luminescence and so is unsuitable as a cryoprotectant for protein XEOL experiments.

3.4.1.3 Protein crystals

XEOL spectra were recorded for HEWL, thermolysin, NAL, apoferritin and holoferritin, and are shown in Figure 3.6 and Figure 3.7. The spectra are complex, but distinct spectral features were observed for each protein. These were not found to be dependent on crystal orientation. The XEOL studies of pure amino acids indicates that the luminescence from each protein was due to the presence of aromatic

amino acids and disulphide bonds. However, comparison of the spectra to those in Figure 3.6, shows that protein XEOL is not the simple sum of luminescence from individual amino acids. The λ_{max} values are also generally red shifted compared to those of the individual amino acids in DMSO. This is likely to be because XEOL, like fluorescence, is quenched or altered by non-radiative decay and local polarity of the individual amino acids. This is evident in Figure 3.7 where a change in both spectral shape and red shift is observed between the XEOL of apo- and holoferritin. This can be attributed to the presence of the amorphous iron core in holoferritin that alters the radiative and non-radiative transfer processes and causes an increase in the protein dielectric constant.

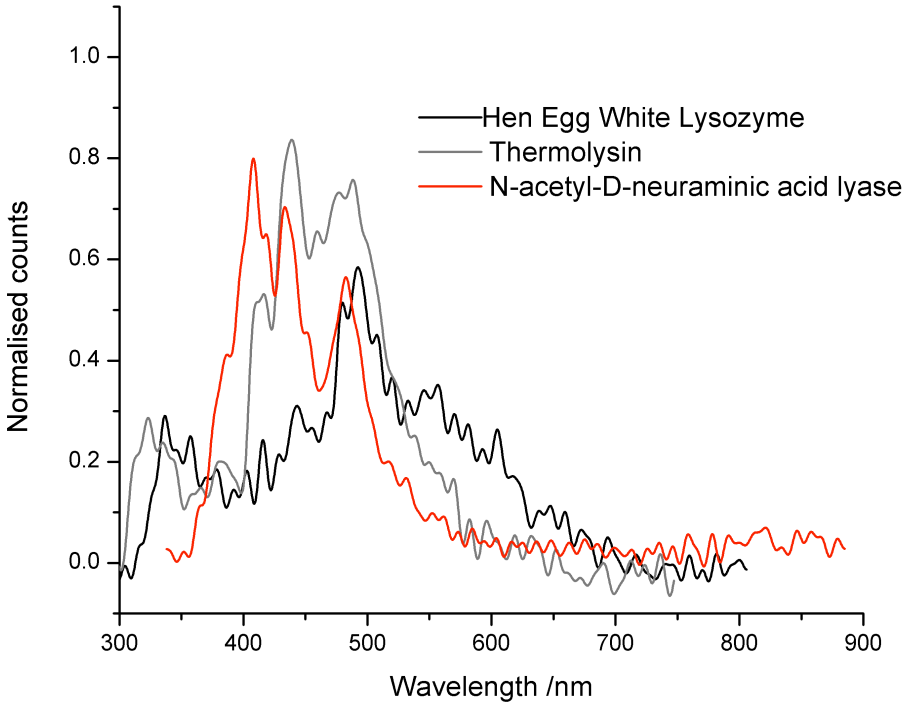

Figure 3.6: XEOL spectra of HEWL, Thermolysin and NAL after passage through a low pass FFT filter. Thermolysin data were collected at beamline I24 at Diamond Light Source and HEWL and NAL data were collected at beamline X10SA at the Swiss light Source. Spectra were accumulated over 1 second of exposure.

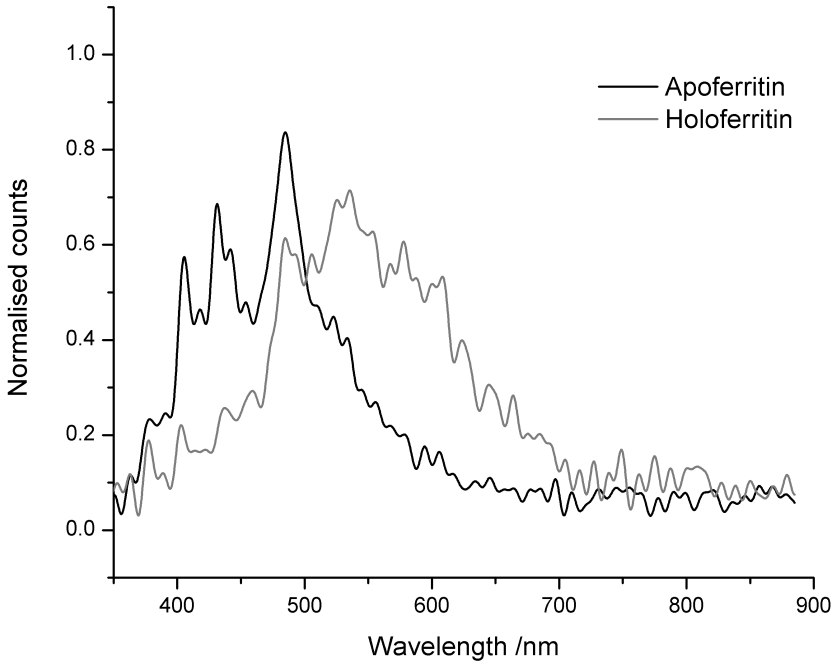

Figure 3.7: XEOL spectra of apoferritin and holoferritin recorded at beamline X10SA at the Swiss Light Source after passage through a low pass FFT filter. Spectra were accumulated over 1 second of X-ray exposure.

3.4.2 XEOL & radiation damage

3.4.2.1 XEOL as a general metric for radiation damage

The XEOL signal was observed to decay rapidly during X-ray exposure, making it a possible probe for radiation damage studies. Longer accumulation times resulted in smoother spectra, but in order to achieve a higher time resolution shorter exposure times were used in conjunction with FFT smoothing. The decay of XEOL from an apoferritin crystal is shown in Figure 3.8.

To determine whether there is a correlation between XEOL and diffraction decay rates, XEOL and diffraction data were collected simultaneously. The change in total luminescence yield for each spectrum was then compared to the decay in the intensity of individual peaks and the decay in diffraction intensity. This is shown for apoferritin in figure 3.9. In this example the XEOL decay follows a single exponential and the rate is comparable to that of the decay in diffracting power, although this shows a linear dependence on dose. Despite the comparable decay rates observed in this example, further investigation using several proteins showed that XEOL decay correlated poorly with decay in diffracting power. A wide range of XEOL decay rates were observed (Figure 3.9), even between crystals of the same type (Figure 3.10). In addition, XEOL was observed to not always follow a single exponential decay, with some crystals better described by a double exponential decay.

During these experiments XEOL and diffraction data were collected with the simplest possible experiment design: each diffraction image was collected over the same repeated angular range. The lack of correlation and consistency observed with this simplified experimental setup suggests that XEOL is not (with currently available instrumentation) a reliable metric for following radiation damage. However, further analysis showed that even with crystals of the same protein the rate of decay varied, figure 3.11. This lack of correlation unfortunately makes XEOL an unreliable general metric for the experimental analysis of radiation damage.

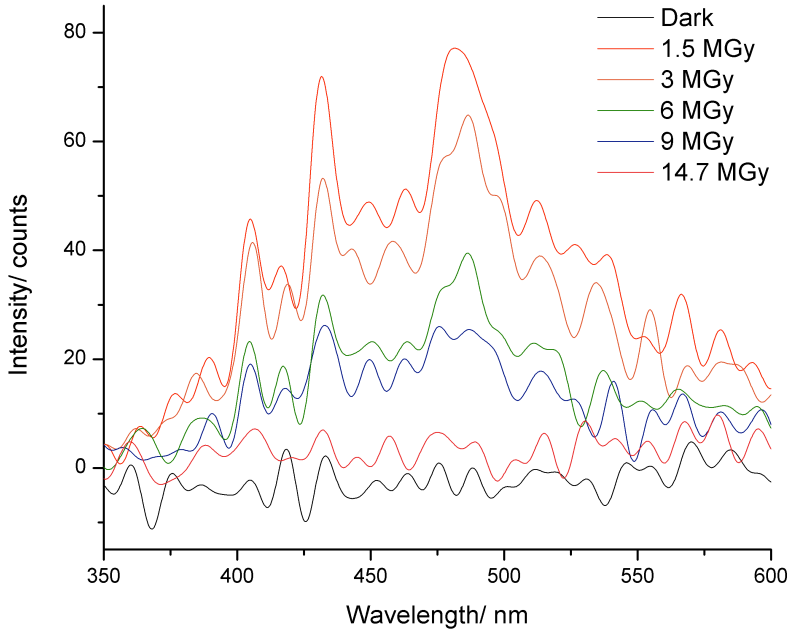

Figure 3.8: Decay of apoferritin XEOL signal as a function of increasing absorbed dose.

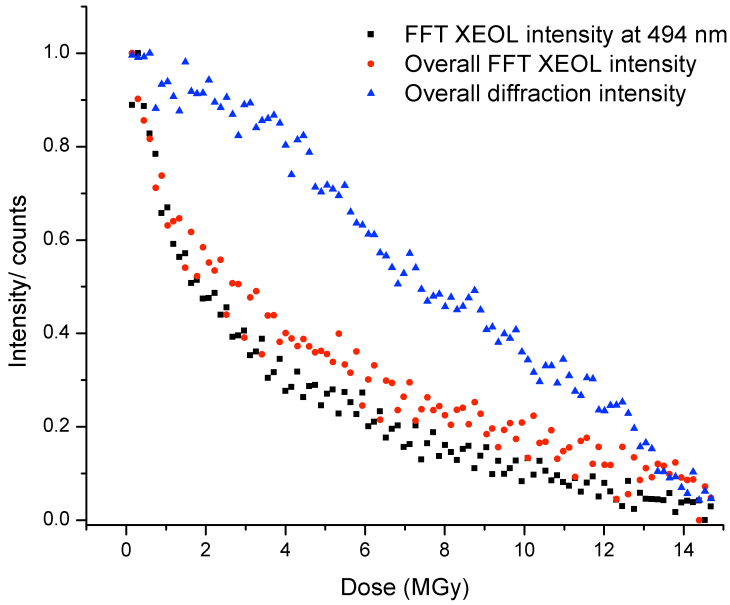

Figure 3.9: The decay in apoferritin XEOL at 494 nm (black squares), total XEOL intensity (red circles) and diffraction intensity (blue triangles) as a function of absorbed X-ray dose.

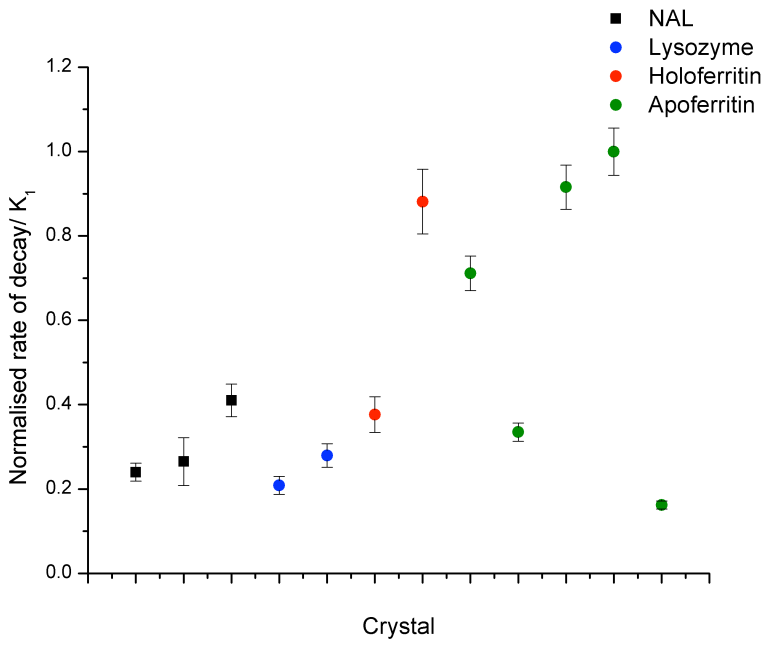

Figure 3.10: The rate constants for the XEOL decay of multiple crystals of each protein. The error bar shows the residual of the fit for each XEOL decay curve.

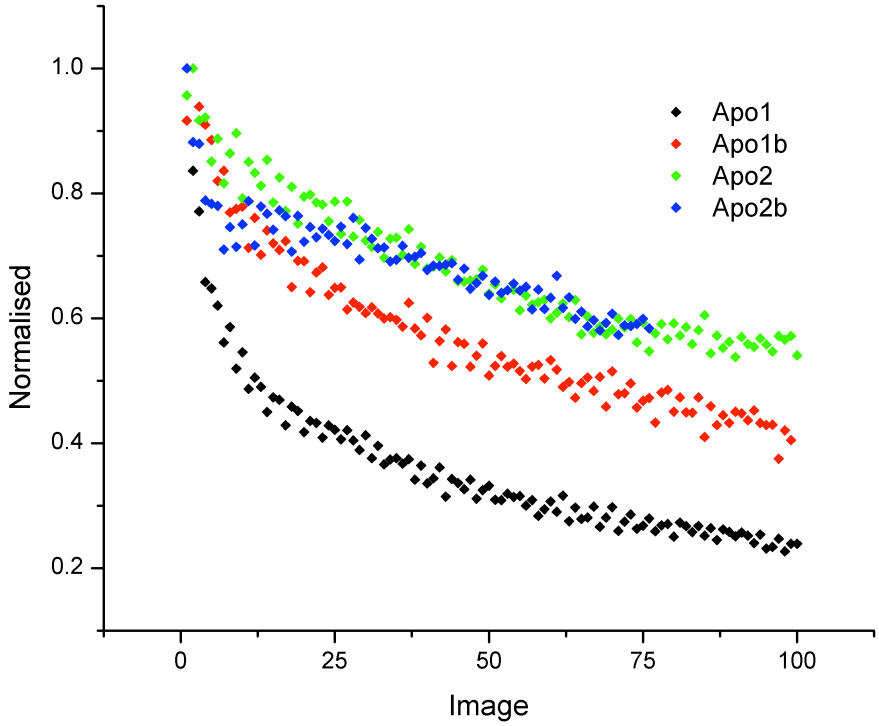

Figure 3.11: Decay of XEOL plotted as normalised intensity vs. image number for four crystals of apoferritin.

3.4.2.2 XEOL as a potential probe for site specific radiation damage

Bleaching of fluorescence is usually associated with the irreversible destruction of the fluorophore[158]. In order to determine whether a similar irreversible process occurs during the bleaching of the XEOL signal during X-ray exposure, a series of thermolysin XEOL spectra were collected using X-ray pulses spaced such that the XEOL signal could decay completely before the next pulse (Figure 3.12). The luminescence was progressively bleached over time at all wavelengths and no recovery of signal was observed, even with extended time delays (50s) between each pulse. This observation is in contrast to single crystal fluorescence experiments[158] where the signal recovers after the crystal is exposed to a low X-ray dose (<1 MGy). The dose absorbed per pulse (3.6 MGy) in these experiments is very high and so even if the rate of the irreversible destruction of the luminescent moieties is low, the damaged state will become highly populated over the course of the experiment.

However, the XEOL life time and rate of decay is not uniform over different values of λ_{max} (Figure 3.12 inset). The difference in observed rate of decay is probably due to differences in the rate of radiation damage at different sites within the protein. The rate of radiation damage in a protein is site dependent and changes according to the side chain of an amino acid and its local environment[83,110]. This suggests that with further characterisation, XEOL may provide insight into the mechanisms of radiation damage in macromolecules.

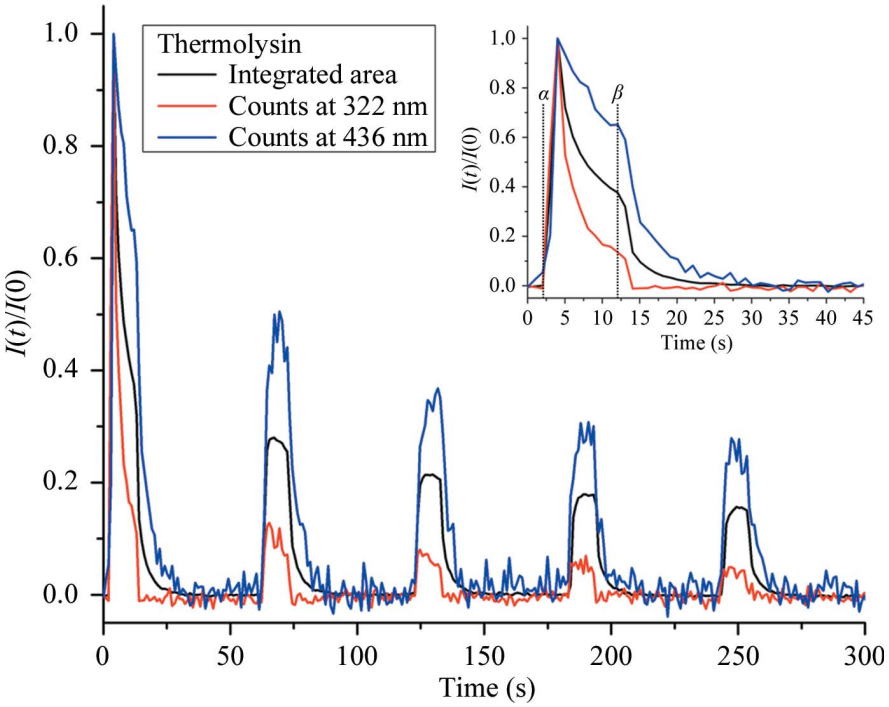

Figure 3.12: XEOL spectra show differential rates of decay as a function of wavelength and a lack of recovery between X-ray pulses. The cumulative dose absorbed by the crystal per pulse is 3.6 MGy. The inset shows an expanded view of the first pulse; the X-ray shutter is opened at $t = \alpha$ and closed at $t = \beta$. All data were collected on I24 at DLS.

3.5 Discussion

Despite being a relatively weak phenomenon for protein crystals, XEOL could easily be recorded using the microspectrophotometers at SLS and DLS. XEOL occurs for every molecule during every data collection, this makes it an ideal probe for the study of radiation damage mechanisms in macromolecules. Most spectroscopic methods require a reporter chromophore (UV-Vis, fluorescence) and all require instrumentation that is bulky and can prevent certain sample orientations from being accessed. Unlike traditional spectroscopic methods, XEOL, can be performed with a simple set-up, using a collection optic connected to a detector and spectrograph via optical fibres. This study showed that XEOL is not dependent on the sample orientation. This is in contrast to other spectroscopies, where the signal changes with orientation. Using other spectroscopic methods the sample must be therefore returned to the optimum orientation for each spectroscopic measurement to avoid complicated convolution of orientation effects with true radiation induced changes. XEOL is essentially a passive experiment that can be performed automatically during any X-ray crystallographic experiment.

XEOL in proteins arises primarily from aromatic amino acids, but the effects of local environment and quenching within crystals means that the spectra are not a simple sum of the spectra arising from the constituent parts of the crystals. Global rates of XEOL decay were found not to correlate to decays in diffracting power, making XEOL of limited use as a metric for radiation damage to protein crystals. However, the decay of XEOL spectra is non-uniform, suggesting that XEOL is sensitive to site-specific radiation damage of aromatic amino acids and may be of use in developing a better understanding of the mechanisms of radiation damage in macromolecular crystallography. XEOL spectra could thus be further characterised by mutating single residues in protein molecules and observing the effect these changes have on the XEOL spectrum. This will enable a model of the contributions to the XEOL spectra to be devised.

Recent studies combining X-ray diffraction with electron paramagnetic resonance (EPR) and UV-Vis spectroscopy have also shown that the population of radical species and the dose dependency of disulphide bond cleavage are not uniform throughout the protein.[110] The local chemical environment of cysteine residues forming disulphides appears to have a major effect on the dose at which radiation damage is observed through the formation of radicals (EPR, UV-Vis spectroscopy) causing disulphide bond breakage (X-ray diffraction). The combination of these methods has enabled an the proposal of a novel mechanism of X-ray induced cleavage of disulphide bonds in protein crystals that includes both bond breaking and repair events. The proposed model is shown in figure 3.13.

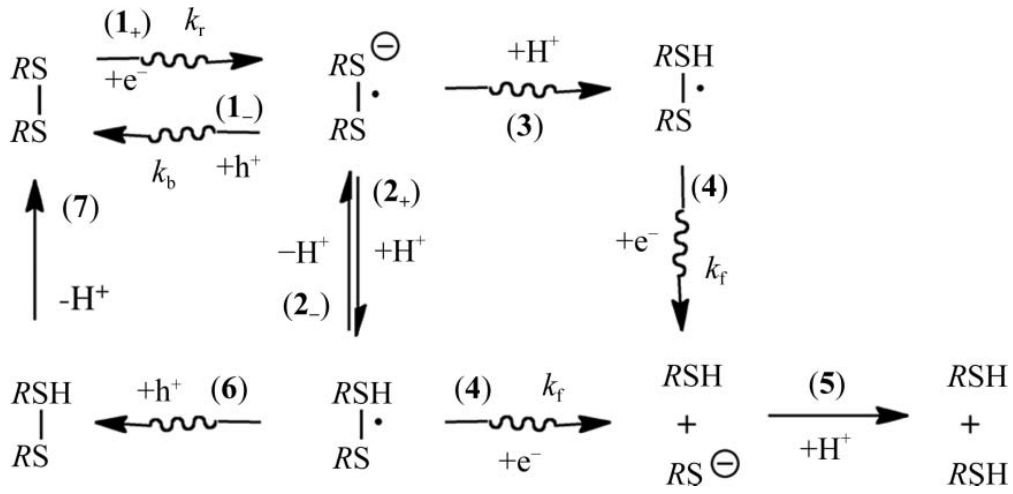

Figure 3.13: The proposed 'multi-track' mechanism for X-ray induced disulphide bond cleavage, modified from Sutton et. al.[110].

Combining XEOL with EPR could help us to identify the specific contributions of amino-acids to X-ray induced radical formation and provide a comprehensive model of radiation damage mechanisms.

Chapter 4 Photocaging aspartate decarboxylase

4.1 Introduction

Dynamic structural science is the study of the movement of atoms in molecules as chemical reactions or biological processes occur. This area of science promises to greatly increase our understanding of such processes by providing us with tools to relate molecular structure to function. Static three-dimensional images of biological molecules can provide a wealth of information about the functions and mechanisms of such systems. Further insights into mechanisms can be obtained by trapping intermediate species formed during a reaction, either chemically (using blocking groups) or by cryotrapping[32,159,160]. These structures enable the elucidation of the relationship between structure and function. However, to truly understand this relationship and to fully characterise the mechanistic pathways of biological processes it is necessary to observe the changes occurring in the system with time. The dynamic properties of biological mechanisms can be probed using NMR[2,161] and time-resolved absorption spectroscopy[162–164], however, neither of these methods can directly probe the three dimensional structure of biological molecules as they function in 'real-time'.

Time-resolved X-ray crystallography is currently the best method available to obtain data with high spatial and temporal resolution, enabling us to 'watch' chemical and biological processes as they occur. The current state-of-the-art time-resolved experiment, used in both crystallography and spectroscopy, is the pump-probe method. A short laser pulse (known as the 'pump') is used to initiate the reaction and the system is probed at a series of time-delays using either X-ray diffraction (crystallography) or light absorption (time-resolved spectroscopy). Light activation is essential to achieve synchronisation of the reaction in all of the molecules in the crystal. Without synchronisation, any time-resolved changes in the structure would be averaged out in the electron density map and so would not be resolved in the structure. Most biological reactions are not light activated, however, light activation can be achieved using synthetic substrates that have a photolabile group attached[165]. These groups known as

photocages, prevent the reaction from starting until the sample has been exposed to a high intensity pulse of light, either by sterically blocking the functional configuration of the active site, or by chemically preventing the first step of the enzymatic reaction.

4.1.1 The test system

A major aim of this thesis was the development of new time-resolved crystallographic methods that could extend such measurements to a much wider range of biological systems, including irreversible processes and systems that are not naturally light activated. To demonstrate the new methods a test system was required. The following criteria were used to select a suitable system:

1. Irreversible enzymatic reaction
2. Possible to synthesise a photocaged substrate
3. Published crystallization conditions
4. Published protein structure
5. Incomplete characterization of enzymatic mechanism

L-aspartate α-decarboxylase (ADC) satisfied these criteria and was selected as the test system. This enzyme catalyses the decarboxylation of L-aspartate to produce β-alanine (figure 4.1) as part of the pantothenate biosynthesis pathway in plants, fungi and bacteria (figure 4.2)[166]. ADC is not present in mammalian cells and has been identified as a possible drug target against *Mycobacterium tuberculosis* in humans [167]. Crystallization conditions have been published resulting in a range of structures including the wild-type and a number of single residue variants[168169]. ADC exists as a homotetramer with a 6-stranded β-barrel tertiary structure formed upon oligomerisation.

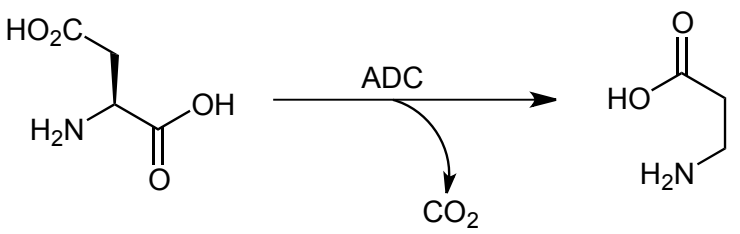

Figure 4.1: Decarboxylation of L-aspartate by ADC to form β-alanine

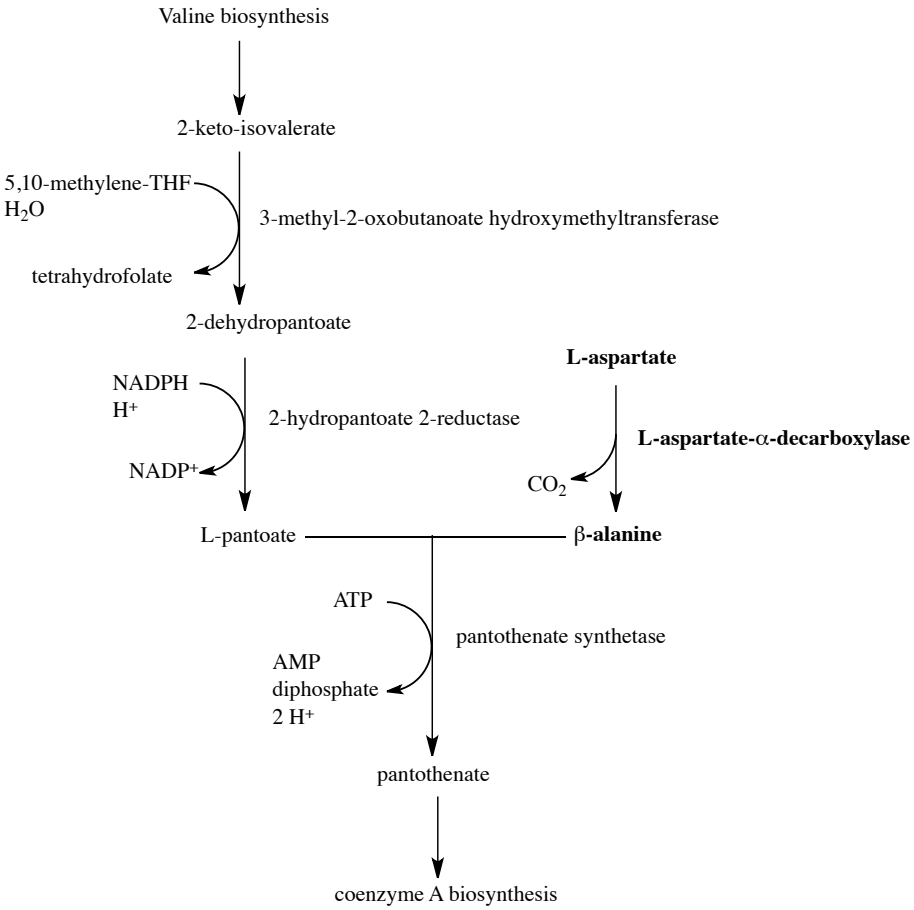

Figure 4.2: Pantothenate biosynthesis pathway, the role of ADC is highlighted in bold. Figure modified from Webb et. al.[166]

The enzyme is expressed as an inactive pro-protein (π-chain) which is activated by cleavage of the bond between Gly 24 and Ser 25, this results in two chains (α and β) with a pyruvoyl group at the N-terminus of the α-chain, Figure 4.3, 4.4. The mechanism of this activation has been described as an intramolecular N→O acyl shift, the autocatalytic *in vitro* activation has been attributed to PanZ, the two proteins form a 4:4 heterooctameric complex whose formation is dependent on the presence of coenzyme A (CoA)[170].

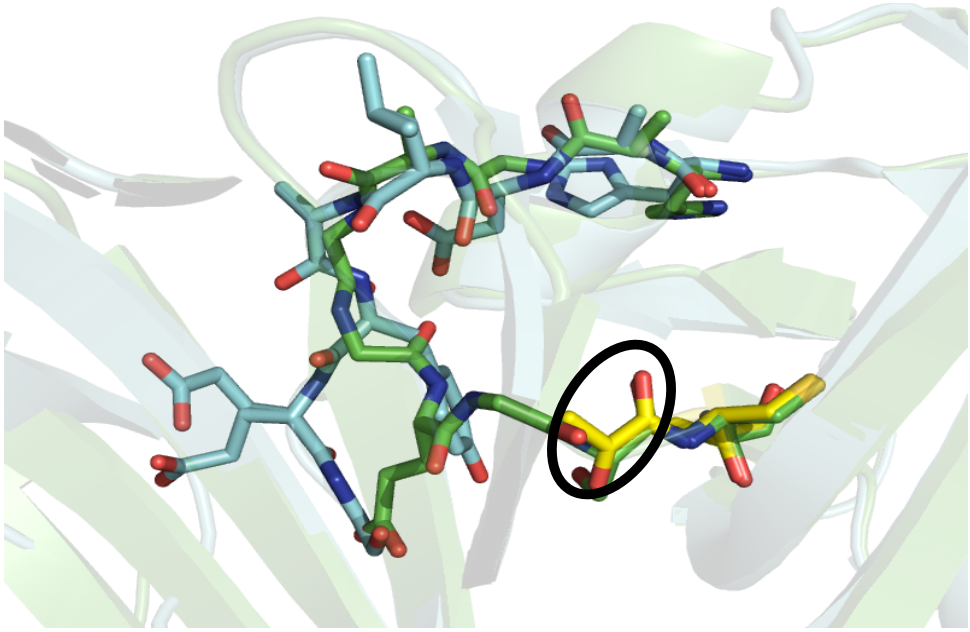

Figure 4.3: Crystal structure of L-aspartate α-decarboxylase, the inactive pro enzyme is shown in green. The two chains of the activated protein are shown in blue (β) and yellow (α), the pyruvoyl N-terminal residue is circled.

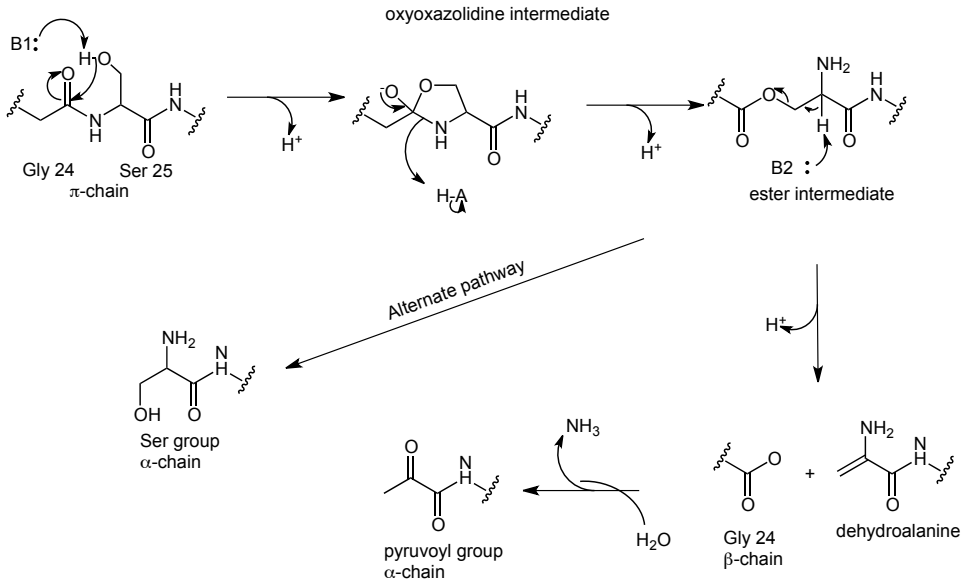

Figure 4.4: Proposed mechanism for the *in vitro* activation of ADC. Modified from Ramjee et. al.[171]

The yield of covalently bound pyruvoyl is only 70% due to ester hydrolysis in the autocatalytic cleavage resulting in the formation of a terminal serine residue at position 25[171]. This 70:30 ratio is often observed in crystal structures of the activated enzyme, however, the low occupancy of the serine residue means it is not always visible in the electron density.

We have identified the threonine residue at position 57 as the base identified in the activation mechanism shown in figure 4.4. The structure of ADC with a point mutation at position 57 from threonine to valine (T57V) was solved; the data and refinement statistics for T57V are given in table 4.1. T57V and wild-type ADC were isostructural, except for the region surrounding the site of activation (residues 16-26). A comparison of the structures is shown in figure 4.5 for both protomers.

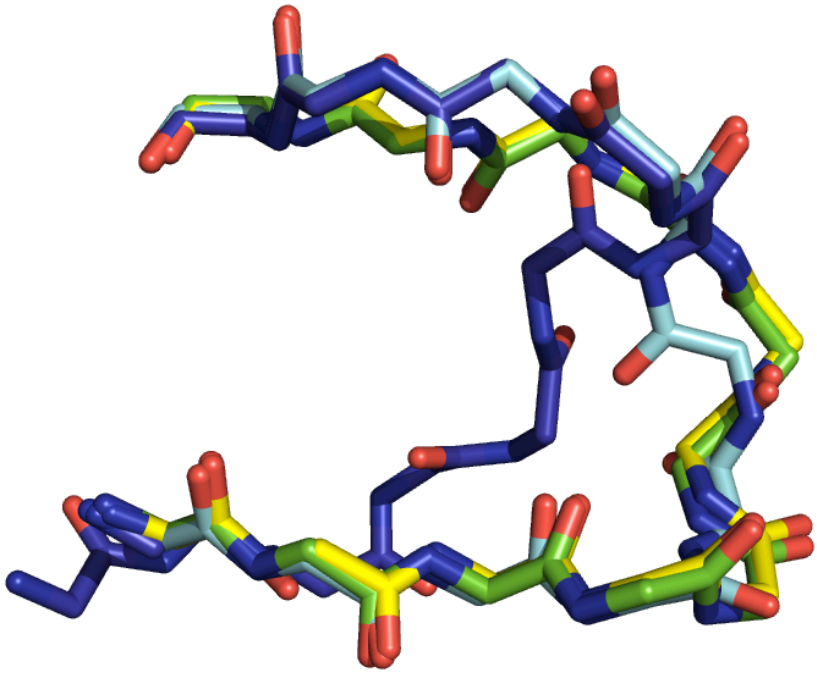

Figure 4.5: Overlay of residues 17-27 from the two protomers of unprocessed wild-type ADC (PDB:1AW8, cyan - protomer A, blue – protomer B) and T57V (green - protomer A, yellow – protomer B).

The major contribution to the structural rearrangement of this region is the presence of a single molecule of the cryoprotectant, malonate, bound into the active site of the T57V mutant (Figure 4.6). The presence of malonate in the T57V structure indicates that the loss of the hydrogen bond between the carbonyl of Gly24 and the β-hydroxyl of Thr57 leads to a rearrangement of the backbone relative to the unprocessed WT.

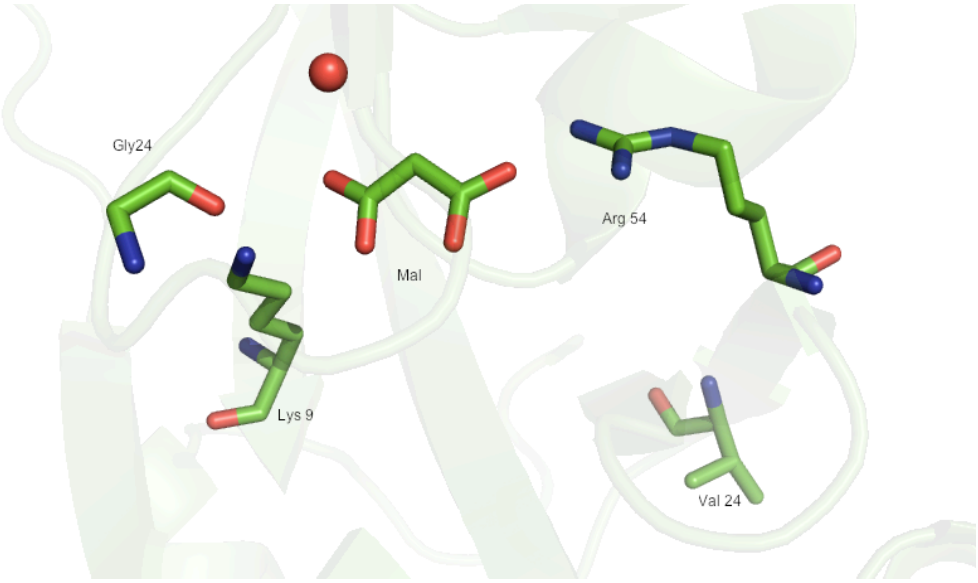

Figure 4.6: T57V active site with malonate forming interactions with Arg 54 and Lys 9. The positions of V 57 and Gly 24 are highlighted.

Dataset	T57V
Source	ID14-4, ESRF
Space group	$P6_122$
Wavelength (Å)	0.9795
Unit cell parameters (Å)	a = 69.9, b = 69.9, c = 217.7
Resolution range (Å)	26.46 – 1.62 (1.67 – 1.62)
No. of unique reflections	37850
Multiplicity	4.4 (4.3)
R_{merge}	0.08 (0.48)
Average I/σ(I)	7.4 (1.4)
Completeness (%)	97.8 (99.9)
Wilson B (Å)	16.1
R factor (%)	18.5
Rfree (%)	21.7
r.m.s.d. bond length (Å)	0.028
r.m.s.d. bond angles (deg)	2.72
PDB code	4AZD

Table 4.1: Data collection and refinement statistics for T57V

When activated the enzyme covalently binds L-aspartate to Pyr 25 forming an iminium ion, the mechanism for this reaction is shown in figure 4.7. This intermediate undergoes base catalysed decarboxylation to form β-alanine, which is then released from the active site. This mechanism has been deduced by chemical trapping of the imine intermediate using sodium cyanoborohydride as a reducing agent[171]. The structures of the natural intermediate species has not been previously determined using conventional X-ray crystallographic

techniques, and this is presumed to be because the reaction is not reversible and the life-time of the second iminium and bound β-alanine is very short. This is, therefore, an ideal system to test new methods developed in this thesis, which will provide new insight into the protein dynamics associated with the catalytic turnover of the enzyme. By probing this mechanism using sub-second time-resolved X-ray crystallography it should be possible to determine the structures of the intermediate species along the reaction pathway.

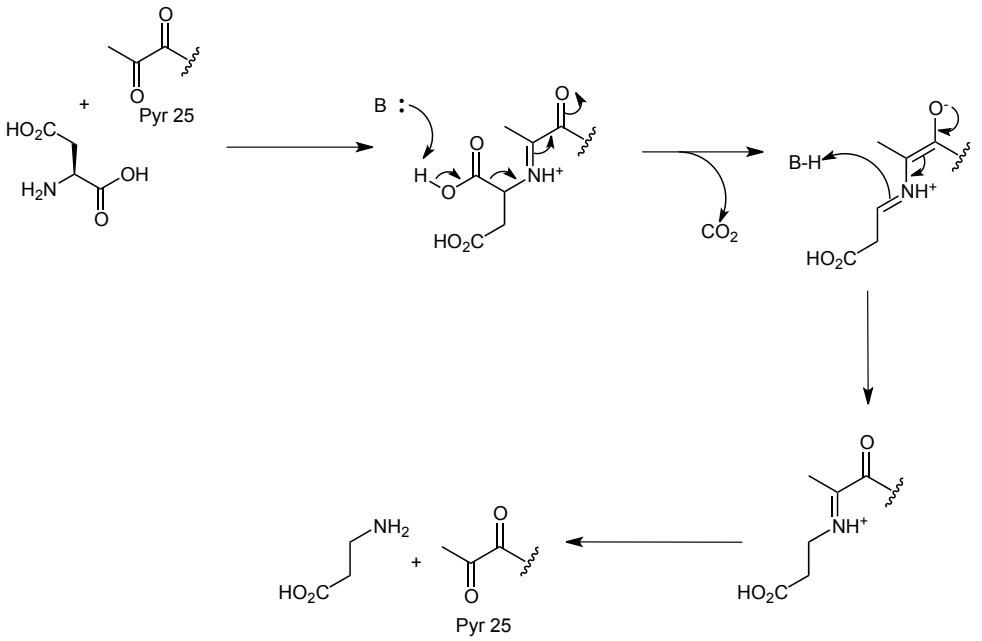

Figure 4.7: Proposed mechanism of the decarboxylation of L-aspartate by ADC. Modified from Lee et. al.[172]

To make the ADC reaction light activated a photocage was used to inactivate the substrate. For this purpose o-nitrobenzyl-methyl-L-aspartate was synthesised, the presence of the nitrobenzyl group prevents decarboxylation from occurring, however, this group is liberated when exposed to UV light. A proposed mechanism for this process is given in figure 4.8.

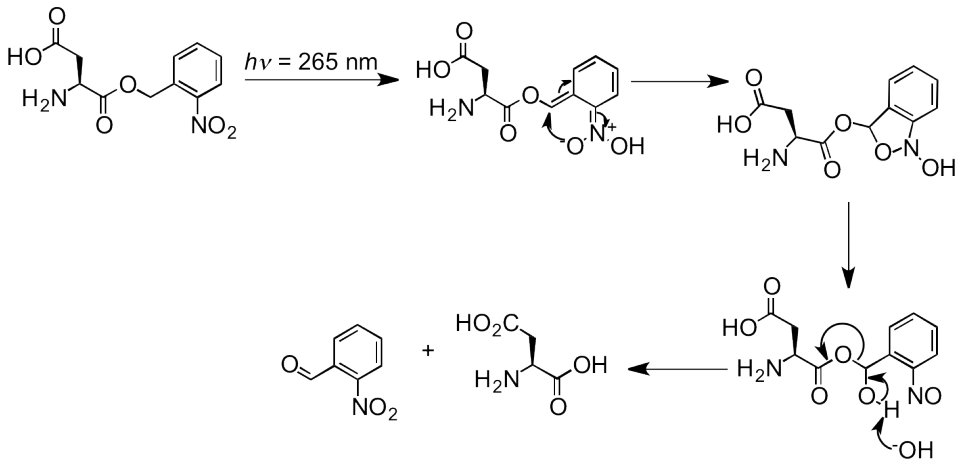

Figure 4.8: Proposed mechansims for the photo-activation of o-nitrobenzyl-methyl-L-aspartate.

4.2 Contributions to this chapter

Dr Michael Webb designed the nitrobenzyl-aspartate photocage. The photocage synthesis, protein production, crystallization and structure determination described in this chapter are entirely my own work. I also refined the structure of the T57V ADC mutant described in the introduction which has been published in the following paper:

Webb, M.E., Yorke, B.A., Kershaw, T., Lovelock, S., Lobley, C.M.C., Kilkenny, M.L., Smith, A.G., Blundell, T.L., Pearson, A.R., Abell, C. (2014) Threonine 57 is required for the post-translational activation of *Escherichia coli* aspartate α-decarboxylase. *Acta Cryst.* **D70** 1166-1172

4.3 Materials and methods

4.3.1 L-aspartate a-decarboxylase expression and characterisation

All recipes are provided in the appendix.

4.3.1.1 Transformation

Plasmids containing His-tagged ADC were provided by Dr. Michael Webb (University of Leeds). The plasmid (1 ml) was added to *Escherichia coli* BL21* (DE3) cells (50 ml) at 4 °C and the mixture was incubated on ice for 10 minutes. The cells were then heated to 42 °C for 45 seconds and subsequently returned to ice for a further 10 minutes. LB (900 ml, appendix 1.1.1) was added to the cells and the mixture was incubated for 1 hour at 37 °C with shaking (200 rpm). Samples of the cell culture were incubated on LB agar plates supplemented with ampicillin at 37 °C overnight.

4.3.1.2 Expression

Colonies of transformed cells were inoculated into LB (50 mL) with ampicillin (100 mg/mL) and the culture was incubated overnight at 37°C with shaking. A small sample of this culture (1 mL) was removed and suspended in 80% w/v glycerol (1 mL) and flash frozen. A larger sample (10 mL) was added to 1 L of autoinduction media (appendix 1.1.2) with ampicillin (100 mg/mL) and incubated overnight at 37 °C with shaking. The cells were pelleted by centrifugation (10,000 x g, 15 mins) and flash frozen in liquid nitrogen before storage at -70°C.

4.3.1.3 Purification

The cell pellet was defrosted on ice and resuspended in lysis buffer (appendix 1.1.3) and lysed by cell disruption (Constant Systems). The insoluble material was pelleted by centrifugation (30,000 x g, 45 minutes) and the protein was purified by affinity chromatography using a Nickel-NTA resin column (QIAGEN, 10 mL). DNAse I (0.1 mg) was added to the supernatant prior to loading onto the column. The column was washed with 50 mL wash buffer (appendix 1.1.4), the protein

eluted in 30 mL elution buffer (appendix 1.1.5) and collected in 5 ml fractions. The purity of the eluted fractions was determined using SDS-PAGE and the concentration of the protein was determined by UV/Vis absorption at 280 nm. The eluted fractions were combined and concentrated to 10 mg/mL (Vivaspin centrifugal concentrator, 5000 x g, 10,000 Da cut-off). The concentrated protein was then purified by FPLC gel-filtration through a Superdex 75 (10/300) column (ÄKTA purifier™), the eluent was collected in 5 ml fractions and stored at 4 °C.

4.3.1.4 Activation and activity determination

Purified ADC was activated by incubation at 60 °C for 48 hours in a heat block, the activation was characterised by the extent of cleavage of the α-chain (SDS-PAGE) and by the conversion of L-aspartate to β-alanine (NMR, §4.3.1.5).

4.3.1.5 Determination of ADC activity by NMR

ADC (10 mM) was incubated with Aspartate (1 mM) at 37 °C for 24 hours, 10% v/v D_2O was added and the solution was analysed by H^1 NMR at 500 MHz (Bruker 500 Ultra-shield™) with pre-saturation of the water peak (Figure 4.9).

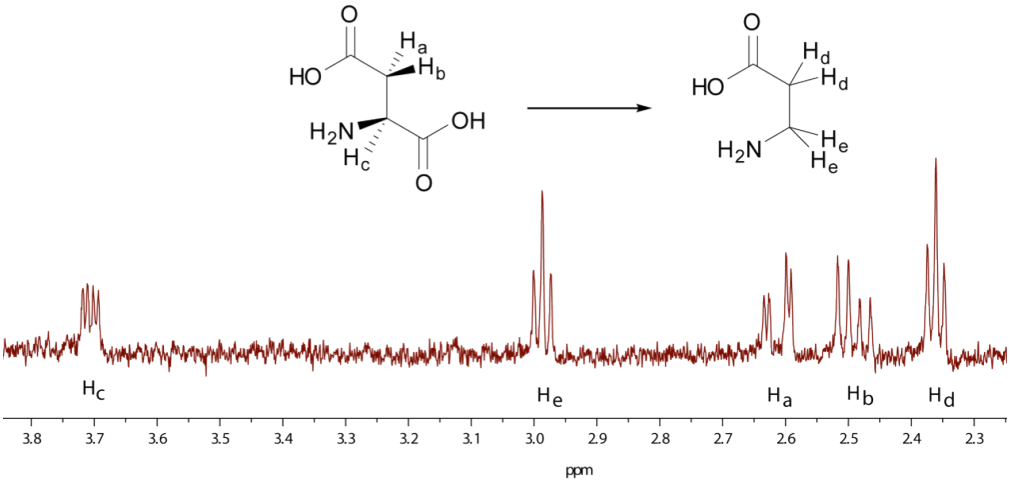

Figure 4.9: ^{1}H-NMR of ADC and L-Aspartate mixture, showing the partial conversion of L-Aspartate to β-Alanine. **L**-asp: ^{1}H NMR (501 MHz, H_2O+D_2O) δ (ppm): 3.72 (dd, *J* = 7.9, 4.9 Hz, 1H), 2.68 (dd, *J* = 17.0, 3.5 Hz, 1H), 2.49 (dd, *J* = 16.8, 8.8 Hz, 1H). β-ala: ^{1}H NMR (501 MHz, H_2O+D_2O) δ (ppm): 3.71 (dd, *J* = 8.2, 4.1 Hz, 1H), 2.99 (t, *J* = 6.8 Hz, 1H), 2.61 (dd, *J* = 17.6, 3.9 Hz, 1H), 2.49 (dd, *J* = 17.1, 8.4 Hz, 1H), 2.36 (t, *J* = 6.7 Hz, 1H).

4.3.2 o-nitrobenzyl-methyl-L-aspartate synthesis

The photocaged aspartate, o-nitrobenzyl-methyl-L-aspartate (NZD) was synthesised in two steps. The first was nucleophilic aromatic substitution via an addition-elimination mechanism of 2-nitrobenzyl bromide with Boc-Asp-OtBu (Scheme 4.1). The second step was deprotection by treatment with acid, in this step the Boc and t-Bu groups were removed simultaneously (Scheme 4.2).

4.3.2.1 Synthesis of o-nitrobenzyl-Boc-asp-OtBu

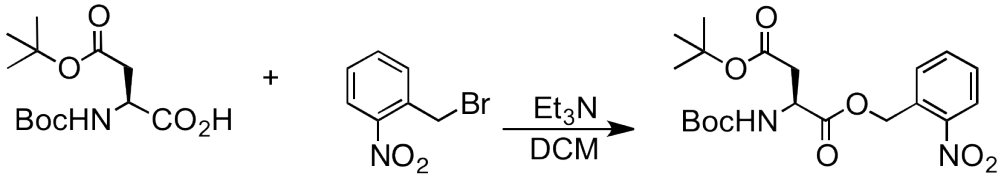

Yield: 61%

Reaction Scheme 4.1: Synthesis of o-nitrobenzyl-Boc-asp-OtBu

Boc-asp-OtBu (1.0 g) and ET_3N (2.48 mL) were added to anhydrous DCM (28 mL) under nitrogen at 0 °C. The mixture was then stirred at

0°C for 10 minutes and then at room temperature overnight. Ethyl acetate was added and the compound was washed with water, $NaHCO_3$ and sat. NaCl. The organic layer was then dried with $MgSO_4$, filtered and the solvent was evaporated to leave a pale yellow oil. The oil was dissolved in DCM (20 mL) and column chromatography was performed (30 g silica, 2:1 hexane:ethyl acetate), the eluent was collected in 5 mL fractions which were analysed by TLC to identify the product. Fractions 14 – 26 were evaporated to give a pale yellow oil (0.9 g, 61% yield). **LC-MS**: 424.1 m/z

4.3.2.2 Deprotection of o-nitrobenzyl-Boc-asp-OtBu to o-nitrobenzyl-L-aspartate

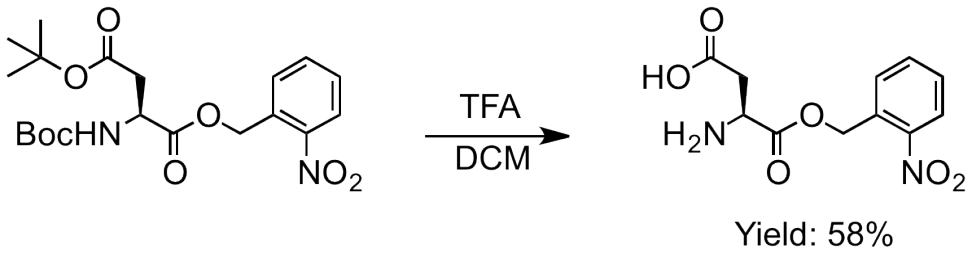

Yield: 58%

Reaction Scheme 4.2: Synthesis of o-nitrobenzyl-L-aspartate.

o-Nitrobenzyl-Boc-asp-OtBu (0.9 g) was dissolved in anhydrous DCM (20 mL) and TFA (30 mL) was added slowly. The solution was stirred at room temperature for 2 hours. After 2 hours the solution was analysed by LC-MS to confirm the reaction was complete. The solution was covered to exclude ambient light, the TFA and DCM were removed by rotary evaporation and the resulting oil was frozen (-20 °C) to leave a pale yellow solid (0.83 g, 58%). The final product was analysed by LC-MS and NMR (Figure 4.10) and was then stored at -20°C.

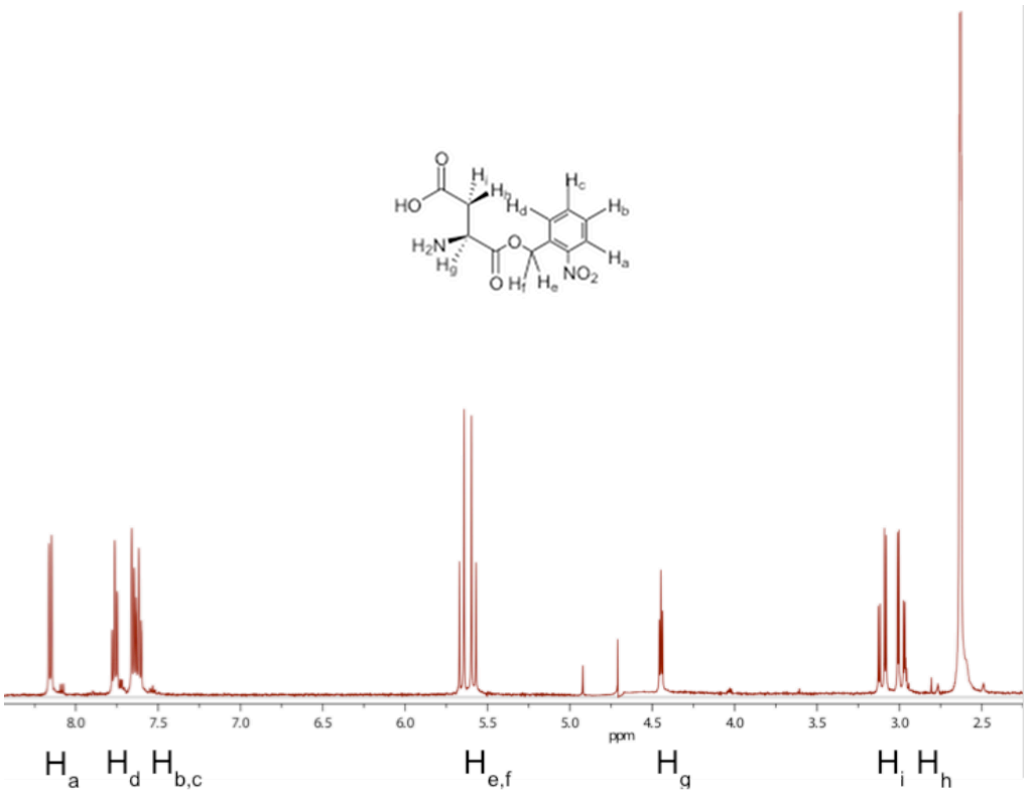

Figure 4.10: ^{1}H NMR of o-nitrobenzyl-L-asparate. ^{1}H NMR: (501 MHz, H_2O+D_2O) δ (ppm): 8.18 (d, *J* = 1.3 Hz, 1H), 7.75 (t, *J* = 1.3 Hz, 1H), 27.64 (m, 2H), 5.6 (q, *J* = 5.9, 2.5 Hz, 1H), 3.0 (ddd, *J* = 9.0, 2.5, 1.3 Hz, 1H). LC-MS: 268 m/z.

4.3.2.3 Spectroscopic analysis of o-nitrobenzyl-L-aspartate

Solution phase UV/Vis spectra of the photocaged substrate were recorded before and after photolysis to determine the peak absorption wavelength of the compound and to provide preliminary data for the crystallographic experiment. The photocage [1 mg] was dissolved in 100 mL milliQ H_2O. The UV/Vis spectra were collected between 200 – 800 nm with a Cary50 spectrophotometer. A 'dark' spectrum was recorded from the sample with minimal exposure to ambient light, the sample was then exposed to blue LED light for 1 hour before recording the second spectrum of the 'light' compound.

4.3.3 Crystallisation of ADC for photocage studies

All crystallization screens were prepared in 24-well plates using the hanging drop vapour diffusion method. The conditions were based on those previously published by Schmitzberger *et. al*.[169] The crystals obtained using the methods described in § 4.3.3.1-4.3.3.2 were soaked with NZD (1 mg) for 1 minute in the crystallization droplet. This was carried out in a darkroom to prevent photodegredation of NZD.

4.3.3.1 pH 3.8 - 4.5

The protein (in elution buffer, 5 mg/mL) was crystallised in a 1:1 mixture with 0.1 M Citrate (pH 3.8-4.5) and Ammonium Sulfate (1.4-1.6 M). The plates were left for 1 week at 19 °C for crystallisation to occur.

4.3.3.2 pH 7.5 - 8

To grow crystals in conditions closer to biological pH, the protein (5 mg/mL) was crystallised in a 1:1 mixture with 0.15 M Tris (pH 7.5 – 8.0) and 1.2 – 1.9 M Ammonium Sulfate. Crystals were grown for 2 months at 19 °C.

4.3.3.3 Microcrystals

Microcrystals were obtained by using a higher concentration of protein. The protein (10 mg/mL) was crystallised in a 1:1 mixture with 0.1 M Citrate (pH 3.8 – 4.5) and Ammonium Sulfate (1.4-1.6 M). The plates were left for 2 - 3 weeks at 19 °C to crystallise.

4.3.3.4 Co-crystallisation with NZD

Although the NZD appeared pure by mass spectrometry any small fraction of uncaged aspartate could bind preferentially in the active site. In an attempt to avoid this, ADC (5 mg/mL) was incubated with NZD (100 mg/mL) at 37 °C overnight in the dark. This allowed the enzyme to convert any uncaged aspartate into β-alanine leaving only the photocaged aspartate to bind in the active site. Crystallization screens were attempted using all of the conditions described above. All preparation involving NZD was carried out in a darkroom to prevent photodegradation.

4.3.3.5 Crystal Harvesting

All of the crystals obtained using the above methods were cryo-protected in glycerol (20% v/v, 1 minute soak) and then flash cooled in liquid nitrogen. They were then mounted in either a nylon loop (for crystals between 50 – 500 mm) or on MiTeGen MicroMeshes™ (for crystals < 50 mm) (Figure 4.11).

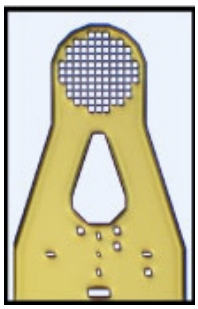

Figure 4.11: MiTeGen MicroMesh™ with 25 (m grid-spacing, meshes with 10 (m grid-spacings were also used for smaller crystals.

4.3.3.6 In-situ growth of microcrystals

Harvesting the microcrystals was not a trivial procedure and so, to address this, conditions were screened to enable the microcrystals to be grown *in-situ* (directly on the MicroMesh). First, to avoid the need to cryo-protect the crystals before mounting, 20% v/v glycerol was added to the crystallisation solution (0.1 M Citrate (pH 3.8 – 4.5) and Ammonium Sulfate (1.4-1.6 M)) prior to mixing with the protein. This resulted in the crystallisation taking longer, however, it did not appear to affect the formation of microcrystals.

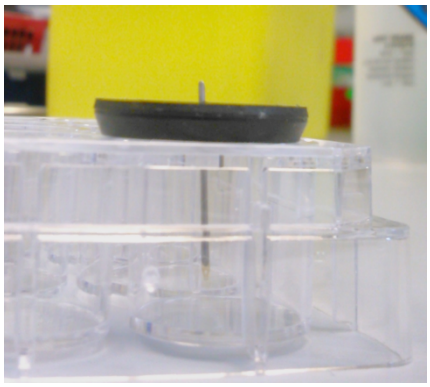

Figure 4.12: A mesh-pin was used to pierce a septum; this allowed the mesh to be suspended above the crystallisation solution. The well was sealed using a small amount of vacuum grease between the plate and septum, as with traditional hanging drop plates.

Secondly, the set-up shown in figure 4.12 was developed to enable crystals to be grown directly on a micromesh mount. In this setup the protein/crystallisation solution mixture is applied to a mesh (with 10 µm and 25 µm gaps) in a thin layer. The mesh is then suspended above the crystallisation solution in a sealed well, using a rubber septum, allowing crystals to form through a process analogous to hanging drop crystallisation.

The crystallization mixture was prepared by missing the protein (10 mg/ml) with the pH 3.8-4.5 crystallisation solution in a 1:1 ratio. A 5 ml droplet was then placed on a glass slide and the mesh quickly swirled the solution to completely coat it in the mixture. The mesh was then suspended above the crystallisation solution and left for 2-3 weeks at

19 °C to allow crystals to form. To screen for crystal growth, the mesh was placed into a re-useable cryobase before being flash cooled in liquid nitrogen and placed under a microscope in the presence of a cryostream to check for crystallization. Once the crystallisation conditions had been verified this initial screening step was omitted and the meshes were directly screened for diffraction at beamline I24 (DLS) using the gridscan method.

4.3.4 Single crystal spectroscopy analysis of ADC with NZD

Single crystal spectra were recorded using the off-axis spectrophotometer developed for I24 (DLS) off-line. To observe the decaging of NZD in ADC crystals the crystals were first soaked with NZD before washing in mother liquor to reduce spectroscopic artefacts due to any unbound photocage in the solution. The crystals were then flash cooled in liquid nitrogen (100 K) and mounted onto a goniometer in the spectrophotometer under a cryostream. The temperature of the cryostream was slowly ramped from 100 K to 200 K at a rate of 0.8 K s^{-1}. Spectra were recorded in 30 s cycles with 50 accumulations of 100 ms exposures for each time-point.

After these initial experiments the spectrophotometer was installed on beamlines I04 and I24 (DLS). The above experiment was repeated on beamline I04, however in this case, diffraction data were collected before and after the temperature ramp (see § 5.3.5).

The spectra were analysed using OriginPro9. The intensities of specific spectral peaks were extracted as time-slices and plotted to display the changes occurring over time. The temperature dependent intensities were normalised by subtraction of the baseline, the data were plotted and the best fit of the curve was calculated as an initial attempt to characterise the rate of cleavage of the photocage over a range of temperatures.

4.3.5 X-ray data collection

A number of experiments were performed before collecting time-resolved data, to characterise the behaviour of the system and determine suitable data collection strategies. Initial datasets for the dark and light structures were obtained from large (50-200 mm) single crystals at beamlines I04 and I24 at DLS.

4.3.5.1 ADC soaked with NZD

ADC crystals soaked with NZD were cryoprotected in glycerol (10% v/v, 10 min soak), mounted in nylon loops and flash cooled in liquid nitrogen. As a precaution, light was excluded from the sample during preparation and data collection. Crystals were aligned using the gridscan method (box size 50 μm^2, beam size 150 μm^2, beam transmission 5%). Data were collected on beamline I04 (DLS) with a CCD detector (ADSC-Q315). The data collection parameters are shown in table 4.2.

Dataset	NZD
Number of images	200
Exposure time/image (s)	1
Oscillation/image (()	0.5
Detector distance (mm)	274.4
X-ray wavelength (Å)	0.97625
Transmission (%)	30

Table 4.2: Data collection parameters used for datasets NZD.

4.3.5.2 Dark structure of ADC cocrystallized with NZD (DARK)

Analysis of the above datasets revealed that the NZD had photolysed. The experiment was repeated using a new batch of NZD cocrystallized with ADC to obtain 'dark' structures, with the intact photocaged aspartate. The crystal samples were prepared using the method described in section 4.3.3.4. They were cryoprotected (glycerol 10% v/v, 10 min soak), mounted in nylon loops and flash cooled in liquid nitrogen. Light was excluded during sample preparation and data collection, sample alignment was performed using a gridscan (box size 25 μm^2, transmission 2%). Data were collected on beamline I24 (DLS) with a photon counting detector (Pilatus 6M). The data collection parameters are given in table 4.3.

Dataset	DARK	LIGHT
Number of images	900	900
Exposure time/image (s)	0.2	0.2
Oscillation/image (°)	0.2	0.2
Detector distance (mm)	275.0	273.4
X-ray wavelength (Å)	0.97779	0.97779
Transmission (%)	10	25

Table 4.3: Data collection parameters used for the DARK & LIGHT dataset

4.3.5.3 Light structure of ADC cocrystallized with NZD (LIGHT)

To obtain the 'light' structure, ADC crystals from the same batch, cocrystallized with NZD, were exposed to blue light (265 nm, LED, 20 minutes, 5 J) prior to mounting in nylon loops, cryoprotection (glycerol 10% v/v, 10 min soak) and flash cooling. Ambient light was not further excluded after the samples were flash cooled. The crystals were aligned using the on-axis microscope. Data were collected on beamline I24 at Diamond Light Source (Pilatus 6M detector). Data collection parameters are given in table 4.3.

3.3.5.4 X-ray data collection from microcrystals

Crystals were prepared using the method described in §4.3.3.3. The crystals were mounted onto micromeshes (25 μm^2), cryoprotection conditions and sample handling techniques were identical to those described in sections 4.3.3.5. Crystals were identified and aligned using the gridscan (box size 10 μm^2, transmission 2%), the crystal co-ordinates were recorded using the in-house beamline software (GDA) and used to define positions for data collection. Diffraction data were collected in 50° wedges from 27 microcrystals, the parameters are given in table 4.4.

Dataset: Merge Dark	Xtals 1, 2, 6	Xtals 3-5, 11-27	Xtals 7-10
Number of images	25	25	25
Exposure time/image (s)	0.2	0.2	0.2
Oscillation/image (°)	0.2	0.2	0.2
Detector distance (mm)	518	399.7	333.5
X-ray wavelength (Å)	0.97779	0.97779	0.97779
Transmission (%)	25	25	25

Table 4.4: Data collection parameters used for the 'merge dark' dataset

4.3.5.5 Room temperature X-ray data collection

Room temperature diffraction data were collected on beamline I24 (DLS). Spectrophotometer optics were installed onto the beam line in an off-axis geometry and used to focus a 265 nm laser onto the crystal samples (50 x 50 mm focal point). The samples were held at room temperature under a humidified gas stream (HC1, 96% humidity)[173] to prevent drying of the sample.

To characterise the amount of radiation damage occurring in the samples at room temperature, 100 images were collected using the parameters given in table 4.5. Each image was taken from the same area of the crystal over an oscillation range of 0.5°. The total Bragg intensity of each diffraction image was calculated using Labelit and was used as a parameter to estimate the extent of global radiation damage to the sample.

Crystals (~50 μm) were used to collect complete datasets in 120° wedges before and after UV laser illumination (200 s, 400 μm fibre). Crystals were aligned using the grid-scan tool (10 μm^2, 15% transmission). The data collection strategies for the structures shown in section 4.4.4. are given in table 4.5.

Dataset	**Dark_rt_ merge**	**60s_light**	**120s_light**	**200s_light**
Number of images	60	60	60	60
Exposure time/image (s)	0.04	0.04	0.04	0.04
Oscillation/image (°)	0.5	0.5	0.5	0.5
Detector distance (mm)	325	325	325	325
X-ray wavelength (Å)	0.97779	0.97779	0.97779	0.97779
Transmission (%)	70	70	70	70

Table 4.5: Data collection parameters used for all room temperature datasets.

4.3.5.6 Laue X-ray data collection

Laue datasets from ADC crystals were collected at beamline 14-IDB, BioCars at the Advanced Photon Source (APS, Chicago). These initial experiments were performed with the aim of characterising the ADC system for the Laue experiment at room temperature, i.e. to determine whether the ADC crystals diffracts well with 100 ps pulses, whether they are particularly susceptible to radiation damage and whether there is significant overlap of the reflections in the Laue diffraction images. The crystal was capillary mounted in the beam. Each image was recorded from 7 Laue pulses with a single pulse length of 100 ps (Table 4.6).

Dataset	Laue
Number of images	14
Exposure time/image (ps)	7 × 100
Beam size (μm)	65 × 90
Detector distance (mm)	150
X-ray energy (k eV)	12

Table 4.6: Data collection parameters for the Laue datasets

4.3.6 Diffraction data processing

4.3.6.1 Single crystal data

Data were indexed and integrated using XDS[174] in space group $P6_122$. Data were scaled and merged with SCALA[175]. During this step a randomly selected subset set of reflections (5%) were defined as the free R set (to be excluded from refinement for free R analysis) and the intensities were converted to structure factor amplitudes using the French and Wilson protocol[176] implicated in cTRUNCATE[175]. A model of ADC (1AW8) was edited for use as a molecular replacement model by removal of water molecules, the pyruvoyl residue in the active site and the disordered region of the α-chain (residues 22-24). Molecular replacement was carried out using MOLREP[177]. Maximum likelihood refinement was carried out on the structure using REFMAC5[178]. After

an initial rigid body refinement (10 cycles, with hydrogen atoms) a restrained refinement was carried out (10 cycles, Bfactors treated isotropically). Real space refinement and model building was then performed using sigmaA-weighted maps in Coot[179]. Models of the photocage/substrate/pyruvoyl residue were built and libraries of the relevant restraints were calculated using JLigand[180]. The relevant models were fit into the density with the Coot fit-ligand protocol. Further iterative rounds of restrained maximum likelihood refinement and real-space model building was used to build the partially disordered region of the α-chain and add water molecules to the model. Validation of the model was carried out using Molprobity[181] and SFcheck[182].

4.3.6.2 Micro crystal diffraction data

Each wedge of data was indexed in space group $P6_122$ and integrated using XDS[174]. At this stage wedges of data that were not successfully indexed as $P6_122$ were discarded. The successfully integrated wedges were then merged together using POINTLESS[175], during this step each wedge was reindexed to match a reference (defined as the first wedge in the list to be merged). Scaling of the data was performed using SCALA[175]. The merged data was collected from crystals with varied orientations and sizes, resulting in poor merging statistics. To successfully scale the data scaling was performed iteratively, with the exclusion of low quality data (identified by poor batch merging statistics) between each run. The relative quality of the batches within the dataset was assessed using the following parameters Rmerge, Rpim and Rmeas[183]. Outlying batches of data were identified using a plot of Rmerge vs. Batch and excluded according to a cut-off value of Rmerge. This cut-off was determined by assessing the overall quality of data using the parameters Rpim, Rmeas, <I>/sigI and completeness after exclusion of batches above a certain Rmerge threshold. In the initial runs, scaling was performed by batch with the eigenvalue shifts damped by a factor of 0.2. The intensity cut-off for reflections included in scaling was lowered to 2.0 SDmin. After multiple iterations of scaling

and batch exclusion the final scaling step was performed with no damping and SDmin set to 3.0. A set of 5% of reflections were defined as the free R set and structure factor amplitudes were calculated from the intensities using the French- Wilson protocol[176]. Molecular replacement and refinement was as described above.

During this project the iterative scaling process was automated using a bootstrapping protocol by David Waterman (Diamond Light Source)[184]. In this method an initial scaling run is analysed on the fly and the results are used to automatically define the next input parameters for SCALA, *i.e*. the list of excluded datasets generated by analysis of Rmerge. The program, ABBREVIATE, reads a list of .mtz files from a data directory and prompts the user to define the convergence criteria (Rmerge, <I>/sigI, *etc*.,), the maximum number of bootstrap trials, the estimated number of wedges/images required for a complete dataset and the required completeness. The output is a scaled .mtz file with structure amplitudes. These scaled .mtz files were further processed using the method described in section 4.3.6.1.

4.4 Results

4.4.1 Crystallisation of ADC

The formation of crystals was observed over a range of timescales depending on the crystallization conditions, these are summarised in section 4.4. All crystals obtained were hexagonal bipyramidal in morphology (Figure 4.13), the largest having dimensions of ~700 x 250 x 250 µm. Large crystals (>50 µm) grew either as single crystals or in a small quantity (<10) within a single drop, however, microcrystals were always observed growing in a large quantity (>100).

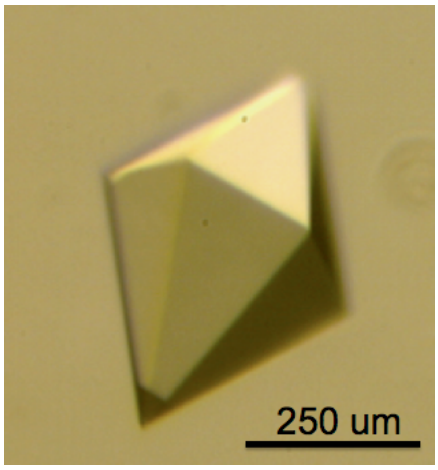

Figure 4.13: Hexagonal Bipyramidal ADC crystal grown by hanging drop vapour diffusion in 0.1 M Citrate, pH 4.0 and Ammonium Sulfate 1.6 M.

The *in-situ* growth of microcrystals was only successful for meshes with 25 µm spacings. The microcrystals appeared to form preferentially in the mesh spacings, possibly due to surface imperfections aiding nucleation.

4.4.2 Solution and single crystal spectroscopy

The solution spectrum of the 'dark' photocage solution has absorbance peaks at 200 nm and 260 nm. With exposure to light the absorbance at 260 nm increases as the absorbance at 200 nm decreases. The overlay of the spectra shows an isosbestic point at 240 nm, indicative of a simple two state system contributing to the spectra, *i.e.* the caged aspartate in the 'dark' spectrum and the liberated nitrobenzyl group in the 'light' spectrum (Figure 4.14). In this example the photocage has not been completely degraded due to the low intensity of the LED source used.

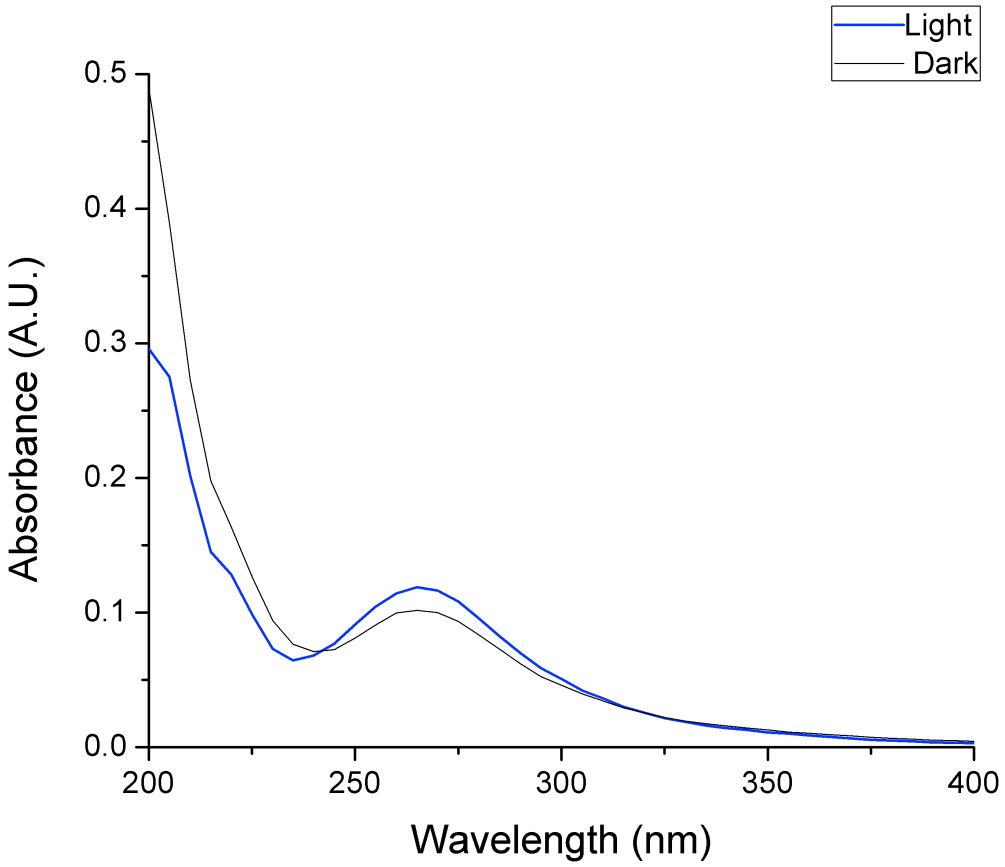

Figure **4.14**: UV-vis spectra of NZD solution between 200 and 400 nm. The 'dark' spectrum (shown in black) was recorded immediately after the sample was prepared in a dark room. The 'light' spectrum (shown in blue) was recorded after 1 hour of exposure to a blue LED light source.

Single crystal spectra were recorded at Diamond Light Source using the single crystal spectrometer built by Robin Owen, both off-line and on-line with off-axis geometry on beamlines I04 and I24.

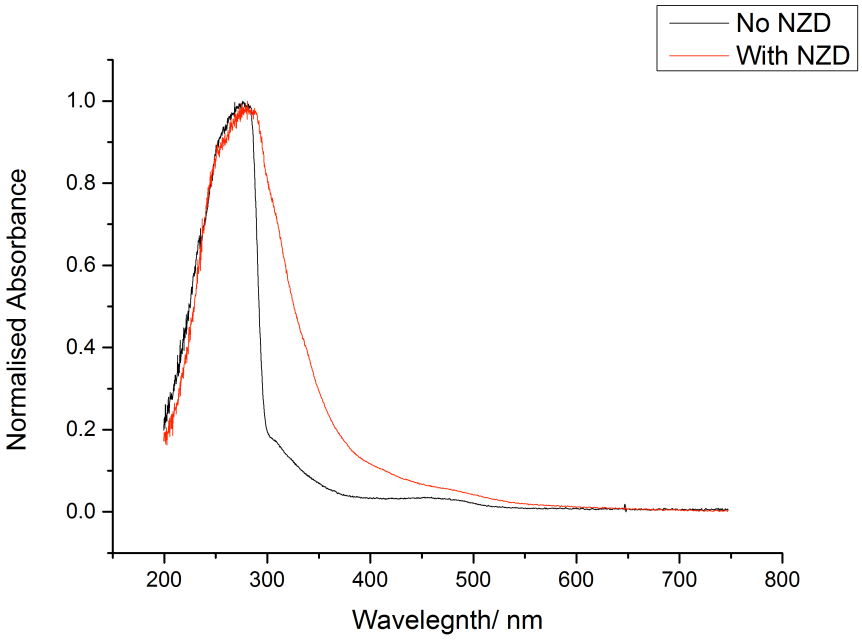

Figure 4.15: UV-Vis absoprtion spectra of ADC crystals. The black line is the spectrum of an ADC crystal with no additives, the red line is the spectrum of an ADC crystal soaked with NZD. A baseline subtraction was performed on both spectra before normalising between 0 and 1.

The single crystal spectra in figure 4.15, show the changes observed when an ADC crystal is soaked in mother liquor containing NZD. The peak at 280 nm in both spectra is due to the absorbance of aromatic amino acids, however, after soaking with NZD this peak broadens. This broadening may be attributed to the contribution of the photocage at 200 and 260 nm. Although the individual peaks cannot be distinguished due to the overlap with protein absorption, the broadness of the absorption over 350 nm corresponds to the solution spectrum of the photocage.

The crystals were initially kept at 100 K, however, as the rate of uncaging under the white light source of the spectrophotometer at 100 K was negligible, the temperature of the cryostat was ramped up to 200 K with repeated measurement of the absorbance spectra every 30 seconds (Figure 4.16).

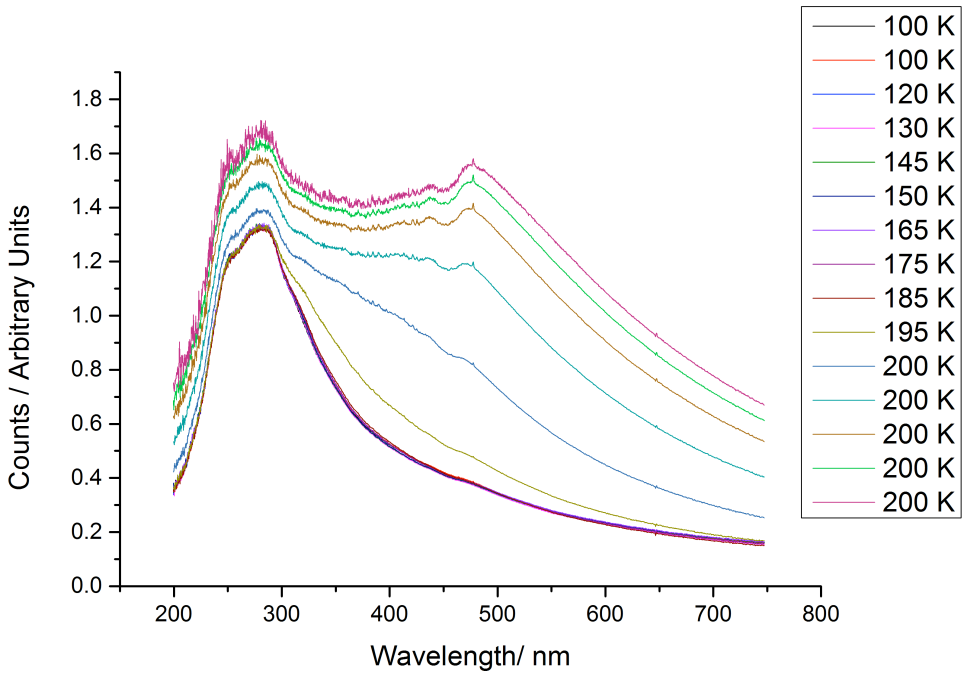

Figure 4.16: Spectra of ADC crystals + NZD recorded during a temperature ramp from 100 K to 200 K. The red line represents the spectrum recorded at time = 0 and temperature = 100 K. No spectral changes are observed before 185 K, the changes continued after the temperature stabilised at 200 K.

The overall increase in absorbance can be attributed to an increase in scattering of the crystal with the increase in temperature, due to the formation of ice crystals as the crystal warmed. Post-processing of the spectra was used to improve analysis of spectral feautures. First, a simple baseline correction was performed in which the mean absorbance between 200 - 250 nm was subtracted from each spectrum. Then, difference spectra were calculated by subtracting the spectrum t = 0 s (at 100 K) from each subsequent spectrum (Figure 4.17).

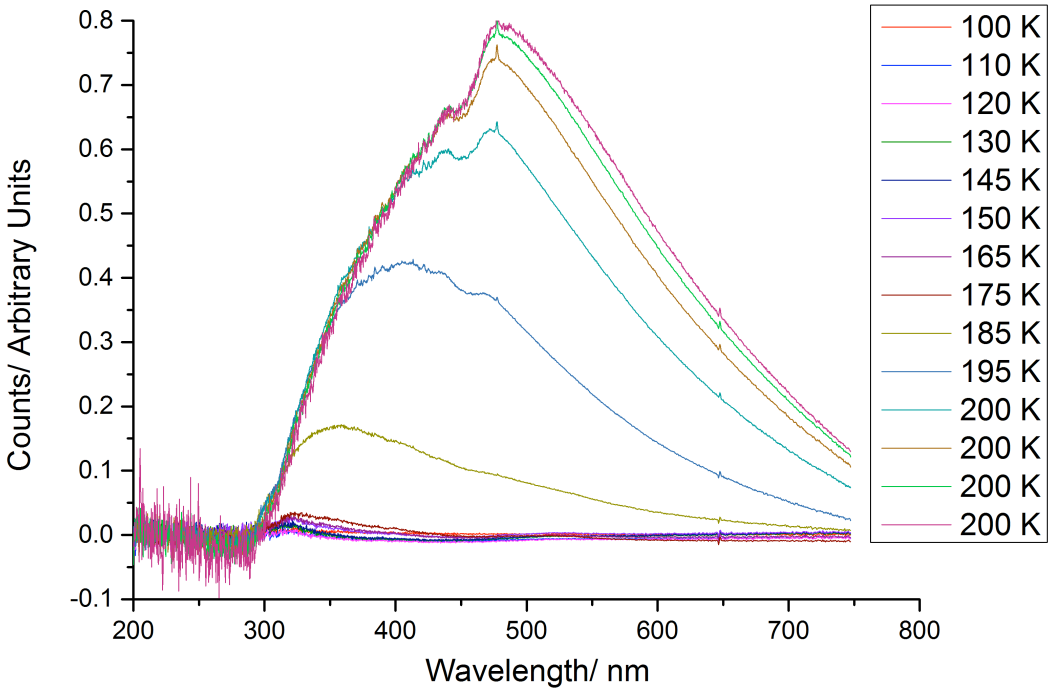

Figure 4.17: Difference spectra (t=x - t=0) of ADC with NZD, each spectrum was recorded sequentially with ramping of the cryostat temperature from 100 K to 200 K with continuous illumination from the spectrophotometer Xenon lamp.

A number of factors prevent the umambiguous assignment of the spectral features observed. These include the overlap of the protein and photocage absorption peaks and the effects of scattering from ice crystallites which causes a broadening of spectral features and an overall increase in the measured absorbance.

The absorbance at 480 nm from the raw spectra was followed over the whole temperature range, and over the time points recorded after the temperature had reached 200 K, the data from one crystal is shown in figure 4.18.

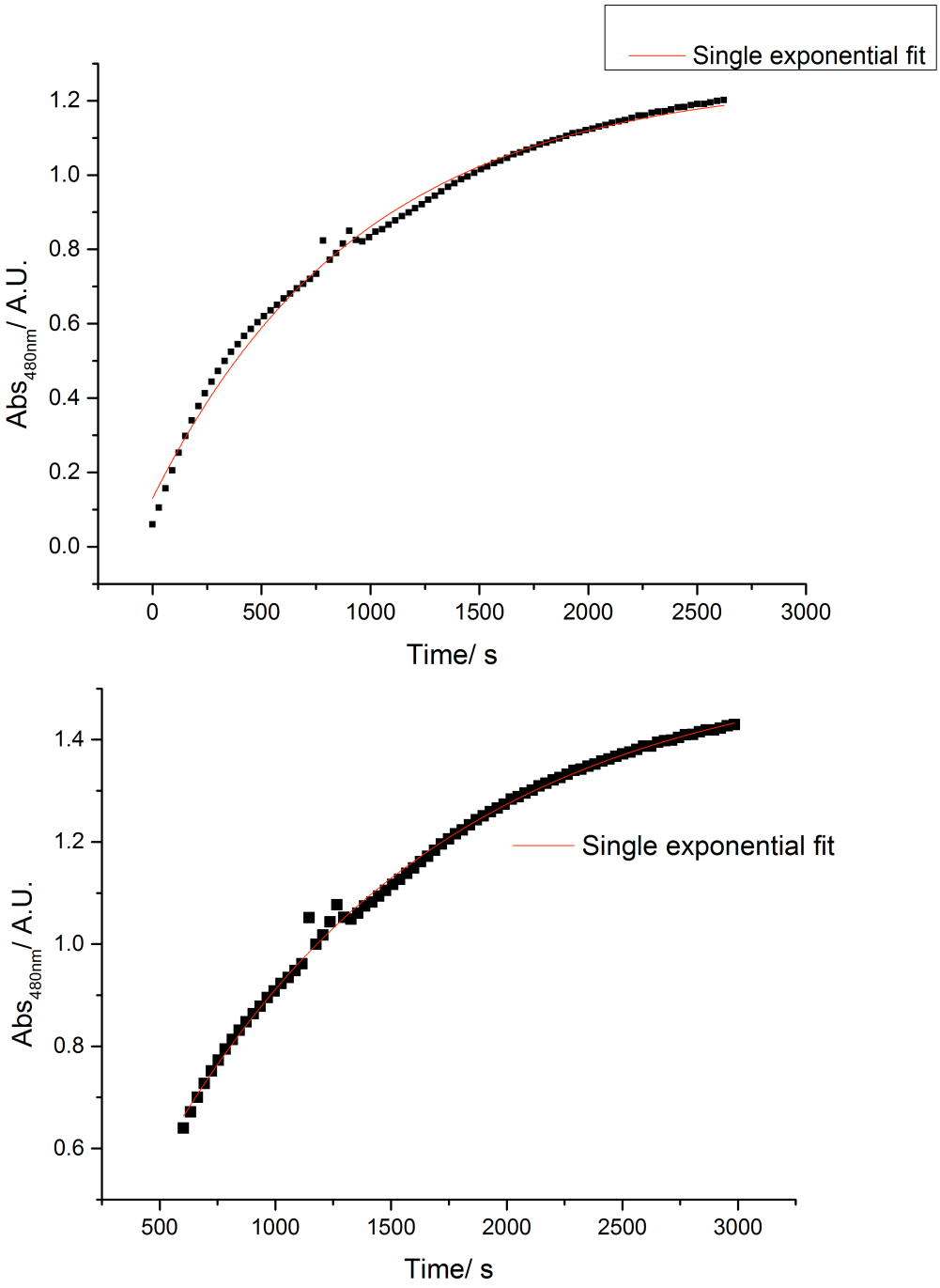

Figure 4.18: The rate of change at 480 nm extracted from the single crystal UV-vis spectrum of an ADC crystal with NZD for the whole time series (top) and for the measurements taken at 200 K (bottom).

There was no obvious correlation between the rates calculated from 4 crystals. This can be attributed to the varied conditions used in each run of the experiment, such the size of the crystals and the overall length of the time course. To study the rate of uncaging in

cryoconditions, it would be sensible to repeat these experiments at a constant temperature of 200 K.

Despite the difficulty in analysing such spectra, there are features that can be followed to make predictions about the behaviour of the photocaged substrate in the crystal at increasing temperatures. For example the feature at 480 nm appears only when the temperature has reached 185 K, it then continues to increase in intensity with temperature. This observation allows us to design a time-resolved experiment that can be performed below room temperature under a cryostat, this may necessary in the absence of a sample humidifier because the traditional capillary method of room temperature data collection is unsuitable when the use of laser initiation is required, due to the difficulty of aligning the sample in the laser and scattering of light from the capillary. It will also enable us to compare datasets collected at different temperatures in order to fully quantify the kinetic mechanism of the reaction[69].

The rate of change in the peak at 480 nm above 200 K is shown for two samples (Figure 4.18). Both time-courses were best fit with a single exponential. This suggests that the change in absorbance is determined by a two state system (*i.e*. there is a single step from reactants to products). This is in contrast to the mechanism suggested in figure 4.8 and a numerical value for the rate of uncaging at 200 K has not been calculated due to the variations in temperature ramping, sample size and the photocage concentration. Further time-resolved spectra must be collected at a constant temperature to better characterise the system.

4.4.3 X-ray crystallography

4.4.3.1 An unexpected intermediate

The first “dark” data collected from large ADC crystals soaked with NZD showed ligand density in the active site that was inconsistent with the intact photocage. This density was best modelled as the first intermediate formed in the conversion of L-aspartate to β-alanine, the Schiff base formed when L-aspartate binds to pyruvoyl 25 on the β-

chain the active site (Figure 4.19, Table 4.7). There was no evidence of electron density for the nitrobenzyl group. This was surprising as these diffraction data were collected at 100 K, from crystals mounted under red light, and with no laser initiation.

The imminium intermediate is formed when L-aspartate covalently binds to the pyruvoyl group (figure 4.7). Given the absence of laser initiation we attribute the formation of this intermediate to the preferential binding of L-aspartate impurities in the NZD sample arising from degradation of the photocage. The natural substrate, L-aspartate, is likely to bind preferentially over the NZD, so that even a small proportion of uncaged L-aspartate in the NZD sample can result in the cryo-trapped imminium intermediate.

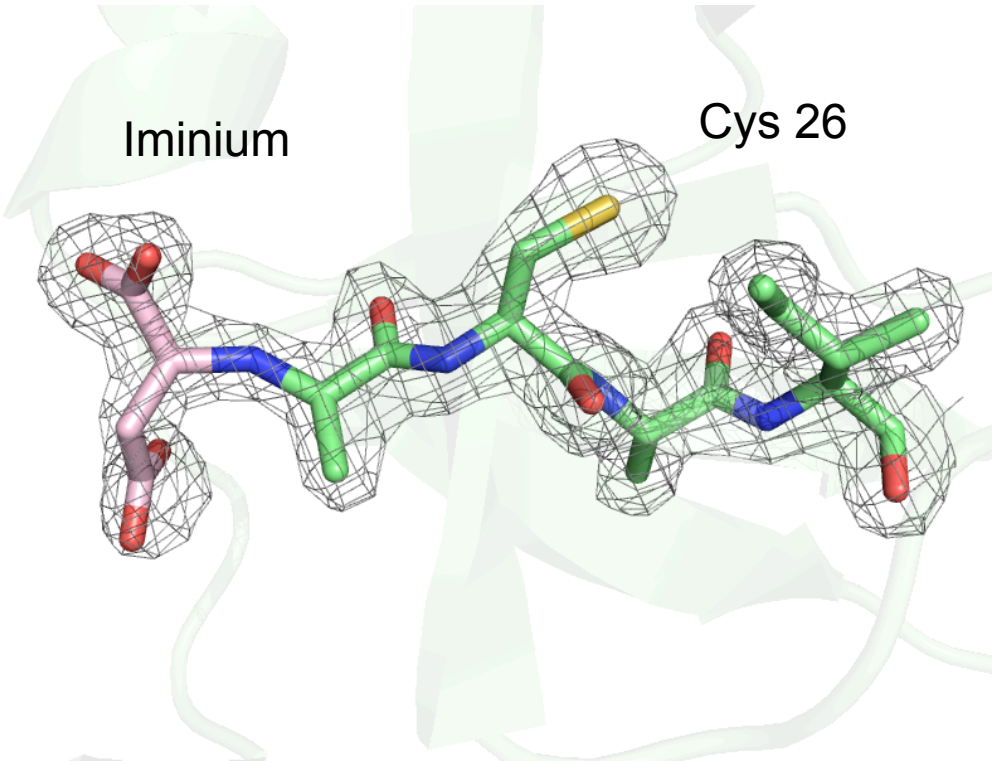

Figure 4.19: L-Aspartate (pink) covalently bound to pyruvoyl in the ADC active site (green) forming the imminium intermediate. The 2Fo-Fc electron density is shown contoured to 1 σ.

Dataset	NZD
Source	I04
Space group	P6122
Wavelength (Å)	0.978
Number of frames	900
Unit cell parameters (Å)	a = 69.35, b = 69.35, c = 212.13
Resolution range (Å)	57.79- 1.71 (1.80 - 1.71)
No. of unique reflections	27302
Multiplicity	18.4 (16.8)
R_{merge}	0.122 (2.164)
Average I/σ(I)	23.6 (1.9)
Completeness (%)	100 (100)
Wilson B (Å)	27.984
R factor (%)	17.92
Rfree (%)	22.50
r.m.s.d. bond length (Å)	0.029
r.m.s.d. bond angles (deg)	2.19

Table 4.7: Data (left) and refinement (right) statistics for imminium intermediate structure from a large single crystal of ADC, this structure was obtained at 100 K without laser initiation.

4.4.3.2 The structure of ADC in complex with NZD

Two modifications to the previous experiment were used to avoid L-aspartate preferentially binding in the active site. The first was the synthesis of a new batch of NZD with extra care taken to exclude light during the final purification step. The NZD was stored below 18 °C in an opaque vial. The second was to co-crystallise the NZD with ADC. The rationale behind this was that any residual L-aspartate present would be converted to β-alanine during the time taken for ADC to crystallise, leaving the unreactive photocage free to bind in the active site.

These modifications enabled us to obtain structures of ADC with the intact photocaged aspartate in the active site from both large single crystals and from small wedges of data merged together from multiple microcrystals.

The first structure obtained of ADC with NZD was collected from a single crystal grown at pH 3.8. The crystal was soaked, rather than co-crystallized, with the fresh batch of NZD (1 mg) added to the crystal, in a cryoprotectant mother liquor droplet, as a dry powder and incubated for 2 minutes before flash cooling to 100 K. The crystal diffracted beyond 1.4 Å on beamline I24 at Diamond Light Source. Data collection statistics and refinement details are shown in table 4.8.

In this crystal structure, shown in figure 4.20, the photocage was unexpectedly bound non-covalently in the active site. The photocaged aspartate had been designed so that the nitrobenzyl group would not interfere with the formation of a covalent bond between the L-aspartate moiety and Pyr25 and the formation of this bond was expected to occur during soaking, prior to cryocooling. However, in this structure, the NZD molecule is held non-covalently in the active by a series of hydrogen bonds. The aspartate carboxyl group adjacent to the nitrobenzyl group of NZD acts as a hydrogen bond acceptor. A hydrogen bond is formed between this carboxyl and the amino group on the side chain of Lys9. The two oxygen atoms on the nitro group

form an ion pair with Arg54. Thr57 is highlighted in the structure and may interact with the nitro groups and this residue is essential for the formation of the pyruvoyl group during post-translational activation.[185] The benzyl group is positioned in a hydrophobic pocket formed by Ile84 and Ala75. All of the labelled interacting residues shown in figure 4.20 are strictly conserved among ADCs and form stabilising interactions with the Schiff base of the natural substrate[172,166].

The non-covalently bound NZD was not observed in any other dataset. Its presence could be attributed the low pH of the crystal. The activity of ADC has been shown to drop sharply below pH 6, although it is reported to maintain more than 80% activity between pH 4 - 7. The formation of the Schiff base is dependent on the deprotonation of the L-aspartate amine group, to enable nucelophilic attack from the amine to the pyruvate carbonyl group. If the pka of the protonated amino group is ~ 10 (pka for protonated aspartic acid is 9.9) then at pH 3.8 the formation of the Schiff base is unfavourable, especially as the promoting interactions are already formed in the non-covalent structure[186]. The crystal containing the non-covalently bound substrate was cryocooled, resulting in a serendipitous cryo/pH trapped structure.

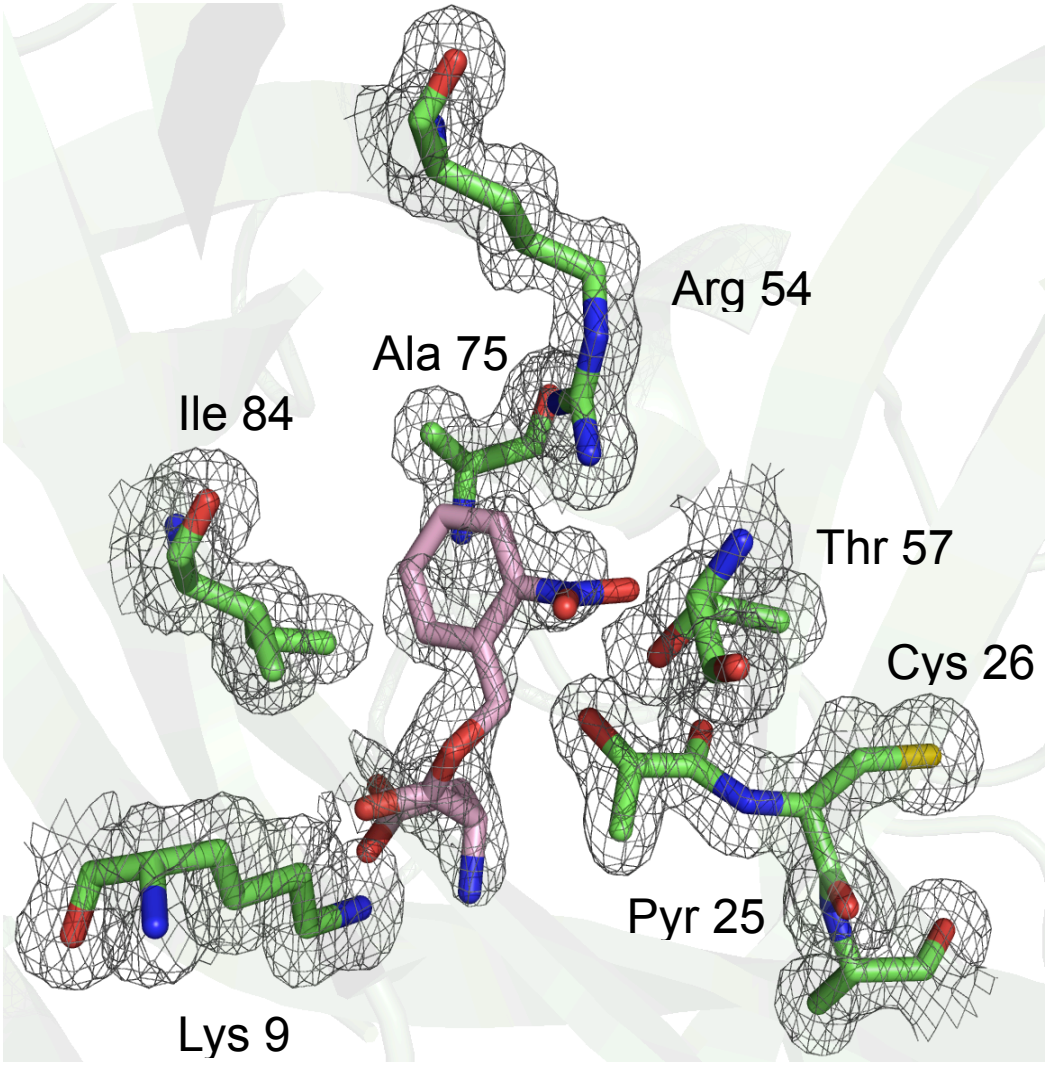

Figure 4.20: NZD structure with ADC shown in green with the photocaged L-aspartate shown in pink. The 2Fo-Fc electron density map is shown contoured at 1σ.

Dataset	NZD
Source	I24
Space group	$P6_122$
Wavelength (Å)	0.978
Number of frames	900
Unit cell parameters (Å)	a = 70.9, b = 70.9, c = 216.3
Resolution range (Å)	59.14- 1.35 (1.42 - 1.35)
No. of unique reflections	66730
Multiplicity	25.5 (6.5)
R_{merge}	0.106 (0.815)
Average I/σ(I)	23.6 (1.9)
Completeness (%)	99.7 (98.0)
Wilson B (Å)	14.23
R factor (%)	13.73
Rfree (%)	15.48
r.m.s.d bond length (Å)	0.030
r.m.s.d bond angles (deg)	2.59

Table 4.8: Data (left) and refinement (right) statistics for the ADC structure at 100 K and pH 3.8, with NZD held non-covalently in the active site.

A 'dark' dataset containing the photocaged substrate covalently bound to Pyr25 was collected from a single crystal grown in unbuffered ammonium sulphate. NZD was added to the ADC prior to crystallisation and co-crystallised in the protein active site. The crystal diffracted beyond 1.5 Å, however, the resolution of the dataset was cut to 1.7 Å during scaling to improve the overall data quality. The resolution cut-off was determined by analysis of the Pearson correlation coefficient between random half datasets ($CC_{1/2}$). $CC_{1/2}$ is

used to calculate an approximation of the true signal using the following formula:

$$CC^* = \sqrt{\frac{2CC_{1/2}}{1+CC_{1/2}}} \quad ^{187} \quad (4.1)$$

From this it is possible to estimate the correlation of the measured dataset with the true signal. At low resolution CC* is close to 1, however at high resolution this value drops sharply as the intensity of diffraction spots declines. In addition, poor batches of data were identified by analysis of Rmerge, those whose value of Rmerge exceeded 10% were excluded from data processing. The structure with NZD covalently bound to the pyruvoyl group at the N-terminal of the α-chain of ADC is shown in figure 4.21. The data collection and refinement statistics for this dataset are given in table 4.9. The covalent complex formed in this crystal due to a combination of the pH, which is closer to the biological pH in the unbuffered crystallisation solution, and the extended incubation time during co-crystallisation.

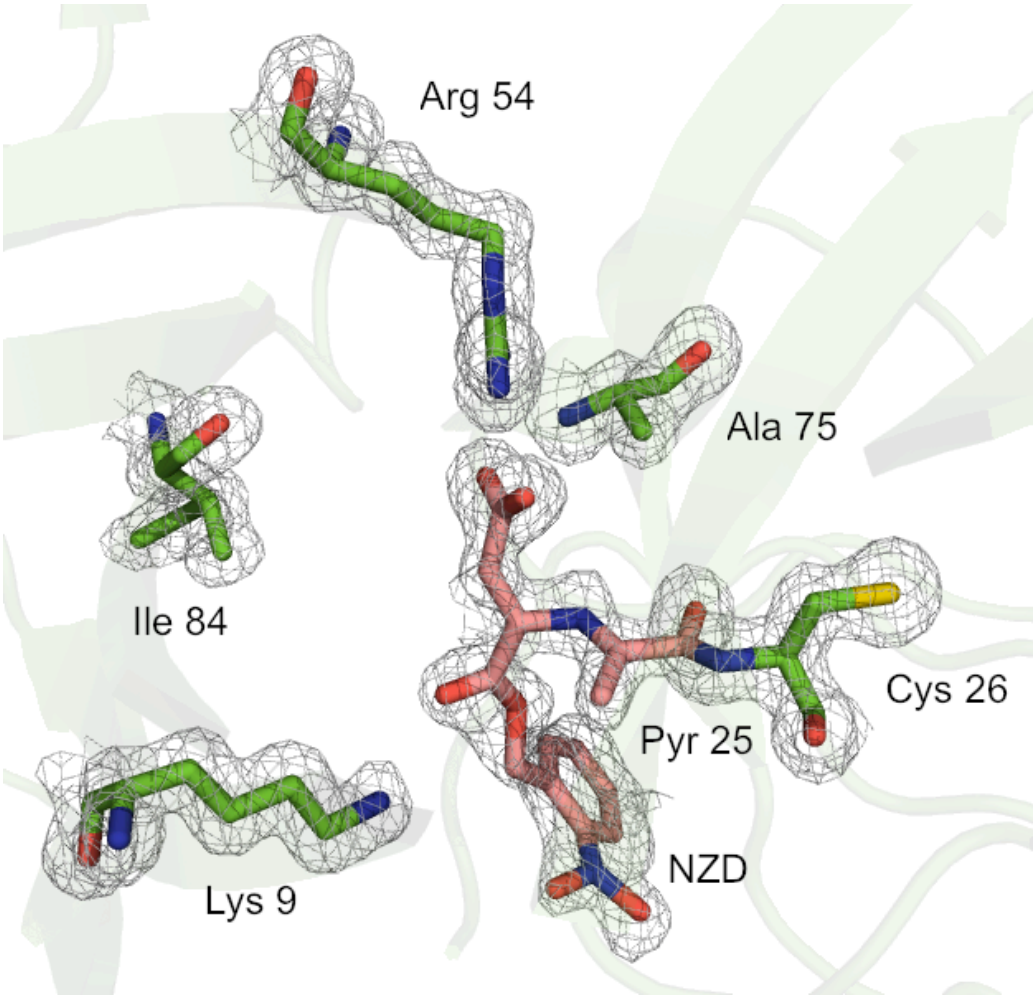

Figure 4.21: Dark ADC shown in green with the pyruvoyl residue and the photocageed L-aspartate shown in pink. The 2Fo-Fc density map is contoured at 1σ.

Dataset	Dark
Source	I24
Space group	P6122
Wavelength (Å)	0.978
Unit cell parameters (Å)	a = 71.0, b = 71.0, c = 215.9
Resolution range (Å)	47.74 – 1.70 (1.73 - 1.70)
No. of unique reflections	33743
Multiplicity	4.2 (4.2)
R_{merge}	0.066 (0.193)
Average I/σ(I)	15.9 (5.7)
Completeness (%)	98.8 (99.3)
Wilson B (Å)	11.588
R factor (%)	16.73
RFree (%)	17.69
r.m.s.d bond length Å	0.042
r.m.s.d bond angles (deg)	3.12

Table 4.9: Data collection and refinement statistics for the dark structure collected from a single crystal at 100 K.

A crystal from the same plate was exposed to blue LED light for 20 minutes, a dataset was then collected using the same strategy as for the dark dataset (dark_d2). The resolution of the dataset was cut from 1.6 to 1.75 and poorly merging batches of data were removed. The structure showed that photolysis had occurred, decaging the L-aspartate and the imminium intermediate was once again trapped in the active site upon cryocooling. The liberated o-nitrobenzaldehyde was not observed in the structure suggesting that no specific

interactions are formed between ADC and this moiety after photolysis. The ‘light’ structure is shown in figure 4.22. The data collection and refinement statistics are given in table 4.10.

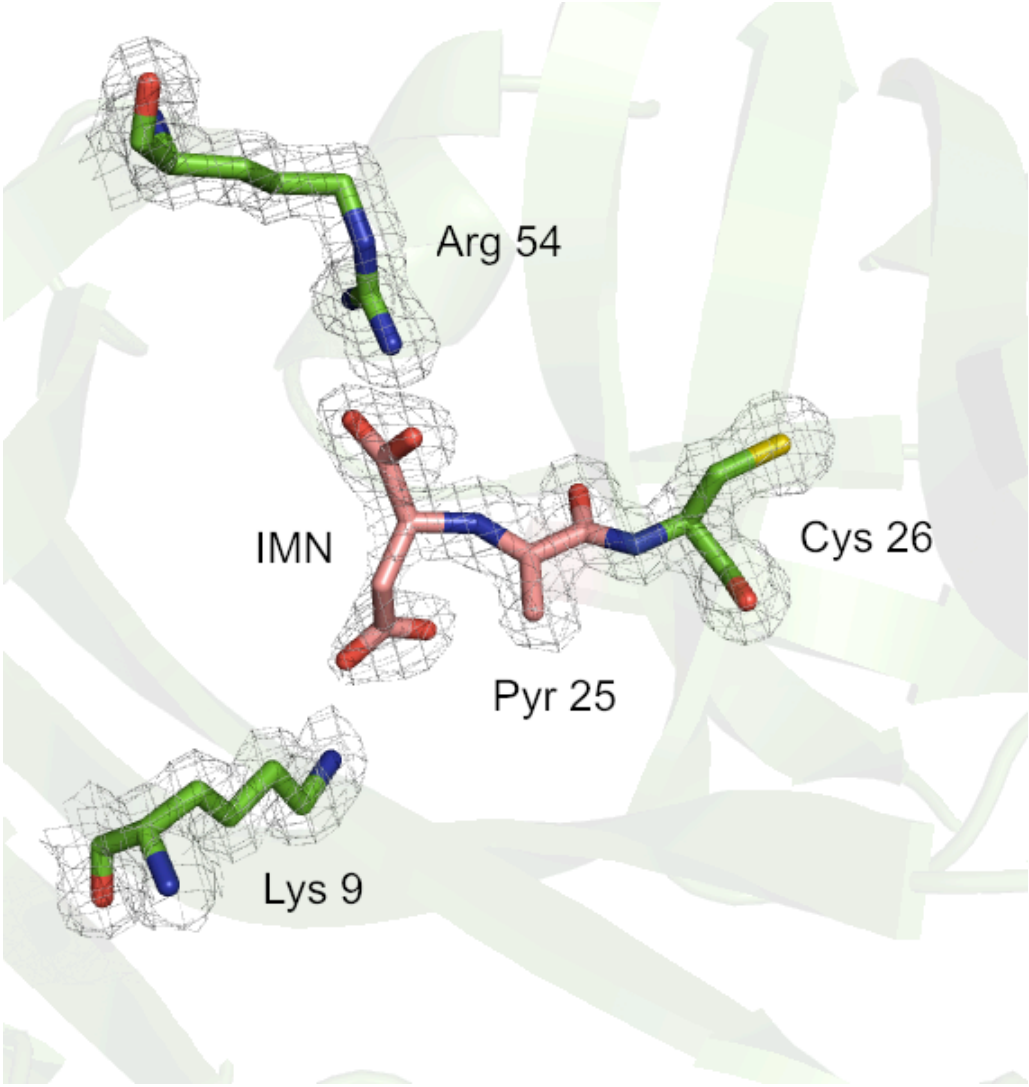

Figure 4.22: The 'light' structure showing the Schiff base (imminium) intermediate formed after photolysis of NZD. The 2Fo-Fc electron density map is contoured to 1σ.

Dataset	Light
Source	I24
Space group	$P6_122$
Wavelength (Å)	0.978
Unit cell parameters (Å)	a = 70.99, b = 70.99, c = 215.90
Resolution range (Å)	46.86 – 1.75 (1.78 - 1.75)
No. of unique reflections	31777
Multiplicity	7.1 (8.2)
R_{merge}	0.052 (0.117)
Average I/σ(I)	26.2 (15.1)
Completeness (%)	99.5 (99.6)
Wilson B (Å)	9.844
R factor (%)	20.1
RFree (%)	22.3
R.m.s.d bond length Å	0.023
R.m.s.d bond angles (deg)	3.36

Table 4.10: Data collection and refinement statistics for the light structure collected from a single crystal at 100 K.

The ‘dark’ and ‘light’ experiments were then repeated using microcrystals with the aim of showing that these structural changes were resolvable using merged datasets from many microcrystals. The resolution was set at 2.0 Å during auto-merging by ABBREVIATE, this was to account for the variations in data quality between datasets. The data and refinement statistics for the dark microcrystal structure are given in table 4.11. The ‘light’ data were very low quality and were not processed further.

Dataset	Micro_dark
Source	I24
Space group	$P6_122$
Wavelength (Å)	0.978
Number of crystals	27
Unit cell parameters (Å)	a = 71.0, b = 71.0, c = 216.6
Resolution range (Å)	54.16 – 2.0 (2.05 – 2.0)
No. of unique reflections	19376
Multiplicity	49.5 (51.4)
R_{merge}	0.117 (0.239)
Average I/σ(I)	50.1 (31.2)
Completeness (%)	100 (100)
Wilson B (Å)	11.389
R factor (%)	17.0
RFree (%)	19.7
r.m.s.d bond length Å	0.024
r.m.s.d bond angles	2.45

Table 4.11: Data collection and refinement parameters for the dark dataset collected from multiple micro crystals at 100 K.

4.4.4 Towards a time-resolved experiment

The ‘dark’ and ‘light’ structures from single crystals were used as standards from which the progress of the reaction during the time-resolved experiment could be determined. These structures along with the combination of the on-line microspectrophotometer with the sample humidifier enabled the design of a collection strategy for a time-resolved experiment at room temperature.

The initial characterisation experiments were performed at I24 using larger crystals (< 50 μm) with wedges of data over 120° of rotation collected from each crystal. These larger wedges of data were used to perform initial investigations into the progress of the reaction after exposure to the UV light source. Much of the experimental time available was used to align the sample into the light path, set up a trigger for the laser and modify the standard data collection procedure to improve the experiment timing. For example, in the standard data collection setup the crystal is photographed in 4 orientations at the start of each new data collection before the X-ray shutter is opened.

The first test was to determine the stability of the crystal at room temperature during X-ray exposure. A dataset containing 100 images was collected from a large single crystal, the crystal was oscillated over the same 0.5° portion of the crystal for each 40 ms exposure, so that the Bragg intensity for each image could be compared directly. The total Bragg intensity per image is shown in figure 4.23. The loss of half the initial diffracted intensity is widely used as an indication of substantial radiation damage[83]. From these data we determined that for a 40 ms exposure at 100% beam transmission the data quality was acceptable for the only first 10 images of the dataset.

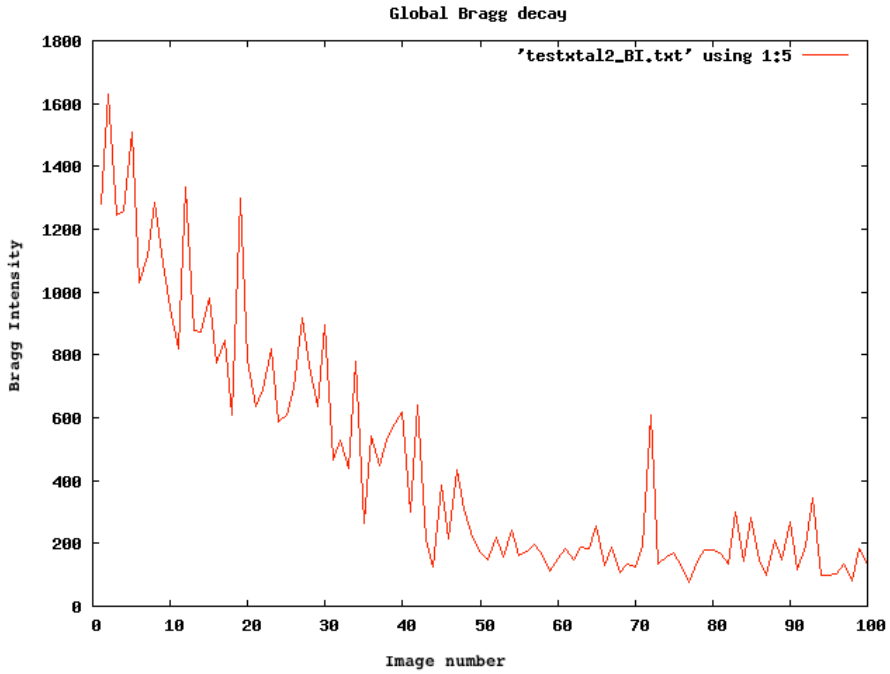

Figure 4.23: Decay in Bragg intensity as a function of image number. The traditional dose limit is defined as the dose at which the original diffraction intensity is reduced by half. For ADC crystals at room temperature the diffraction intensity was halved after 10 images when the crystals were exposed to a full beam for 40 ms per image.

Room temperature 'dark' datasets were collected from 6 microcrystals using the data collection strategy described in table 4.5. The first 10 images from each crystal were merged to form a single dataset (dark_rt_merge), from which the structure in figure 4.24 was calculated. The data and refinement statistics are given in table, 4.12 these statistics showed that the room temperature merged data was sufficient for structural determination, and that the photocage had remained intact during room temperature data collection. This was a particularly promising result because the possibility of radiation induced cleavage of the photocage from the substrate had not previously been ruled out.

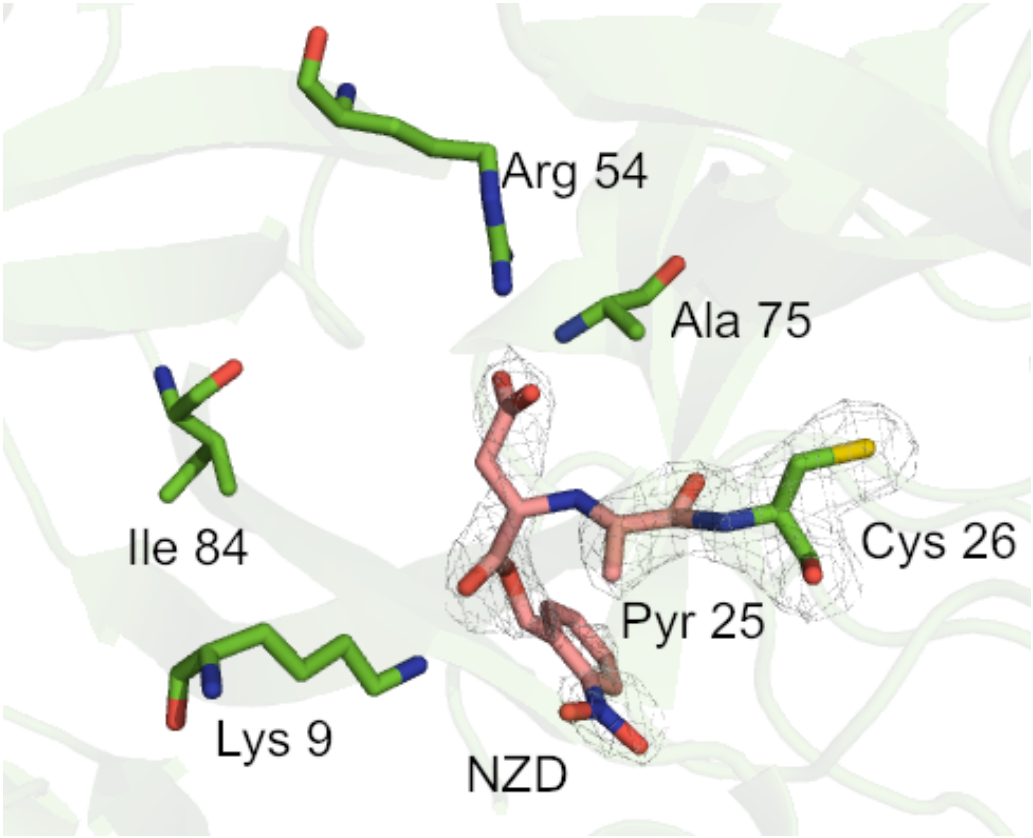

Figure 4.24: 'Dark' structure (dark_rt_merge) collected at room temperature from 6 crystals. The 2Fo-Fc electron density map is shown contoured to 1 σ.

Dataset	Dark_tr_merge
Source	I24
Space group	$P6_122$
Wavelength (Å)	0.978
Number of crystals	10
Unit cell parameters (Å)	a = 71.0, b = 71.0, c = 216.6
Resolution range (Å)	54.05 – 2.5 (2.6 – 2.5)
No. of unique reflections	121125
Multiplicity	3.9(4.1)
R_{merge}	0.106 (0.306)
Average I/σ(I)	9.2 (4.7)
Completeness (%)	99.0 (99.2)
Wilson B (Å)	30.745
R factor (%)	13.5
Rfree (%)	19.3
R.m.s.d bond length Å	0.017
R.m.s.d bond angles (deg)	1.88

Table 4.12: Data and refinement statistics for dataset dark_rt_merge

Although the resolution of this dataset was lower than those collected at 100 K the position of NZD could be identified in the electron density map. The structure was in good agreement with the covalently bound NZD dark structure, showing NZD covalently bound to Pyr 25, forming an ionic exchange interaction with Arg 54 and a hydrogen bond with Lys 9.

The photolytic uncaging of the protein was determined structurally by collecting datasets after exposure to the UV laser. Datasets were

collected from crystals exposed to the laser for 60, 120 and 200 s, using the collection strategy described in table 4.5. The data were processed according to the same method used to calculate the room temperature ‘dark’ structure. The structures are shown in figure 4.25 and the data and refinement statistics are given in table 4.13. There appears to be no significant change in the structure between the datasets 60s_light, 120s_light and 200s_light.

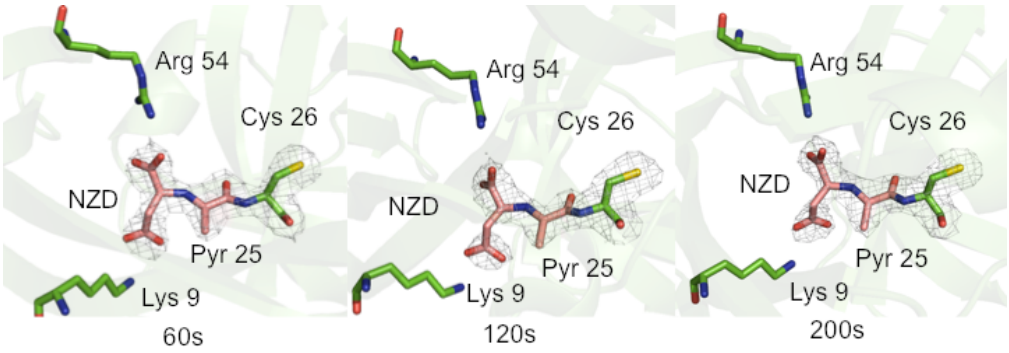

Figure 4.25: Three 'light' ADC structures after laser initiations of pulse length 60s, 120s and 200s at room temperature.

Dataset	60s_light	120s_light	200s_light
Source		I24	
Space group		$P6_122$	
Wavelength (Å)		0.978	
Number of crystals	4	5	4
Unit cell parameters (Å)	a = 71.9, b = 71.9, c = 217.9	a = 72.1, b = 72.1, c = 217.7	a = 72.1, b = 72.1, c = 217.7
Resolution range (Å)	57.27 – 2.5 (2.6 – 2.5)	54.14 – 2.5 (2.6 – 2.5)	54.16 – 2.5 (2.6 – 2.5)
No. of unique reflections	10148	10499	11983
Multiplicity	4.3 (4.7)	4.2 (4.6)	4.8 (4.9)
R_{merge}	0.153 (0.340)	0.170(0.427)	0.145 (0.388)
Average I/σ(I)	9.3 (4.8)	9.0 (4.3)	9.6 (4.6)
Completeness (%)	88.4 (88.4)	88.5 (84)	98.0 (99.0)
Wilson B (Å)	20.840	21.584	21.617
R factor (%)	16.1	15.8	16.3
Rfree (%)	21.7	19.7	21.9
r.m.s.d bond length Å	0.016	0.018	0.017
r.m.s.d bond angles (deg)	23.149	3.17	3.165

Table 4.13: Data collection and refinement statistics for the three light structures recorded at room temperature, 60s_light, 120s_light and 200s_light.

4.4.5 Laue data collection

Laue diffraction patterns from ADC crystals are shown in figure 4.26 and 4.27, the first image shows the diffraction from a single 100 ps pulse, the second shows a diffraction image from a 7-pulse frame. The data is still to be processed, however, these images show clear diffraction from 100 ps pulses. The crystals were resistant enough to radiation damage to enable full datasets to be collected and from visual inspection there are minimal overlapping reflections.

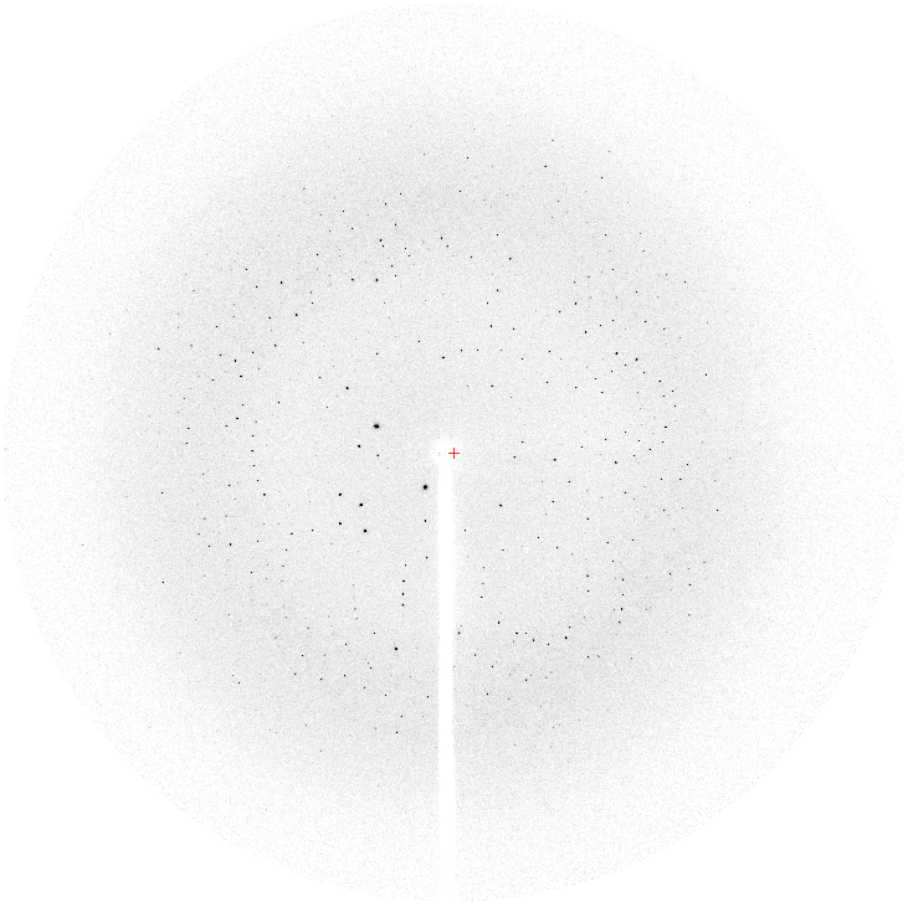

Figure 4.26: Laue diffraction from an ADC crystal at room temperature, recorded from a single 100 ps pulse.

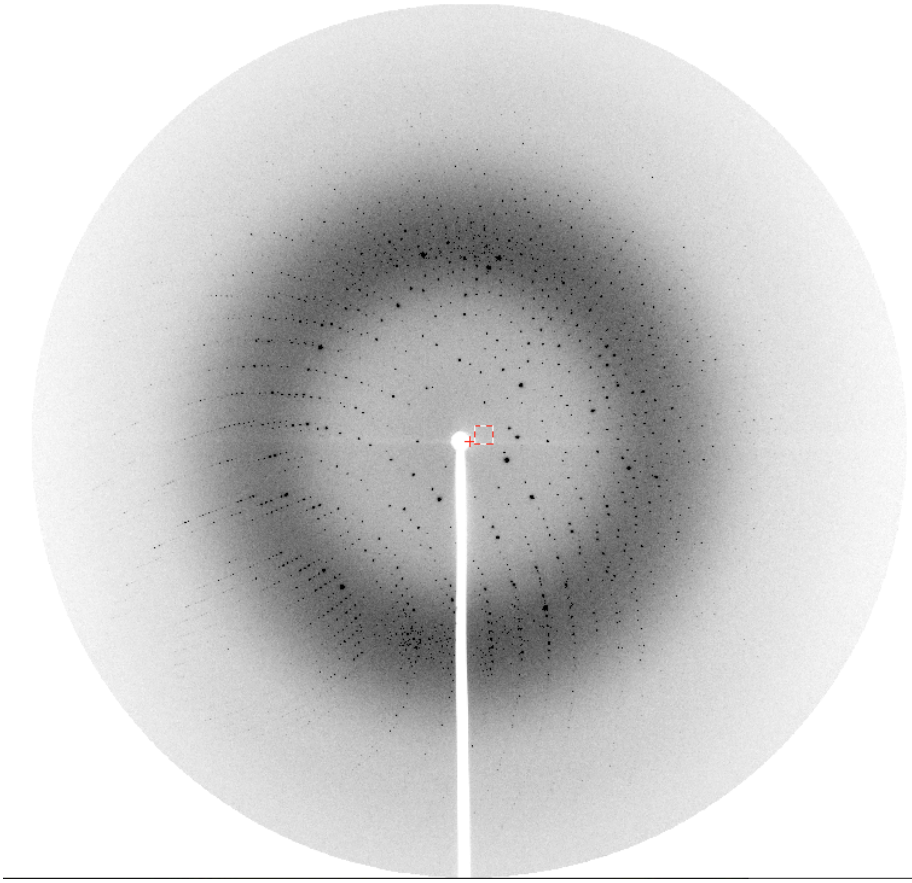

Figure 4.27: Laue diffraction from an ADC crystal at room temperature, recorded from 7 pulses of 100 ps.

4.5 Discussion

The spectroscopic characterisations carried out here suggest that for time-resolved experiments using this system the temperature must be above 185 K in order to observe any photo-induced changes in the structure. The overlap of the photocage with the protein absorbance peaks is not ideal; the absorbance of light in this region by the protein will interfere with photoinitiation. It also introduces uncertainty when following the initiation spectroscopically; ideally a photolabile group would absorb light at wavlengths longer than 300 nm[50,165]. The spectroscopic and structural data show that the photoinitiation of the reaction is slow, with a 60s laser pulse required to observe the decaging of the substrate. However, the enzymatic reaction is also very slow in the crystal. No significant changes were observed in the

crystal structure between the 60s and 200s datasets, from this we may infer that the decarboxylation of L-aspartate takes longer than 200 s in our crystal system. This is much slower than the *in vitro* the catalytic reaction which has a reported k_{cat} of 0.56 s^{-1} at 300 K[171]. It is possible that the reaction has in fact occurred more than once during the initiation time, and the resulting structure is that of a steady-state species.

Despite being unable to observe progression of the ADC reaction after photolysis the first structure of the predicted imine intermediate in the ADC enzymatic reaction has been obtained. This structure is consistent with the proposed ADC catalytic mechanism and represents the Michaelis complex of the reaction. Previous attempts to determine this structure (by cryo-trapping or trapping by reduction with borohydride) have failed (Dr M Webb, personal communication).

'Dark' structures of the ADC NZD complex at low pH, where NZD is non covalently held in the active site and at high pH where the NZD forms a covalent bond with the N-terminal pyruvoyl group on the α-chain of ADC have been obtained. These show that the photocage has not perturbed the initial stages of the catalytic cycle, as expected. Photo initiation of the ADC reaction does occur in the crystal and results in the formation of the imine intermediate which then appears stable for a prolonged period. Finally, it has been demonstrated that the multi-crystal data collection method can be used to obtain reasonable quality datasets at room temperature and 100 K.

If the ADC reaction had progressed beyond the imine intermediate we would now be in a position to perform a time-resolved experiment. We have demonstrated that we can achieve a time-resolution of 40 ms for the X-ray data collection. The photo initiation of the reaction limits the resolution of the experiment, however, this could be improved by using a more intense laser. Trying to improve the time resolution of the experiment may seem redundant when considering that no structural changes are observed within 140 s after initation, however, the first

step in the mechanism is rate limiting and we aim to observe the structure of β-alanine in complex with ADC.

During this study I identified a new way to improve this experiment and the time-resolution available at a monochromatic synchrotron sources. The new multiplexing technique is described in the following chapter.

Chapter 5 HATRX: A new approach to time-resolved X-ray crystallography

5.1 Introduction

To understand the dynamic properties of chemical and biological processes the time-resolution of the experiments used must correspond to the time scales of the mechanisms involved. The limits on the time resolution of crystallographic experiments is discussed in section 1.1. Since FEL and Laue facilities are in limited supply, we have developed a time-resolved method that can be performed at standard monochromatic beamlines (or for slow reactions, at home sources). The sensitivity of any multicrystal approach (chapter 5) is limited by the length of time required to collect a diffraction image (which is inherently limited by the flux of the beam) and the number of crystals needed to produce a full dataset.

To improve both the time-resolution and the sample consumption of the multi-crystal experiments, we have developed a novel multiplexing technique. This method utilises the Hadamard transform to design multiplexed collection strategies, where multiple time points are recorded from each crystal in a single run of the experiment. Although the Hadamard transform is already used in mass spectrometry[188–190] and NMR spectroscopy[191,192] to improve the signal-to-noise ratio of data, it has never been applied to time-resolved experiments.

5.1.1 Basic theory of the Hadamard transform

The Hadamard method of multiplexing measurements is most easily explained using the analogy of measuring the mass of three objects using a scale that introduces an error (or uncertainty) onto the recorded measurement. If the three objects are weighed individually there is an uncertainty introduced during each measurement. When all three objects have the same mass, they can be weighed together and divided by three, this will improve the accuracy of the measurement by a factor of $\sqrt{n}$. A greater signal to noise advantage can be obtained if the objects are weighed in groups according to a Hadamard **S**-matrix, this method can also be used to determine the individual mass of each

object if they do not all weigh the same amount[190,193]. An outline of the method is given in figure 5.1.

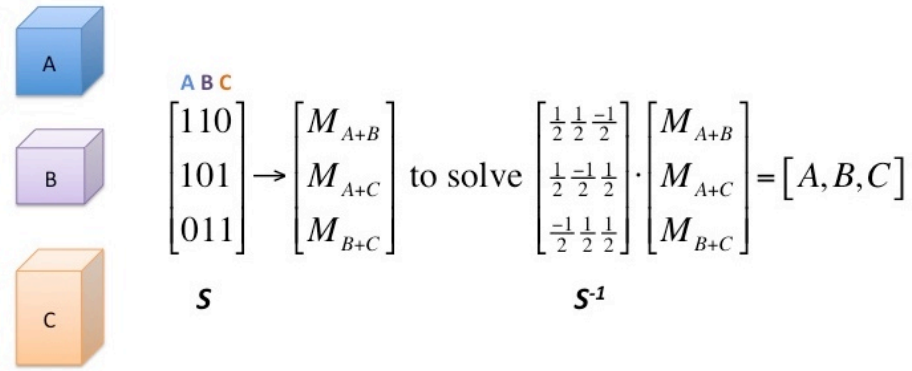

Figure 5.1: Schematic of the Hadamard weighing experiment, objects A, B and C are weighed in groups according to the S-matrix. The masses are recorded in a column vector which is then multiplied by the inverse of the S-matrix, S^{-1} to yield a vector containing the masses of objects A, B and C. This method produces a S/N ratio of (n+1)2/4n ≈ n/4 for n measurments vs. √n for the conventional method of measuring.

This technique can be applied to time-resolved crystallography by encoding the X-ray beam with a sequence of on-off pulses; determined by the **S**-matrix. The diffraction at a series of time-points is then measured as a single diffraction image. The intensities from this image are mathematically transformed to give the individual intensities for each reflection at single time-points along the reaction pathway; a schematic of this experiment is shown in figure 5.2.

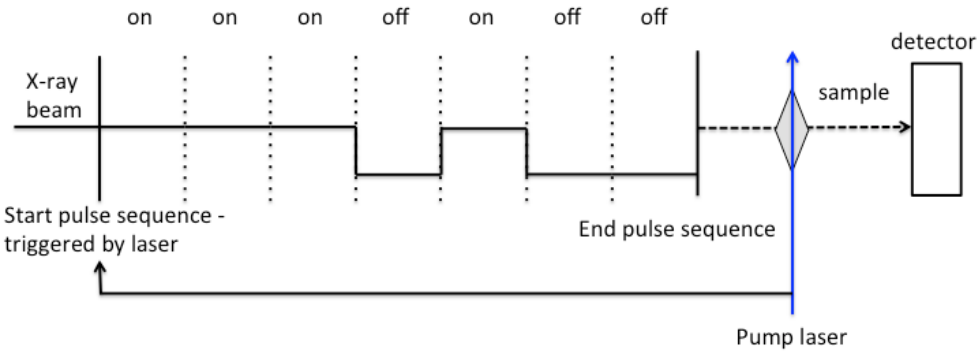

Figure 5.2: Schematic showing the Hadamard transform method applied to time-resolved X-ray crystallography (HATRX) by encoding the X-ray beam with a pulse sequence. The detector records the diffraction from the whole sequence as a single image.

5.2 Contributions to this chapter

The original suggestion of applying Hadamard transforms to time-resolved experiments was made by Prof. G.S. Beddard. I proposed the use of this method for time-resolved X-ray crystallography and demonstrated its application. Dr R.L. Owen and Prof. A.R. Pearson assisted with data collection and processing.

This work has been accepted for publication in Nature Methods.

Yorke, B.A, Beddard, G.S., Owen, R.L., Pearson, A.R. (2014) A new approach to time-resolved X-ray crystallography: removing flux limitations using the Hadamard Transform. *Nature Methods. In press.*

5.3 The HATRX method

In a Hadamard time-resolved crystallography (HATRX) experiment experiment, a Hadamard ***S***-matrix (Figure 5.1) is used to design a collection strategy in which multiple time points are collected from a single crystal. Each row of the matrix determines the time points at which diffraction patterns are recorded onto the detector during each run of the experiment (probe sequence). Only after the full probe sequence has been recorded is the detector read out and the sample changed for the next run of the experiment. This removes the requirement that a single probe pulse deliver sufficient photons to produce a measurable diffraction pattern, as long as there are enough photons in the entire sequence of pulses. The number of photons within the entire probe sequence therefore defines the sensitivity of the experiment; with the time resolution defined as the total probe sequence length divided by the number of pulses. This is in contrast to a traditional pump-probe experiment where the diffraction pattern from a single time point is recorded during each run of the experiment (Figure 5.3).

The experiment is conducted as follows; the reaction is initiated, for example by a laser pulse, and the entire probe sequence (given by the first row of the ***S*** matrix) is recorded by the detector as a single image. This is repeated on a new sample (or if the system is state-reversible on the same sample after relaxation), but with the probe sequence now defined by the next row of the ***S*** matrix, until all rows have been used. The resulting encoded signals, from n excitations are collated to form a vector $\boldsymbol{w}$ of length n. To obtain the time-dependent signal, $\boldsymbol{I}_t$, the probe sequence encoding is reversed by multiplying the vector $\boldsymbol{w}$ by the inverse of the matrix $\boldsymbol{S}$. *i.e.* $\boldsymbol{I}_t = \boldsymbol{S}^{-1}\boldsymbol{w}$.

Since the use of the Hadamard approach is independent of the manner in which the pulse sequence is generated, a HATRX experiment can be reproduced by selectively summing single images from a continuous series of evenly spaced exposures into

HATRX images. This allows us to directly compare the electron density acquired from the HATRX time-series to that from a control time-series acquired in the conventional manner, and demonstrates that a HATRX experiment can successfully track time-dependent structural changes (Figure 5.6).

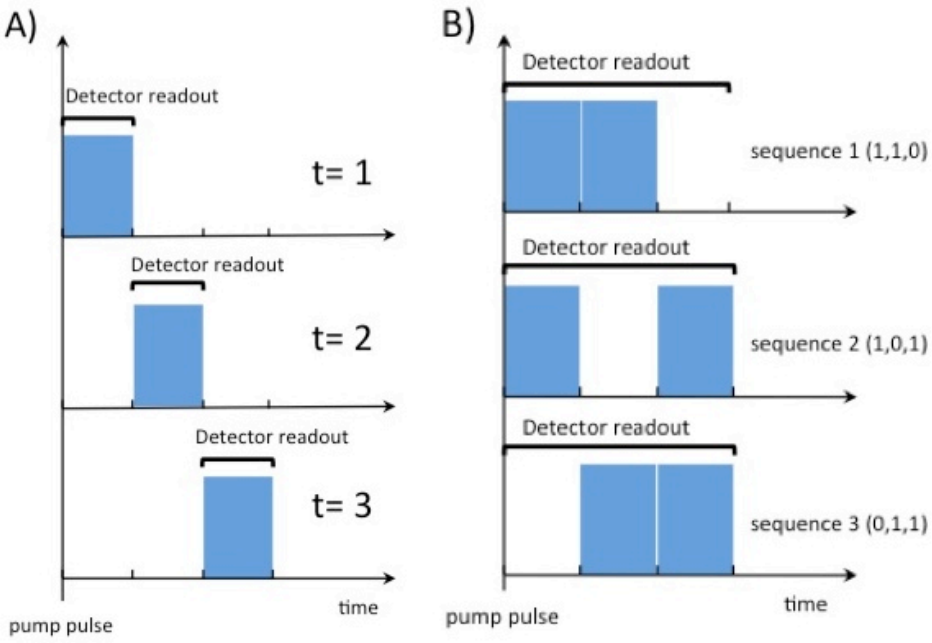

Figure 5.3: Comparison of the traditional pump probe experiment (A) and the Hadamard experiment (B)

It should be noted that although in this chapter the application of the Hadamard transform to time-resolved crystallography is discussed, in practice the underlying methodology can be applied to any time-resolved experiment where the probe can be encoded.

5.4 Materials and Methods

5.4.1 Calculation of *S*-matrices

Left circulant ***S***-matrices were calculated using Maple according to the method described by Harwit and Sloane[190] (Figure 5.4). First, all possible values of n were identified, where n is a prime number obeying the condition $n = 4m + 3$, where m is any integer greater or equal to 0. These n values determine the allowed ***S***-matrix dimensions.

Next, a vector (***v1***) is defined where each element is the square of its index. A new vector (***v2***) is calculated as the modulo remainder of the corresponding element of ***v1*** divided by n, ((*j* mod *n*)+1). The first row of the ***S***-matrix is defined as a vector of length n, with the first element defined as 1. The remaining elements are then assigned as 1 if the value of its index is present anywhere in ***v2***, if not it is assigned as 0. The first row is then rotated by 1 position to the left to produce the second row, this is repeated n times to produce a square n × n ***S***-matrix.

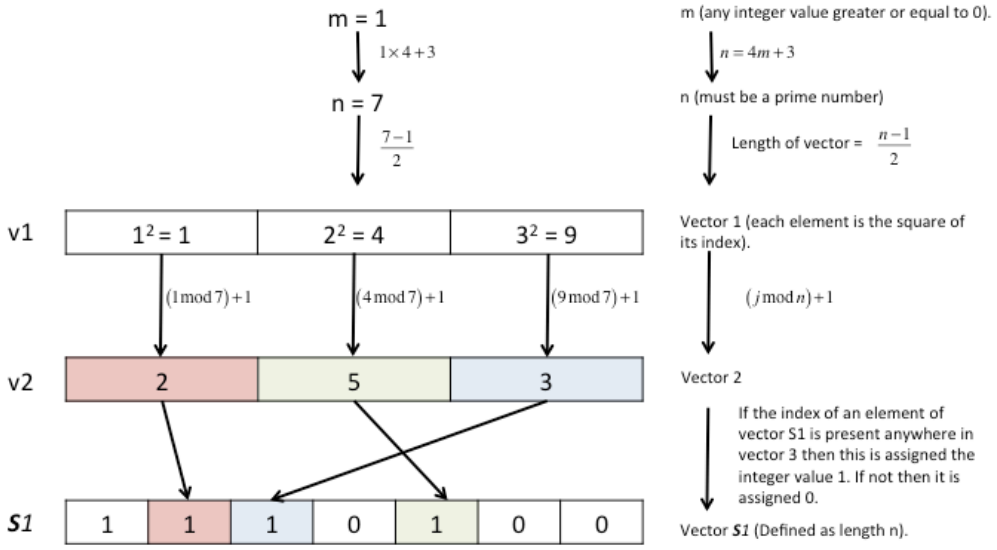

Figure 5.4: Flow chart showing the calculation of the first row of a 7 × 7 *S*-matrix.

The first three values of n are 3, 7 and 11, pictoral represenations of these ***S***-matrices are shown in Figure 5.5.

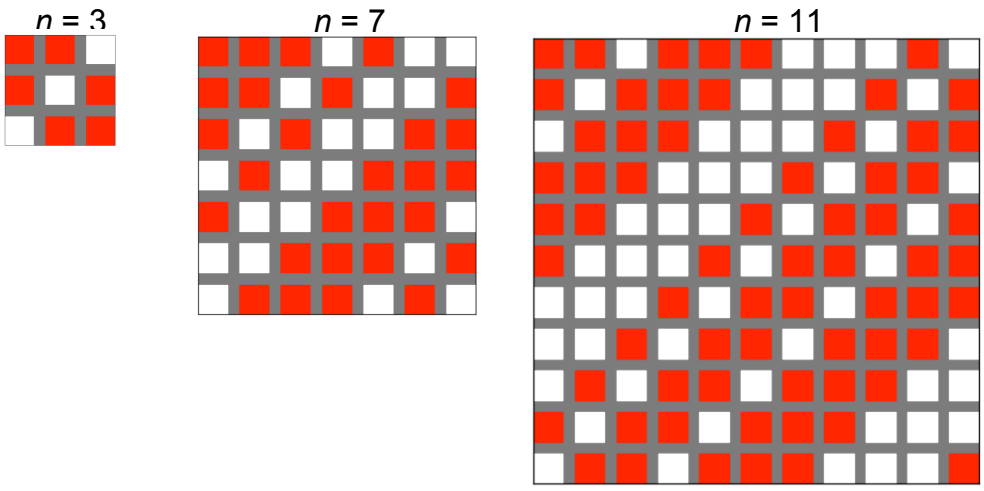

Figure 5.5 Pictorial representation of three *S* matrices. The red squares represent ones, the white squares, zeros.

The inverse of the ***S***-matrix, $\boldsymbol{S^{-1}}$, was calculated using the following formula:

$$\boldsymbol{S}^{-1} = \frac{2}{n+1}(2\boldsymbol{S}^{T} - \boldsymbol{J}) \qquad (5.1)$$

Where ***J*** is the 'all ones' matrix, however, it can also be calculated by direct inversion[155,190].

5.4.2 Data Collection

Thaumatin crystals were provided by Robin Owen (DLS), these we)e prepared using the following method. The protein in ddH20 (40 mg/ml] was crystallised in a 2:1 (4 ml protein: 2 ml reservoir solution) mixture with 0.05 M ADA pH 6.8, 0.6 M K/Na Tartrate and 20% glycerol in sitting drop plates. The thaumatin crystals (~10-20 mm along the longest edge) were then mounted in a nylon loop and cryo-cooled to 100 K in liquid nitrogen. All diffraction data were collected on beamline I24 (DLS) at 100 K, with a beam size of 10 x 10 mm^2 and an incident flux of $1.5x10^{12}$ ph s^{-1} in the focal spot.

To design the data collection strategy a number of tests were carried out to determine the absorbed dose required to break the disulfide bonds, to ensure that the disulphide bonds were still intact after the first few images so that a change in structure can be followed across

the dataset and to confirm that all data collected was useful, *i.e*. the intensity of diffraction was strong enough by the end of the data set to be able to determine the crystal structure and that there was no significant change in the unit cell parameters of the crystal over the data collection. An initial burn test was carried out to provide a starting estimate of the dose required to cause structural changes in the crystal. For this, 100 images were collected from a single crystal using a 200 ms exposure, the oscillation per image was 0.001° this meant that only 1 degree was covered over the whole dataset and so the Bragg intensity was comparable over all images. The intensity of all of the reflections was then calculated for each image using LABELIT[153]. After 60 images the diffracting power of the crystal had halved and so a change in the structure should be apparent within 10% of this value (3×10^{10} photons).

Any changes in the unit cell were identified preliminarily by visual analysis of the spot sizes and shapes across this data set. To verify the stability of the unit cell parameters a dataset of 28 images was collected with a 200 ms exposure and 0.2° oscillation per image, these images were grouped into 4 bins of 7 and the unit cell parameters were calculated using XDS. Finally, to determine the dose required to observe the breaking of disulfides in the crystal, a dataset containing 1400 images was collected with the beam attenuated to 20% transmission and an exposure time of 100 ms over 0.12° of oscillation per image. The crystal structure was then solved using batches of 200 images through the dataset and the position of disulfide cysteines was compared.

To simulate the HATRX experiment wedges of data were collected from 264 microcrystals in random orientations. Each wedge contained 27 images taken from the same repeated oscillation of 1°, each image had an exposure time of 20 ms, the absorbed dose per image was 1.16 MGy and the total absorbed dose was 29.16 MGy over the 27 images.

5.4.3 Data Processing

A subset of 31 crystals were used to collect control data, the diffraction data were integrated using XDS[174] and then merged into a single mtz file with POINTLESS[175]. Data from all image 1 were then scaled together using AIMLESS to produce a dataset for time (dose) point 1. This was repeated for each batch to form 27 time-resolved datasets, shown in table 5.1.

Image	Crystal	time point
1	1 2 3 4 ⋯ 31	1
2	1 2 3 4 ⋯ 31	2
⋮	⋮	⋮
⋮	⋮	⋮
27	1 2 3 4 ⋯ 31	27

Table 5.1: The data structure of the control dataset used to produce time-resolved electron density maps.

The HATRX experiment was simulated using a 3×3 ***S***-matrix but to extend the time (dose) range probed, the experiment was repeated 9 times over the 27 images. The data wedges from the remaining 233 crystals were split into three approximately equal groups of about 70 images. An exposure sequence corresponding to a line of the 3×3 ***S*** matrix was assigned to each group, to determine which images would be summed for the HATRX analysis. The required images were then summed using the programme SUMSUB provided by David Waterman (CCP4)[194] to yield a new HATRX encoded image.

§	Crystal group 1	Crystal group 2	Crystal group 3	HATRX group
1	1	1	0	
2	1	0	1	1
3	0	1	1	
4	1	1	0	
5	1	0	1	2
6	0	1	1	
⋮	⋮	⋮	⋮	.
25	1	1	0	
26	1	0	1	9
27	0	1	1	

Table 5.2: Schematic showing how images were summed to create the HATRX images. 1 indicates the image was included in the summed image, 0 that it was not included. Each HATRX group contains three summed images.

The HATRX encoded images were indexed and integrated using XDS, the integrated images were then scaled with AIMLESS[195]. Poorly merging datasets were identified by analysis of Rmerge vs. Batch and removed before rescaling. Once a scaled the intensities were converted into structure factors using cTRUNCATE[175]. A dummy .mtz file containing all possible reflections was created using CAD[196], the F and SigF columns from each image in the HATRX group were copied into this file. To produce a file with the following headings: H, K, L, F1, SigF1, F2, SigF2, F3, SigF3 for all reflections. This was converted to .cif format (standard text), the column headings all rows containing a reflection with a structure factor of zero were removed. The three HATRX structure factors for each reflection were then read into R[197] as a numerical vector ($w_{1\text{-}3}$). This vector was then multiplied by the inverse of the ***S***-matrix ($\boldsymbol{S}^{-1}$) and the three resulting structure factor values for each time (dose) point were written to a plain text file.

$$\boldsymbol{S}^{-1}\begin{bmatrix} w_1 \\ \vdots \\ w_n \end{bmatrix} = \begin{bmatrix} I_1 \\ \vdots \\ I_n \end{bmatrix} \qquad (5.2)$$

The time (dose)-resolved structure factors were calculated for each reflection and the time-resolved SigF values were calculated in the same way. The data was converted to .mtz format for map calculation and analysis. Phases were calculated using 1KWN as a starting model. The model was refined using REFMAC5[178] against the HATRX time-point 1 data and the resulting phases used for all further map calculations (Table 5.4). Maps derived from the control and HATRX data were then compared by the calculation of difference maps.

i.e. $F_{HATRX_1} - F_{TRAD_1}$ for $1 \le n \le N$; $\left(F_{HATRX_N} - F_{HATRX_1}\right)$ vs. $\left(F_{TRAD_N} - F_{TRAD_1}\right)$ (5.3)

This process was carried out for all nine HATRX groups, resulting in 27 time-resolved datasets. The HATRX method was also tested using a

7×7 ***S*** matrix, however, the data were insufficiently complete to calculate a map (<60 %).

The control and HATRX data were compared by analysis of $F_{HATRX} - F_{control}$ maps, the weighted R-factor (W_{rel}) between the reference data (R) and the HATRX data (H) at each time-point were calculated for each resolution shell using REFMAC5[178]:

$$W_{rel} = \frac{\sum \frac{\left|f_R^2 - f_M^2\right|}{\sigma_R^2} + \frac{\left|f_H^2 - f_M^2\right|}{\sigma_H^2}}{\sum \left(\frac{f_R}{\sigma_R}\right)^2 + \left(\frac{f_H}{\sigma_H}\right)^2} \quad (5.4)$$

where

$$f_M^2 = \left[\left(\frac{f_R}{\sigma_R}\right)^2 + \left(\frac{f_H}{\sigma_H}\right)^2\right] / \left(\frac{1}{\sigma_R^2} + \frac{1}{\sigma_H^2}\right), \ \sigma_R = 2 f_R \sigma_{f_R} \text{ and } \sigma_H = 2 f_H \sigma_{f_H} \quad (5.5)$$

5.5 Results

Both the control and HATRX datasets were scaled using AIMLESS, the scaling statistics for time (dose)-points 1, 15 and 27 from the control data and the HATRX data for the HATRX group 1 summed according to the three sequences ([110], [101], and [011]) are shown in tables 5.4 and 5.3 (these tables are provided in full in the Appendix). A direct comparison cannot be made between the scaling statistics of the control and HATRX groups as an analysis of consistency. However, the statistics for both groups show that merging wedges of data from multiple crystals can provide satisfactory data with correlation coefficients ($CC_{1/2}$) > 98% for both types of data. The R_{merge} and I/Sig(I) values are also indicative of good quality data. Although the HATRX data has slightly worse values for these metrics as it is multiplexed, this does not affect the quality of the data post transformation or the electron density maps.

Time point	1	15	27
Resolution (Å)	45.8 – 1.8 (1.84 – 1.80)		
Unit cell	*a*=57.9 Å, *b*=57.9 Å, *c*=150.2 Å, α=90°, β=90°, γ=90°		
R_{merge} (%)	6.7 (8.7)	6.2 (9.0)	6.3 (9.7)
$R_{p.i.m.}$ (%)	5.3 (7.1)	4.9 (7.3)	5.0 (7.7)
# reflections	37901 (2053)	37192 (1866)	38746 (1877)
#unique reflections	20148 (1120)	20134 (1053)	20418 (1031)
<I>/sd<I>	29.8 (27.7)	34.6 (21.9)	26.5 (19.1)
CC(1/2)	0.982 (0.975)	0.988 (0.971)	0.988 (0.974)
Completeness (%)	83.2 (79.9)	82.7 (74.3)	83.7 (72.8)
Multiplicity	1.9 (1.8)	1.8 (1.8)	1.9 (1.8)
Absorbed Dose (MGy)	1.08	16.20	29.16

Table 5.3: Data statistics of time-points 1, 15 and 27 from the control dataset.

Image	1 [110]	1 [101]	1 [011]
Resolution (Å)	57.8-1.79 (1.83-1.79)		
Unit cell	*a*=57.8 Å, *b*=57.8 Å, *c*=149.9 Å, α=90°, β=90°, γ=90°		
R_{merge} (%)	10.7 (13.9)	10.6 (15.6)	10.2 (13.9)
$R_{p.i.m.}$ (%)	5.9 (7.8)	6.0 (8.8)	5.8 (8.1)
#reflections	88218 (3731)	87000 (4212)	83487 (3901)
#unique reflections	23468 (1061)	23569 (1196)	23528 (1184)
<I>/sd<I>	19.6 (10.9)	15.6 (11.2)	16.0 (11.3)
CC(1/2)	0.984 (0.962)	0.986 (0.955)	0.987 (0.963)
Completeness (%)	95.3 (74.4)	96.4 (85.0)	96.0 (83.9)
Multiplicity	3.8 (3.5)	3.7 (3.5)	3.5 (3.3)
Absorbed Dose (MGy)	3.24	3.24	3.24

Table 5.4: Data and refinement statistics for HATRX group 1.

To analyse the agreement between the data from both methods, a comparison was made between the electron density maps calculated using traditional data processing (control) and the HATRX method. Ideally the $F_{HATRX} - F_{control}$ maps would be completely flat, showing that the HATRX method can reliably reproduce the classical data. The control and HATRX data were collected using the same methodology and only the data processing in the proof of principle experiments was distinct. The comparison of the control and HATRX data showed no significant difference between the two datasets and the maps contoured at 3 rmsd showed no significant features (Figure 5.6). Table 5.5 shows the weighted R-factors between HATRX and control data for

one time (dose)-point from each HATRX group: 1, 4, 7, 10, 13, 16, 19, 22, and 25. The complete table is in the appendix.

Resolution (Å)	W_{rel}1	W_{rel} 4	W_{rel} 7	W_{rel} 10	W_{rel} 13	W_{rel} 16	W_{rel} 19	W_{rel} 22	W_{rel} 25
11.20	0.020	0.006	0.007	0.017	0.205	0.036	0.025	0.002	0.007
6.60	0.009	0.008	0.023	0.000	0.014	0.009	0.023	0.000	0.014
5.10	0.028	0.001	0.003	0.000	0.002	0.003	0.002	0.002	0.004
4.30	0.025	0.001	0.013	0.019	0.005	0.009	0.003	0.005	0.015
3.78	0.008	0.006	0.005	0.003	0.004	0.000	0.004	0.001	0.010
3.41	0.020	0.000	0.001	0.016	0.009	0.005	0.001	0.004	0.006
3.15	0.002	0.000	0.011	0.005	0.000	0.002	0.009	0.000	0.008
2.92	0.015	0.008	0.001	0.004	0.009	0.000	0.001	0.001	0.003
2.75	0.007	0.011	0.006	0.000	0.001	0.003	0.003	0.000	0.000
2.60	0.001	0.004	0.089	0.002	0.003	0.010	0.000	0.000	0.003
2.47	0.000	0.000	0.006	0.004	0.005	0.003	0.003	0.016	0.003
2.36	0.009	0.043	0.000	0.001	0.002	0.013	0.000	0.003	0.017
2.26	0.005	0.002	0.001	0.022	0.000	0.011	0.002	0.000	0.013
2.18	0.017	0.000	0.000	0.006	0.007	0.004	0.002	0.001	0.000
2.10	0.000	0.001	0.000	0.001	0.009	0.013	0.002	0.005	0.002
2.04	0.005	0.002	0.004	0.005	0.007	0.008	0.001	0.028	0.001
1.97	0.000	0.000	0.002	0.014	0.000	0.000	0.009	0.001	0.000
1.91	0.004	0.000	0.000	0.001	0.002	0.017	0.000	0.001	0.002
1.86	0.000	0.009	0.001	0.001	0.002	0.003	0.005	0.001	0.000
1.81	0.001	0.001	0.008	0.010	0.002	0.002	0.030	0.000	0.012

Table 5.5: Weighted R-factors calculated between the HATRX and control datasets for one time(dose)-point from the HATRX groups 1, 4, 7, 10, 13, 16, 19, 22, 25.

W_{rel} does not exceed 5%, except in the inner resolution shell of time-point 13, this is an anomaly and does not significantly affect the overall agreement between the datasets. The average W_{rel} for all resolution shells does not exceed 2% for any of the time-points. The agreement between datasets displays that the HATRX method can be reliably used to calculate electron density maps from data merged from

multiple crystals and that no artefacts are introduced as a result of using this method.

The structural changes in Thaumatin due to radiation damage are evident through the breaking of disulphide bonds. In these experiments the exposure time and incident flux were sufficient to ensure that significant damage occurred within the crystal and the dose limit was reached by the end of the experiment. To identify the structural changes, difference maps $F_{t=n} - F_{t=1}$ were calculated, where the zero dose map was calculated using the first dose-point. These maps show clear and significant changes in the electron density around disulphide bonds with the increase in dose with agreement between the control and HATRX data. The changes in electron density at disulphide bonds between Cys56 - Cys66 and Cys71 – Cys77 are shown in figure 5.6 for time (dose)-points 2, 4, 7, 10, 13, 16, 19, 22, and 25. These results show that the HATRX method can be used to produce 4D electron density maps that are simultaneously highly resolved in space and time.

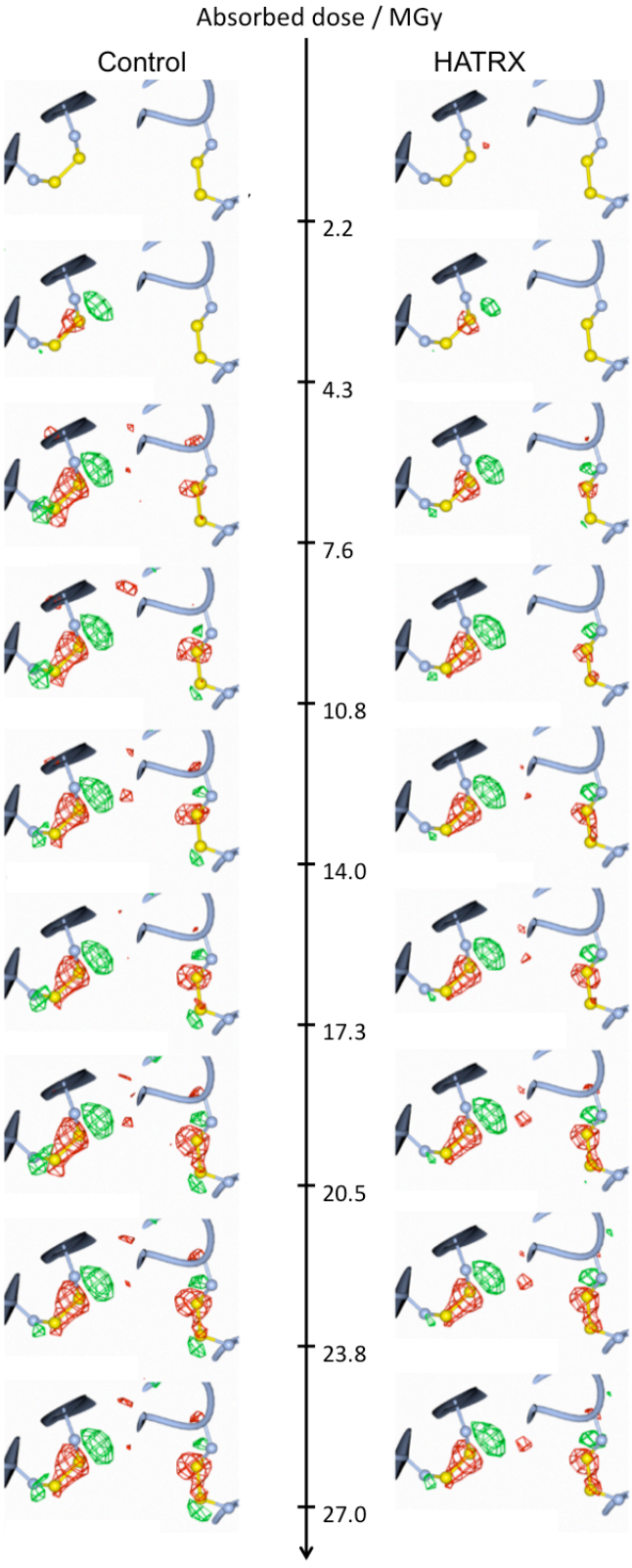

Figure 5.6: Difference electron density maps calculated as F_n-F_1 (where *n*=2,4,7,10,13,16,19,22,25) for the control data (left) and the HATRX data (right). The maps are contoured at 3 r.m.s.d. Negative difference density is coloured red and positive difference density is coloured green. Two of thaumatin's disulphide bonds are shown for each time-point.

5.6 Discussion

The aim of these experiments was to show that the HATRX method can be used to enhance time-resolved X-ray crystallographic experiments. It was not possible in this thesis to test the proposed improvement of time-resolution, due to the requirement of the installation of a rotating shutter or chopper at the beamline, to encode the X-ray beam with the ***S***-matrix probe sequence. An alternate possibility to encode the HATRX sequence is to electronically gate the detector to record data according to the probe sequence and this has been recently demonstrated by a collaborating team at Diamond Light Source[198].

The proof of principle experiments are thus not truly time-resolved, however, the changes in structure occur as the absorbed dose increases (where the absorbed dose increases with time). Therefore, dose can be used as a proxy for time, allowing us to use a system whose mechanisms are well characterised, in this case the radiation damage of Thaumatin to demonstrate the HATRX method. Another benefit of using dose as a proxy for time was that the initiation of structural changes (the pump) was consistent across all molecules in the X-ray beam. There were no issues with timing the pump and probe, or light absorption in the crystal causing inconsistent laser initiation across the crystal. All of these issues can be resolved by full characterisation of a light activated system and in future experiments a photocaged ADC, created using the methodology based on that in the previous chapter will be used to demonstrate the HATRX method in a truly time-resolved experiment.

The real advantage of this method is that it can free the achievable time-resolution from its current total dependence on source brilliance, and thus available photons, by summing time-points across a probe sequence. This results in an improved signal to

noise ratio, because of the increased number of photons recorded during each measurement.

A comparison of the expected signal can be made using estimates of the known flux from a monochromatic X-ray beamline. For example, beamline I24 at Diamond Light Source delivers $\approx 10^{12}$ photons s^{-1}. Assuming an elastic scattering efficiency of 0.1%,[199] for an image with 100 spots there are 10^7 photons scattered/spot/s (assuming for illustration that spots are of equal intensity). If we record 100 time points over a 100 μs range then with classical pump-probe if each time point is 1 μs in duration then each spot will contain only 10 photons. In contrast, by using the HATRX approach each spot will contain approximately 500 photons, because the HATRX sequence is approximately half on and half off (Figure 5.5).

There are two contributions to the improvement in signal to noise. The first is in the absolute number of photons recorded for each time point. Consider the simplest $n = 3$ experiment. In the classical pump-probe approach, each time-dependent measurement is made once. However, with the HATRX approach, the encoded measurement is repeated 3 times with each time point measured twice in the entire experiment, resulting in a doubling of the signal recorded. Consequently, the mean square error associated with the measurement is reduced by a factor $(n+1)^2/4n \approx n/4$ which means that the signal-to-noise ratio is increased by a factor of $(n+1)/2\sqrt{n} \approx \sqrt{n}/2$ relative to conventional experiments[190].

Although here we use a sequence of probe pulses that are equally separated in time, the method will work equally well if the probe pulses are, for example, logarithmically separated in time, thus allowing a wide range of time scales to be observed in a single set of experiments. This is because the experiment measures the total intensity from a sequence and is independent of the time-stamp associated with each pulse.

An additional advantage of HATRX, specific to a crystallographic experiment, is that the scaling together of data from multiple crystals and time-points need only be done once (as the same sample population progresses in time). In contrast in a serial crystallography pump-probe diffraction experiment the data must be scaled first for each time-point over all crystal orientations and then again over time. This is a non-trivial task and is one of the major sources of error in current time-resolved crystallography where multiple crystals are used.

Experimentally, generating Hadamard probe sequences in an X-ray diffraction experiment could be achieved in a number of ways, for example, through the use of a rotating disc shutter encoded with a sequence, which is relatively simple, or by deflecting electron bunches out of the synchrotron electron beam[200] which is also technically feasible. An alternative and more widely implementable encoding can be done using a pixel array detector (or ICCD camera) gated to record according to a specified Hadamard probe sequence but reading out data only at the end of each probe sequence.

The HATRX method thus enables fast time-resolved crystallographic experiments on both reversible and irreversible processes at synchrotron sources where currently the flux density achievable at the sample is the limiting factor. Though HATRX is demonstrated here with millisecond time-resolution, the method can be extended to shorter time-scales. This removes the significant experimental barrier of source flux density and greatly increases the number of synchrotron beamlines where time-resolved structural experiments are possible. In addition, its applicability to any experimental technique where the probe can be encoded makes this a general tool for dynamic studies.

Time-resolved methods can be used to characterise the contribution of structural dynamics to biological processes, such as protein folding, force transfer, ligand binding and enzyme catalysis. The HATRX method is particularly suited to the observation of short-range (1 - 5 Å)

atomic motions that occur on time-scales from picoseconds to seconds. The technique is therefore best applied to the study of enzyme catalysis to highlight the effect of small structural changes in the protein (side chain motion, loop dynamics) on the chemical properties of the active site and to observe the breaking and formation of chemical bonds. This will aid in the elucidation of the mechanisms of catalytic reactions occurring in enzyme active sites. Larger atomic motions (*i.e*. domain rearrangements) can be followed using scattering techniques such as SAXS[201], here protein motions are not limited by the crystal lattice. Mixing methods, i.e. stop-flow methodologies, can reach microsecond time-resolutions. However, with the addition of the Hadamard transform and photoactivation much faster time-resolutions are feasible.

When applied to time-resolved spectroscopy the Hadamard method will enhance the available signal when following the time-scales of chemical reactions with femtosecond time-resolutions. The addition of fluorescent markers, such as in Forster resonance energy transfer spectroscopy (FRET)[202], extends this to the observation of long-range spatial changes that occur during protein folding, ligand binding and force transfer.

The structural changes that occur during the transfer of force through 'mechanical proteins' occur on much longer time-scales and involve large dynamic motions. These can be followed using electron microscopy, which enables direct visualisation of molecules with spatial resolutions of up to 4Å and millisecond time-resolution[3,203–205]. The large-scale structural changes accompanying protein folding and ligand binding occur on time scales ranging from nanoseconds to seconds and Nuclear magnetic resonance (NMR) can be used to probe changes in structure with atomic resolution across these time-scales[1,2,191,206–208]. This method has been applied to protein folding and ligand binding studies. NMR relaxation techniques can also be used to characterise thermal motions in proteins with pico-second time-

resolution[54,207]. These methods can be combined to build a comprehensive view of the role of dynamics in protein function. This information can be fed into molecular dynamics simulations providing better force fields with which the physical properties of amino-acid sequences can be predicted[209–211].

Chapter 6 Discussion

This thesis presents four studies that have been carried out in order to address the challenges currently faced when performing time-resolved crystallography. Namely, 1) the effects of radiation damage during data collection, 2) the need to synchronise the structural changes in every molecule in the crystal and the limitations faced when studying irreversible reactions and 3) the time-resolutions that can be achieved using standard 3rd generation synchrotron beamlines.

6.1 The effects of radiation damage during data collection

The UV-Vis study of low dose radiation damage to metalloproteins confirmed the findings of Beitlich et al[131]. that the maximum population of solvated electrons is reached after a dose of 45 kGy; this is three orders of magnitude smaller than the diffracting power dose limit[154]. X-ray diffraction is not a sensitive enough probe to track radiation damage and complementary methods are essential if we are to know which electronic state of the protein the data describes. The data reported here do suggest that the modification of crystallisation conditions may be useful in order to somewhat extend the lifetime of metalloproteins in the X-ray beam, so that more exposures may be collected before the damaging dose is absorbed, however any gain is likely to be small. Radiation damage, however, does not dependend on dose-rate, rather the amount of diffraction data collected is directly proportional to the number of photons incident on the crystal. Reducing the dose rate will in turn reduce the resolution of the measured diffraction. A compromise between the required resolution and the number of images must therefore be decided on a case by case basis.

Very recent studies have suggested that in certain circumstances radiation damage can be 'outrun'. For example, data collection using the free electron laser has shown that when using a very intense source (high dose rate), diffraction can be recorded from a crystal before radiation damage has time to propagate in the crystal[113]. This phenomenon has also been observed by combining synchrotron radiation (dose rate = 4.8 MGy s^{-1} at 12.8 keV) with a fast photon counting detector (500 Hz, PILATUS)[212]. However, these dose rates are not reached in standard data collections at synchrotron sources and so the best method for avoiding the effects of radiation damage is by collecting a composite dataset from many crystals, with each receiving a small dose.

Complementary to UV-vis measurements of radiation induced changes, is the application of X-ray excited optical luminescence to macromolecular crystallography. This study has built upon early reports of the phenomena and suggests that it can offer insight into the detrimental side effects of using X-rays as a site-specific structural probe, although it is probably not useful as a general metric of overall radiation damage. An exciting possibility is the combination of XEOL other methods such as electron paramagnetic resonance to bring us closer to modelling the electro-chemical processes occurring as diffraction data is collected. This would allow better estimates of the undamaged (zero dose) structure, and ensure that structural changes observed during time-resolved experiments are functionally related and not simply a result of radiation damage. The advantage of using XEOL to probe radiation damage is that it is an entirely passive experiment. The signal appears during X-ray exposure and can be collected using the on-axis viewing microscopes that are ubiquitous on macromolecular beamlines. No modifications are needed to the beamline; the spectrophotometer can be placed distant to the sample environment with the signal carried by optical fibres. This is in contrast to UV-Vis and Raman spectroscopies, where bulky optical equipment must be placed directly in the sample environment, as illustrated in

figure 6.1, for an off-axis combined X-ray diffraction and UV-Vis spectroscopy experiment at Biocars beamline 14-BMC.

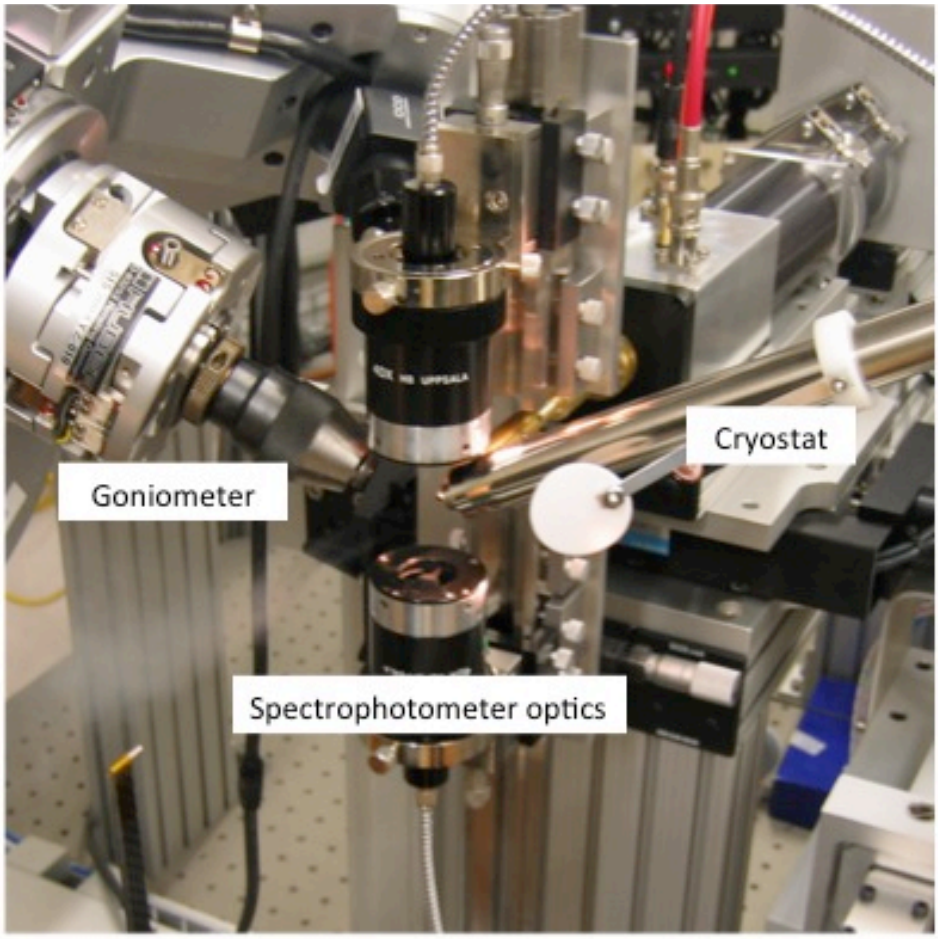

Figure 6.1: Crowded sample environment at BioCars MX beamline (APS) with off-axis spectroscopy set-up. Using this equipment can block certain sample geometries, and limit data collection. Image modified from original supplied by A.Pearson.

The physical processes occurring during the first stages of radiation damage have been well characterised[83], but the mechanisms relating these to site specific damage and the loss of diffraction are still unclear. Structural data disappears as damage increases and so complementary methods are essential if we are to fully understand the processes linking radicalisation of protein and solvent atoms, to the propagation of site-specific structural changes in the protein and the eventual loss off diffraction. Wavelength specific changes in the XEOL spectrum that observed with increasing dose provide a promising method with which to probe these mechanisms. To use XEOL as a probe in these studies, the spectra must first be further characterised

in order to assign the origins of spectral features. Using point mutation libraries it should be possible to identify the spectral changes that accompany particular structural changes, for example mutating phenylalanine to leucine will show the effect of removing an aromatic residue whilst ensuring the size of the residue is similar.

6.2 The challenge of synchronisation & irreversible reactions

To address the challenge of synchronising structural changed throughout the crystal, we have demonstrated the use of a photocaged substrate in an irreversible enzymatic reaction. In addition it is shown that composite datasets collected from micro crystals at a 3rd generation synchrotron source yield sufficiently accurate data to identify intermediate structures in the photoactivatable reaction.

The structure of an intermediate species in the photolytic cleavage of the bond between L-aspartate and o-nitrobenzyl methaldehyde has been solved at 100 K after photolysis at room temperature. L-Asparate α-decarboxylase has proven to be a particularly suitable test system for this method, it is easy to grow a range of differently sized crystals, the crystals diffract well and are exceptionally resistant to radiation damage (with successful data collection of both monochromatic and Laue data at room temperature), and the synthesis of the photocaged substrate is relatively simple. However, the presence of a stable intermediate suggests that in crystalline conditions the liberated photocage may interfere with further progression of the enzymatic reaction, perhaps by chemical interactions with the active site or by sterically hindering the formation of active conformations.

Further improvements to this experiment will include the synthesis of more appropriate photocages, *i.e.* those that will absorb light away from the absorption of aromatic amino acids (ideally above 300 nm) and those with a faster rate of decaging to increase the time-resolution of the experiment and ensure synchronisation between the reactions occurring in each molecule in the crystal. This will allow us to collect

time-resolved datasets from the ADC system. The current proposed mechanism is based on the mass to charge ratio of chemically trapped intermediates identified using electrospray mass spectrometry (ESMS)[171]. Using time-resolved X-ray crystallography we will not only be able to verify these results but we will also be able to provide a detailed description of the structural contributions to the chemical reaction, the structural data will also be used to determine if structural features distant to the active site can be utilised for allosteric control of the reaction.

6.3 Improving the achievable time-resolution - HATRX

Finally, I have developed a method to address the limits that flux imposes on the time-resolution of crystallographic experiments. By multiplexing time-points on the detector, the flux across a whole pulse sequence is measured and then transformed to give the intensities of each reflection at every time point along the reaction coordinate. This means that by using the HATRX method the minimum flux can be delivered over a series of shorter time-points rather than a single time-point, which utilises the broad bandwidth of a Laue beam, in the traditional pump-probe crystallography experiment.

The HATRX experiment has been demonstrated by simulating the encoding using real X-ray diffraction data. We have shown that it is possible to deconvolute the time domain from multiplexed data in order to obtain time-resolved electron density maps. The predicted benefits of this method, including decreased sample consumption, improved signal to noise ratio, and most importantly increased time resolution will open up the field of time-resolved structural biology to new systems using standard crystallographic synchrotron beamlines, especially when combined with the multicrystal method to enable irreversible reactions to be studied.

The experimental set-up is now in place to test the HATRX method by gating a PILATUS[80] detector according to the pulse sequence. This method can be applied to both macromolecular and small molecule

crystallography. Using the detector to encode the pulse sequence into data collection means that the method is now easily transferrable between beamlines and can be performed with no additional specialist equipment.

6.4 Summary

I have demonstrated a new method that aims to make time-resolved structural experiments more generally available. In addition, I have described a fundamental studies of radiation damage processes that provides a potential passive measurement of site-specific damage that does not require much modification to existing beamlines. Such complementary experiments, as shown in our dose-rate study, provide guidance for optimal experimental design and will help improve the quality of time-resolved structural data.

Time-resolved structural data will not only provide mechanistic insight specific to the systems studied, it will also provide a wealth of information from which improvements to molecular dynamics force fields can be made[210,213]. Simulations of molecular processes enable predictions to be made about the functions of certain structural motifs[209,214] and the effects of perturbing the amino acid sequences of biomolecules[215] on their structure and function. To justify these predictions, molecular dynamics calculations must be accompanied by approximations based on the most detailed and reliable experimental measurements. For many systems we only have structures of a single state from which simulations must currently extrapolate.

7 Bibliography

1. Buck, J., Fürtig, B., Noeske, J., Wöhnert, J. & Schwalbe, H. Time-resolved NMR methods resolving ligand-induced RNA folding at atomic resolution. *Proc. Natl. Acad. Sci. U. S. A.* **104,** 15699–704 (2007).

2. Kay, L. E. NMR studies of protein structures and dynamics. *J. Magn. Reson.* **173,** 193–207 (2005).

3. White, H. D., Thirumurugan, K., Walker, M. L. & Trinick, J. A second generation apparatus for time-resolved electron cryo-microscopy using stepper motors and electrospray. *J. Struct. Biol.* **144,** 246–252 (2003).

4. Batson, P. E. Unlocking the time resolved nature of electron microscopy. *Proc. Natl. Acad. Sci. U. S. A.* **108,** 3099–100 (2011).

5. Barnard, D. *et al.* Time Resolved Cryo-Electron Microscopy Of Ribosome Assembly using Microfluidic Mixing. *Microsc. Microanal.* **15,** 942–943 (2009).

6. Moffat, K. Time-resolved crystallography. *Acta Crystallogr. A.* **54,** 833–41 (1998).

7. Stoddard, B. L. New results using Laue diffraction and time-resolved crystallography. 612–618 (1998).

8. Moffat, K. Time-resolved biochemical crystallography: a mechanistic perspective. *Chem. Rev.* **101,** 1569–81 (2001).

9. Helliwell, J. R. Synchrotron X-Ray Crystallography Techniques: Time-Resolved Aspects of Data Collection. *Philos. Trans. R. Soc. A Math. Phys. Eng. Sci.* **340,** 221–232 (1992).

10. Kendrew, J. C. & Perutz, M. F. X-ray studies of compounds of biological interest. *Annu rev Biochem* **26,** 327–372 (1957).

11. Doscher, M. S., Frederic, M. & Richards, M. ARTICLE : The Activity of an Enzyme in the Crystalline State : Ribonuclease S The Activity of an Enzyme in the Crystalline State : Ribonuclease S *. (1963).

12. Richards, M. The Activity of an Enzyme in the Crystalline State : Ribonuclease S *. **238,** (1963).

13. Mozzarelli, A. & Rossi, G. L. PROTEIN FUNCTION IN THE. (1996).

14. Porter, G. Flash photolysis and spectroscopy. A new method for the study of free radical reactions. *Proc. R. Soc. Lond. A* **200,** (1950).

15. Chance, B. THE KINETICS OF THE ENZYME-SUBSTRATE COMPOUND OF PEROXIDASE. *J. Biol. Chem.* **151,** 553–557 (1943).

16. Porter G. *Nobel Symposium 5. Fast Reactions and Primary Processes in Reaction Kinetics*. (Interscience, 1967).

17. Holten, D. & Windsor, M. W. PICO SECOND FLASH PHOTOLYSIS IN BIOLOGY AND BIOPHYSICS. 189–227 (1978).

18. Zewail, A. H. *Femtochemistry: Ultrafast Dynamics of the Chemical Bond*. **1,** (World Scientific, 1994).

19. Hopkin, K. Bright Ideas. *Sci.* (2009). at <http://classic.xn--the-scientist-em6g.com/2009/5/1/48/1/>

20. Makinen, M. W. & Fink, A. L. Reactivity and Cryoenzymology of Enzymes in the Crystalline State. *Annu. Rev. Biophys. Bioeng.* **6,** 301–343 (1977).

21. Blake, C. X-Ray Cryoenzymology. *Nature* **263,** 273–274 (1976).

22. Blake, C. C. F. *et al.* Crystallographic Studies of the Activity of Hen Egg-White Lysozyme. *Proc. R. Soc. B Biol. Sci.* **167,** 378–388 (1967).

23. Berni, R., Ozzarelli, A. & Pellacani, L. Catalytic and Regulatory Properties of D-Glyceraldehyde-3-Phosphate Dehydrogenase in the Crystal. 405–415 (1977).

24. Bolduc, J. M. *et al.* Mutagenesis and Laue structures of enzyme intermediates: isocitrate dehydrogenase. *Science* **268,** 1312–8 (1995).

25. Wang, J. I. E. & Kantrowitz, E. R. Trapping the tetrahedral intermediate in the alkaline phosphatase reaction by substitution of the active site serine with threonine. **2000,** 2395–2401 (2006).

26. Pearson, A. R., Mozzarelli, A. & Rossi, G. L. Microspectrophotometry for structural enzymology. *Curr. Opin. Struct. Biol.* **14,** 1–7 (2004).

27. Quiochot, F. A., Richards, F. M. & Richards, F. M. The Enzymic Behavior of Carboxypeptidase-A in the Solid State". (1964).

28. Mozzarelli, A. & Rossi, G. L. Protein Function in the Crystal. *Annu. Rev. Biophys. Biomol. Struct.* **25,** 343–365 (1996).

29. Douzou, P., Hui, G. & Hoa, B. O. N. Pro & h Crystallography at Sub-zero Temperatures : Lysozyme-Substrate Complexes in Cooled Mixed Solvents. 367–380 (1974).

30. Fink, A. L. & Ahmed, A. I. Formation of Stable Crystalline Enzyme-Substrate Intermediates at Sub-Zero Temperatures. *Nature* **263,** 294–297 (1976).

31. Petsko, G., Alber, T. & Tsernoglou, D. Crystal structure of elastase-substrate complex at -55 oC. **263,** (1976).

32. Weik, M. & Colletier, J.-P. Temperature-dependent macromolecular X-ray crystallography. *Acta Cryst* **D66,** 437–446 (2010).

33. Schmidt, M. Mix and Inject : Reaction Initiation by Diffusion for Time-Resolved Macromolecular Crystallography. **2013,** (2013).

34. Kovaleva, E. G. & Lipscomb, J. D. Crystal Structures of Fe2+ Dioxygenase Superoxo, Alkylperoxo, and Bound Product Intermediates. *Science (80-.).* **316,** 453–457 (2007).

35. Reid, T. S., Terry, K. L., Casey, P. J. & Beese, L. S. Crystallographic analysis of CaaX prenyltransferases complexed with substrates defines rules of protein substrate selectivity. *J. Mol. Biol.* **343,** 417–33 (2004).

36. Bartunik, H. D. & Jerzembek, E. Time-resolved study of dynamics of proteins uing synchrotron radiation and laser excitation. *Acta Cryst* **A37,** C51–C52 (1981).

37. Search, H., Journals, C., Contact, A., Iopscience, M. & Address, I. P. Central data collection facility for protein crystallography, small angle diffraction and scattering at the Daresbury Laboratory Synchrotron Radiation Source (SRS), England. **1363,**

38. Batterman, B. W. & Ashcroft, N. W. CHESS: The New Synchrotron Radiation Facility at Cornell. *Science* **206,** 157–61 (1979).

39. Greenhough, T. J. & Helliwell, J. R. The uses of synchrotron X-radiation in the crystallography of molecular biology. *Prog. Biophys. Mol. Biol.* **41,** 67–123 (1983).

40. Frauenfelder, H., Petsko, G. A. & Tsernoglou, D. Temperature-dependent X-ray diffraction as a probe of protein structural dynamics. *Nature* **80,** 558–563 (1979).

41. Bilderback, D., Moffat, K. & Szebenyli, D. Time-resolved Laue diffraction from protein crystals: instrumental considerations. **222,** 245–251 (1984).

42. Moffat, K., Bilderback, D., Schildkamp, W., Szebenyli, D. & Loane, R. in *Struct. Biol. Appl. X-ray absorption, Scatt. Diffr.* 125–133 (Academic Press, 1986).

43. Wagenfeld, H. Ewald's and von Laue's dynamical theories of X-ray diffraction. *Acta Crystallogr. Sect. A Cryst. Physics, Diffraction, Theor. Gen. Crystallogr.* **24,** 170–174 (1968).

44. Helliwell, J. R. *Macromolecular Crystallography with synchrotron radiation*. (Cambridge University Press, 2005).

45. Ren, Z. *et al.* Laue crystallography: coming of age. *J. Synchrotron Radiat.* **6,** 891–917 (1999).

46. Moffat, K. TIME-RESOLVED CRYSTALLOGRAPHY. (1989).

47. Hadju, J. *et al.* Millisecond X-ray diffraction and the first electron density map from Laue photographs of a protein crystal. *Nature* **327,** 617–618 (1987).

48. Bartunik, H. ~D. Low-temperature and time-resolved protein crystallography using synchrotron radiation. *Nucl. Instruments Methods Phys. Res.* **208,** 523–533 (1983).

49. Stoddard, B. L. & Hutchinson, F. Time-resolved X-ray Crystallography. (2002).

50. Wu, N., Deiters, A., Cropp, T. A., King, D. & Schultz, P. G. A Genetically Encoded Photocaged Amino Acid. 14306–14307 (2004).

51. Abbruzzetti, S., Sottini, S., Viappiani, C. & Corrie, J. E. T. Kinetics of Proton Release after Flash Photolysis of 1- (2-Nitrophenyl) ethyl Sulfate (Caged Sulfate) in Aqueous Solution. **127,** 3709–3713 (2005).

52. Chin, J. W., Martin, A. B., King, D. S., Wang, L. & Schultz, P. G. Addition of a photocrosslinking amino acid to the genetic code of Escherichia coli. (2002).

53. Lee, H.-M., Larson, D. R. & Lawrence, D. S. Illuminating the Chemistry of Life: Design, Synthesis, and Applications of

"Caged" and Related Photoresponsive Compounds. *ACS Chem. Biol.* **4,** 409–427 (2009).

54. Bourgeois, D. *et al.* Complex landscape of protein structural dynamics unveiled by nanosecond Laue crystallography. *Proc. Natl. Acad. Sci. U. S. A.* **100,** 8704–9 (2003).

55. Bourgeois, D. *et al.* Extended subnanosecond structural dynamics of myoglobin revealed by Laue crystallography. *Proc. Natl. Acad. Sci. U. S. A.* **103,** 4924–9 (2006).

56. Schotte, F. *et al.* Watching a Protein as it Functions with 150-ps Time-Resolved X-ray Crystallography 10.1126/science.1078797. *Science (80-.).* **300,** 1944–1947 (2003).

57. Schotte, F., Soman, J., Olson, J. S., Wulff, M. & Anfinrud, P. A. Picosecond time-resolved X-ray crystallography: probing protein function in real time. *J. Struct. Biol. Imaging Macromol. Process. Interact.* **147,** 235–246 (2004).

58. Schmidt, M. *et al.* Ligand migration pathway and protein dynamics in myoglobin: a time-resolved crystallographic study on L29W MbCO. *Proc. Natl. Acad. Sci. U. S. A.* **102,** 11704–9 (2005).

59. Srajer, V. *et al.* Protein conformational relaxation and ligand migration in myoglobin: a nanosecond to millisecond molecular movie from time-resolved Laue X-ray diffraction. *Biochemistry* **40,** 13802–15 (2001).

60. Srajer, V. *et al.* Photolysis of the carbon monoxide complex of myoglobin: nanosecond time-resolved crystallography. *Science* **274,** 1726–9 (1996).

61. Ren, Z. *et al.* A Molecular Movie at 1.8 Å Resolution Displays the Photocycle of Photoactive Yellow Protein, a Eubacterial Blue-Light Receptor, from Nanoseconds to Seconds. *Biochemistry* **40,** 13788–13801 (2001).

62. Ihee H. Srajer V., Pahl R., Anderson S., Schmidt M., Schotte F., Anfinrud P., Wulff M., Moffat K.,, R. S. Visualising reaction pathways in photoactive yellow protein from nanoseconds to seconds. *Proc. Natl. Acad. Sci.* **102,** 7145–7150 (2005).

63. Rajagopal, S., Schmidt, M., Anderson, S., Ihee, H. & Moffat, K. Analysis of experimental time-resolved crystallographic data by singular value decomposition. *Acta Crystallogr. D. Biol. Crystallogr.* **60,** 860–71 (2004).

64. Schmidt, M. *et al.* Protein kinetics : Structures of intermediates and reaction mechanism from time-resolved x-ray data. (2004).

65. Anderson, S. *et al.* Chromophore Conformation and the Evolution of Tertiary Structural Changes in Photoactive Yellow Protein. *Structure* **12,** 1039–1045 (2004).

66. Tripathi, S., Šrajer, V., Purwar, N., Henning, R. & Schmidt, M. pH dependence of the photoactive yellow protein photocycle investigated by time-resolved crystallography. *Biophys. J.* **102,** 325–332 (2012).

67. Perman, B. *et al.* Energy Transduction on the Nanosecond Time Scale: Early Structural Events in a Xanthopsin Photocycle. *Science (80-.).* **279,** 1946–1950 (1998).

68. Genick, U. K., Soltis, S. M., Kuhn, P., Canestrelli, I. L. & Getzoff, E. D. Structure at 0.85 Å resolution of an early protein photocycle intermediate. *Nature* **392,** 206–209 (1998).

69. Schmidt, M., Graber, T., Henning, R. & Srajer, V. Five-dimensional crystallography. *Acta Crystallogr. A.* **66,** 198–206 (2010).

70. Jung, Y. O. *et al.* Volume-conserving trans–cis isomerization pathways in photoactive yellow protein visualized by picosecond X-ray crystallography. *Nat. Chem.* **5,** 212–220 (2013).

71. Baxter, R. H. G. *et al.* Time-resolved crystallographic studies of light-induced structural changes in the photosynthetic reaction center. *Proc. Natl. Acad. Sci. U. S. A.* **101,** 5982–7 (2004).

72. Wöhri, A. B. *et al.* Light-induced structural changes in a photosynthetic reaction center caught by Laue diffraction. *Science* **328,** 630–3 (2010).

73. Ren, Z., Srajer, V., Knapp, J. E. & Royer, W. E. Cooperative macromolecular device revealed by meta-analysis of static and time-resolved structures. *Proc. Natl. Acad. Sci. U. S. A.* **109,** 107–12 (2012).

74. Hori, T. *et al.* The initial step of the thermal unfolding of 3-isopropylmalate dehydrogenase detected by the temperature-jump Laue method. *Protein Eng.* **13,** 527–33 (2000).

75. Key, J., Srajer, V., Pahl, R. & Moffat, K. Time-resolved crystallographic studies of the heme domain of the oxygen sensor FixL: structural dynamics of ligand rebinding and their relation to signal transduction. *Biochemistry* **46,** 4706–15 (2007).

76. Singer, P., Smalas, A. O., Carty, R., Mangel, W. & Sweet, R. M. The hydrolytic water molecule in trypsin, revealed by time-resolved Laue crystallography. *Science (80-.).* **259,** (1993).

77. Zhao, J., Srajer, V. & Franzen, S. Functional Consequences of the Open Distal Pocket of Dehaloperoxidase-Hemoglobin Observed by Time-Resolved X - ray Crystallography. (2013).

78. Cammarata, M. *et al.* Chopper system for time resolved experiments with synchrotron radiation. *Rev. Sci. Instrum.* **80,** 15101 (2009).

79. Neutze, R. & Moffat, K. Time-resolved structural studies at synchrotrons and X-ray free electron lasers: opportunities and challenges. *Curr. Opin. Struct. Biol.* **22,** 651–659 (2012).

80. Broennimann, C. *et al.* The PILATUS 1M detector. *J. Synchrotron Radiat.* **13,** 120–130 (2006).

81. Eikenberry, E. F. *et al.* PILATUS: a two-dimensional X-ray detector for macromolecular crystallography. *Nucl. Instrum. Methods A* **501,** 260–266 (2003).

82. Rajendran, C., Dworkowski, F. S. N., Wang, M. & Schulze-Briese, C. Radiation damage in room-temperature data acquisition with the PILATUS 6M pixel detector. *J. Synchrotron Rad.* **18,** 318–328 (2011).

83. Garman, E. Radiation damage in macromolecular crystallography: what is it and why should we care? *Acta Cryst* **D66,** 339–351 (2010).

84. Kalinowski, J. a, Fournier, B., Makal, A. & Coppens, P. The LaueUtil toolkit for Laue photocrystallography. II. Spot finding and integration. *J. Synchrotron Radiat.* **19,** 637–46 (2012).

85. Ulrich, O. *et al.* A new white beam x-ray microdiffraction setup on the BM32 beamline at the European Synchrotron Radiation Facility. *Rev. Sci. Instrum.* **82,** 033908 (2011).

86. Zhao, Y. & Schmidt, M. New software for the singular value decomposition of time-resolved crystallographic data. *J. Appl. Cryst* **42,** 734–740 (2009).

87. Schmidt, M., Rajagopal, S., Ren, Z. & Moffat, K. Application of singular value decomposition to the analysis of time-resolved macromolecular x-ray data. *Biophys. J.* **84,** 2112–29 (2003).

88. Holton, J. A beginner's guide to radiation damage. *J. Synch. Rad.* **16,** 133–142 (2009).

89. Warkentin, M. *et al.* Global radiation damage: temperature dependence, time dependence and how to outrun it. *J. Synch. Rad.* **20,** 7–13 (2013).

90. Meents, A., Gutmann, S., Wagner, A. & Schulze-Briese, C. Origin and temperature dependence of radiation damage in biological samples at cryogenic temperatures. *Proc. Natl. Acad. Sci. USA* **107,** 1094–1099 (2010).

91. Garman, E. `Cool crystals': Cryocrystallography and Radiation Damage. *Curr. Opin. Struct. Biol.* **9,** 545–551 (2003).

92. Parkin, S. & Hope, H. Macromolecular Cryocrystallography: Cooling, Mounting, Storage and Transportation of Crystals. *J. Appl. Cryst.* **31,** 945–953 (1998).

93. Henderson, R. Cryo-protection of protein crystals against radiation damage in electron and X-ray diffraction. *Proc. R. Soc. Lond. B* **241,** 6–8 (1990).

94. Garman, E. & Owen, R. L. in *Macromol. Crystallogr. Protoc.* **364,** 1–18 (Humana Press, 2007).

95. Gonzalez, A., Thompson, A. W. & Nave, C. Cryo-protection of protein crystals in intense X-ray beams. *Rev. Sci. Instrum.* **63,** 1177–1180 (1992).

96. Garman, E. & Schneider, T. Macromolecular Cryocrystallography. *J. Appl. Cryst.* **30,** 211–237 (1997).

97. Jones, G., Lea, J., Symons, M. & Taiwo, F. Structure and mobility of electron gain and loss centres in proteins. *Nature* **330,** 772–773 (1987).

98. Burmeister, W. Structural changes in a cryo-cooled protein crystal owing to radiation damage. *Acta Cryst* **D56,** 328–341 (2000).

99. Ravelli, R. & McSweeney, S. The `fingerprint' that X-rays can leave on structures. *Structure* **8,** 315–328 (2000).

100. Weik, M. *et al.* Specific chemical and structural damage to proteins produced by synchrotron radiation. *Proc. Natl. Acad. Sci. USA* **97,** 623–628 (2000).

101. McGeehan, J. *et al.* Colouring cryo-cooled crystals: online microspectrophotometry. *J. Synch. Rad.* **16,** 163–172 (2009).

102. Owen, R. L. *et al.* A new on-axis multimode spectrometer for the macromolecular crystallography beamlines of the Swiss Light Source. *J. Synch. Rad.* **16,** 173–182 (2009).

103. Pearson, A. R. & Owen, R. L. Combining X-ray crystallography and single-crystal spectroscopy to probe enzyme mechanisms. *Biochem. Soc. Trans.* **037,** 378–381 (2009).

104. Carey, P. R. Raman Spectroscopy, the Sleeping Giant in Structural Biology, Awakes. *J. Biol. Chem.* **274,** 26625–26628 (1999).

105. Davies, R. J., Burghammer, M. & Riekel, C. A combined microRaman and microdiffraction set-up at the European Synchrotron Radiation Facility ID13 beamline. *J. Synch. Rad.* **16,** 22–29 (2009).

106. Corbett, M. C. *et al.* Photoreduction of the active site of the metalloprotein putidaredoxin by synchrotron radiation. *Acta Cryst* **D63,** 951–960 (2007).

107. Holton, J. XANES measurements of the rate of radiation damage to selenomethionine side chains. *J. Synch. Rad.* **14,** 51–72 (2007).

108. Yano, J. *et al.* X-ray damage to the Mn4Ca complex in single crystals of photosystem II: A case study for metalloprotein crystallography. *Proc. Natl. Acad. Sci. USA* **102,** 12047–12052 (2005).

109. Ellis, M. J., Buffey, S. G., Hough, M. A. & Hasnain, S. S. On-line optical and X-ray spectroscopies with crystallography: an integrated approach for determining metalloprotein structures in functionally well defined states. *J. Synch. Rad.* **15,** 433–439 (2008).

110. Sutton, K. A. *et al.* Insights into the mechanism of X-ray induced disulfide bond cleavage in lysozyme crystals based on EPR, optical absorption, and X-ray diffraction studies. *Acta Cryst* **In press,** (2013).

111. SLAC. Linac coherent light source.

112. Chapman, H. N. *et al.* Femtosecond X-ray protein nanocrystallography. *Nature* **470,** 73–77 (2011).

113. Barty, A., Caleman, C. & Chapman, H. N. Self-terminating diffraction gates femtosecond X-ray nanocrystallography measurements. 35–40 (2011). doi:10.1038/nphoton.2011.297

114. Aquila, A. *et al.* Time-resolved protein nanocrystallography using an X-ray free-electron laser. *Opt. Express* **20,** 2706–2716 (2012).

115. Bogan, M. J. *et al.* Single-shot femtosecond x-ray diffraction from randomly oriented ellipsoidal nanoparticles. **094701,** 1–7 (2010).

116. Kirian, R. A. *et al.* Femtosecond protein nanocrystallography — data analysis methods. **18,** 5713–5723 (2010).

117. Kirian, R. a *et al.* Structure-factor analysis of femtosecond microdiffraction patterns from protein nanocrystals. *Acta Crystallogr. A.* **67,** 131–40 (2011).

118. White, T. A. *et al.* CrystFEL : a software suite for snapshot serial crystallography. 335–341 (2012). doi:10.1107/S0021889812002312

119. Barends, T. R. M. *et al.* De novo protein crystal structure determination from X-ray free-electron laser data. *Nature* **505,** 244–7 (2014).

120. Bakker, S. *et al.* Dynamic structural science : developing the tools to probe biological mechanism in atomic detail.

121. Axford, D. *et al.* In-situ macromolecular crystallography using microbeams. *Acta Cryst* **D68,** 592–600 (2012).

122. Aishima, J. *et al.* High-speed crystal detection and characterization using a fast-readout detector. *Acta Cryst* **D66,** 1032–1035 (2010).

123. Southworth-Davies, R. J. & Garman, E. F. Radioprotectant screening for cryocrystallography. *J. Synch. Rad.* **14,** 73–83 (2007).

124. Blake, C. & Phillips, D. C. Biological effects of ionising radiation at molecular level. *Proc. Symp. Biol. Eff. Ionis. Radiat. Mol. level. Vienna* 183–191 (1962).

125. Teng, T. Y. Mounting of Crystals for Macromolecular Crystallography in a Free-Standing Thin Film. *J. Appl. Cryst.* **23,** 387–391 (1990).

126. Garman, E. F. & McSweeney, S. M. Progress in research into radiation damage in cryo-cooled macromolecular crystals doi:10.1107/S0909049506053015. *J. Synchrotron Radiat.* **14,** 1–3 (2007).

127. Henderson, R. Cryo-Protection of Protein Crystals against Radiation Damage in Electron and X-Ray Diffraction. *Proc. R. Soc. B Biol. Sci.* **241,** 6–8 (1990).

128. Garman, E. F. & Grime, G. W. Elemental analysis of proteins by microPIXE. *Prog. Biophys. Mol. Biol.* **89,** 173–205 (2005).

129. Hough, M. A., Antonyuk, S. V, Strange, R. W., Eady, R. R. & Hasnain, S. S. Crystallography with Online Optical and X-ray Absorption Spectroscopies Demonstrates an Ordered Mechanism in Copper Nitrite Reductase. *J. Mol. Biol.* **378,** 353–361 (2008).

130. Olieric, V. *et al.* Using X-ray absorption spectra to monitor specific radiation damage to anomalously scattering atoms in macromolecular crystallography doi:10.1107/S0907444907019580. *Acta Cryst Crystallogr. Sect. D* **63,** 759–768 (2007).

131. Beitlich, T., Kuhnel, K., Schulze-Briese, C., Shoeman, R. L. & Schlichting, I. Cryoradiolytic reduction of crystalline heme proteins: analysis by UV-Vis spectroscopy and X-ray crystallography. *J. Synch. Rad.* **14,** 11–23 (2007).

132. Carey, P. R. Raman crystallography and other biochemical applications of Raman microscopy. *Annu. Rev. Phys. Chem.* **57,** 527 LP – 554 (2006).

133. Sanishvili, R. G., Margoliash, E., Westbrook, M. L., Westbrook, E. M. & Volz, K. W. Crystallization of wild-type and mutant ferricytochromes c at low ionic strength: seeding technique and X-ray diffraction analysis. *Acta Cryst* **D50,** 687–694 (1994).

134. Gasyna, Z. Transient intermediates in the reduction of Fe(III) myoglobin-ligand complexes by electrons at low temperature. *Biochim. Biophys. Acta Cryst - Protein Struct.* **577,** 207–216 (1979).

135. Keilin, D. & Slater, E. C. Cytochrome. *Br. Med. Bull.* **9,** 89–96 (1953).

136. Paithankar, K. S., Owen, R. L. & Garman, E. F. Absorbed dose calculations for macromolecular crystals: improvements to RADDOSE. *J. Synch. Rad.* **16,** 152–162 (2009).

137. Mcgeehan, J., Ravelli, R. B. G., Murray, J. W. & Garman, E. F. Colouring cryo-cooled crystals : online microspectrophotometry. **0495,** 163–172 (2008).

138. Kmetko, J., Husseini, N. S., Naides, M., Kalinin, Y. & Thorne, R. E. Quantifying X-ray radiation damage in protein crystals at cryogenic temperatures. *Acta Cryst* **D62,** 1030–1038 (2006).

139. Ershov B, G. & Pikaev A, K. in *Radiat. Chem.* 1–24 (American Chemical Society, 1968). doi:10.1021/ba-1968-0081.ch001

140. Denisov, I. G., Victoria, D. C. & Sligar, S. G. Cryoradiolytic reduction of heme proteins: Maximizing dose-dependent yield. *Radiat. Phys. Chem.* **76,** 714–721 (2007).

141. Trincao, J., Hamilton, M. L., Christensen, J. & Pearson, A. R. Dynamic structural science: recent developments in time-resolved spectroscopy. *Biochem. Soc. Trans.* **41,** 1260–1264 (2013).

142. Nummedal, D. & Steen, H. B. On the X-ray-induced thermoluminescence of some proteins in the dry state and in solution. *Radiat. Res.* **39,** 241–251 (1969).

143. Nelson, D. R., Carter, J. G., Birkhoff, R. D., Hamm, R. N. & Augenstein, L. G. Yield of luminescence from X-irraditated biochemicals. *Radiat. Res.* **32,** 723–743 (1967).

144. Carter, J. G., Nelson, D. R. & Augenstein, L. G. Effect of temperature on X-ray induced light emission from powders of amino acids and trypsin. *Arch. Biochem. Biophys.* **111,** 270–282 (1965).

145. Rogalev, A. & Goulon, J. in *Chem. Appl. Synchrotron Radiat. Part II X-ray Appl.* (ed. Sham, T. K.) **12B,** 707–760 (River Edge: World Scientific, 2002).

146. Hu, Y. F. *et al.* Soft x-ray excited optical luminescence: Some recent applications. in *Pap. from 12th Natl. Synchrotron Radiat. Instrum. Conf.* **73,** 1379–1381 (AIP, 2002).

147. Brocklehurst, B. Radio-luminescence of alkane solutions. Comparison of experiment and simulation over a wide energy range. *Chem. Phys. Lett.* **211,** 31–35 (1993).

148. Holroyd, R. A., Preses, J. M. & Hanson, J. C. The Linear Energy Transfer Dependence of Excited Singlet-State Lifetimes of Hydrocarbon Liquids Exposed to X Rays. *Rad Res* **135,** 312–314 (1993).

149. Nummedal, D. & Steen, H. B. On the x-ray-induced thermoluminescence of some proteins in the dry state and in solution. *Radiat. Res.* **39,** 241–51 (1969).

150. Engel, T. & Reid, P. J. *Physical chemistry*. (Pearson Benjamin Cummings, 2006). at <http://books.google.de/books?id=GmUvAQAAIAAJ>

151. Campeotto, I. *et al.* Structure of an Escherichia coli N-acetyl-d-neuraminic acid lyase mutant, E192N, in complex with pyruvate at 1.45 A resolution. *Acta Cryst* **F65,** 1088–1090 (2009).

152. Zhang, Z., Sauter, N. K., van den Bedem, H., Snell, G. & Deacon, A. M. Automated diffraction image analysis and spot searching for high-throughput crystal screening. *J. Appl. Cryst* **39,** 112–119 (2006).

153. Sauter, N. K. & Poon, B. K. Autoindexing with outlier rejection and identification of superimposed lattices. *J. Appl. Cryst* **43,** 611–616 (2010).

154. Owen, R. L., Rudino-Pinera, E. & Garman, E. F. Experimental determination of the radiation dose limit for cryocooled protein crystals. *Proc. Natl. Acad. Sci. USA* **103,** 4912–4917 (2006).

155. Beddard, G. *Applying Maths in the Chemical and Biomolecular Sciences: An Example-based Approach*. (OUP Oxford, 2009). at <http://books.google.de/books?id=7cWcAQAAQBAJ>

156. Steen, H. B. On the luminescence of L tryptophane and I tyrosine in aqueous solution at 77K induced by X-rays and UV light. *Photochem. Photobiol.* **6,** 805–816 (1967).

157. Steen, H. B. Luminescence of L tryptophan in the dry state and in aqueous solution induced by X-rays and UV light at 77K. *Photochem. Photobiol.* **8,** 47–51 (1968).

158. Adam, V. *et al.* Structural Basis of X-ray-Induced Transient Photobleaching in a Photoactivatable Green Fluorescent Protein. *J. Am. Chem. Soc.* **131,** 18063–18065 (2009).

159. Moniot, S. *et al.* Trapping of the thioacylglyceraldehyde-3-phosphate dehydrogenase intermediate from Bacillus stearothermophilus: direct evidence for a flip-flop mechanism. *J. Biol. Chem.* **283,** 21693–21702 (2008).

160. Kovaleva, E. G. & Lipscomb, J. D. Intermediate in the O-O Bond Cleavage Reaction of an Extradiol Dioxygenase. *Biochemistry* **47,** 11168–11170 (2008).

161. Charlier, C. *et al.* Nanosecond time scale motions in proteins revealed by high-resolution NMR relaxometry. *J. Am. Chem. Soc.* **135,** 18665–72 (2013).

162. Herbst, J., Heyne, K. & Diller, R. Femtosecond infrared spectroscopy of bacteriorhodopsin chromophore isomerization. *Science* **297,** 822–5 (2002).

163. Terner, J. & Campion, A. Time-resolved resonance Raman spectroscopy of bacteriorhodopsin on the millisecond timescale Chemistry : **74,** 5212–5216 (1977).

164. Balakrishnan, G., Weeks, C. L., Ibrahim, M., Soldatova, A. V & Spiro, T. G. Protein dynamics from time resolved UV Raman spectroscopy. *Curr. Opin. Struct. Biol. glycoconjugates / Biophys. methods* **18,** 623–629 (2008).

165. Rosell, F. I. & Mauk, a. G. Photochemical reagents for the study of metalloproteins by flash photolysis. *Coord. Chem. Rev.* **255,** 737–756 (2011).

166. Webb, M. E., Smith, G., Abell, C. & Smith, A. G. Biosynthesis of pantothenate. 695–721 (2004).

167. Zhang, S. *et al.* Mutations in panD encoding aspartate decarboxylase are associated with pyrazinamide resistance in Mycobacterium tuberculosis. (2013). doi:10.1038/emi.2013.38

168. Gopalan, G., Chopra, S., Ranganathan, A. & Swaminathan, K. SHORT COMMUNICATION Crystal Structure of Uncleaved L - Aspartate- a - decarboxylase From Mycobacterium tuberculosis. **802,** 796–802 (2006).

169. Schmitzberger, F. *et al.* Structural constraints on protein self-processing in L -aspartate- a -decarboxylase. **22,** 6193–6204 (2003).

170. Monteiro, D. C. F. *et al.* Formation of a heterooctameric complex between aspartate α-decarboxylase and its cognate activating factor, PanZ, is CoA-dependent. *Biochem. Biophys. Res. Commun.* **426,** 350–5 (2012).

171. Ramjee, M. K., Genschel, U., Abell, C. & Smith, A. G. Escherichia coli L-aspartate-a-decarboxylase: preprotein processing and observation of reaction intermediates by electrospray mass spectrometry. **669,** 661–669 (1997).

172. Lee, B. Il & Suh, S. W. Crystal Structure of the Schiff Base Intermediate Prior to Decarboxylation in the Catalytic Cycle of Aspartate a -Decarboxylase. 1–7 (2004). doi:10.1016/j.jmb.2004.04.049

173. Sanchez-Weatherby, J. *et al.* Improving diffraction by humidity control: a novel device compatible with X-ray beamlines. *Acta Crystallogr. D. Biol. Crystallogr.* **65,** 1237–46 (2009).

174. Kabsch, W. Automatic processing of rotation diffraction data from crystals of initially unknown symmetry and cell constants. *J. Appl. Cryst* **26,** 795–800 (1993).

175. Evans, P. An introduction to data reduction: space-group determination, scaling and intensity statistics. *Acta Cryst* **D67,** 282–292 (2011).

176. French, S. & Wilson, K. On the treatment of negative intensity observations. *Acta Crystallogr. Sect. A Found. Crystallogr.* **34,** 517–525 (1978).

177. Vagin, A. A. & Isupov, M. N. Spherically averaged phased translation function and its application to the search for molecules and fragments in electron-density maps. *Acta Cryst* **D57,** 1451–1456 (2001).

178. Murshudov, G. N. *et al.* REFMAC5 for the refinement of macromolecular crystal structures. *Acta Cryst* **D67,** 355–367 (2011).

179. Emsley, P. & Cowtan, K. Coot: Model-Building Tools for Molecular Graphics. *Acta Cryst* **D60,** 2126–2132 (2004).

180. Lebedev, A. a *et al.* JLigand: a graphical tool for the CCP4 template-restraint library. *Acta Crystallogr. D. Biol. Crystallogr.* **68,** 431–40 (2012).

181. Chen & al., et. Molprobity: all atom structure validation for macromolecular crystallography. *Acta Cryst.* **D66,** 12–21 (2010).

182. Vaguine, a a, Richelle, J. & Wodak, S. J. SFCHECK: a unified set of procedures for evaluating the quality of macromolecular structure-factor data and their agreement with the atomic model. *Acta Crystallogr. D. Biol. Crystallogr.* **55,** 191–205 (1999).

183. Karplus, P. A. & Diederichs, K. Linking Crystallographic Model and Data Quality. 1030–1033 (2012).

184. Evans, G., Axford, D., Waterman, D. & Owen, R. L. Macromolecular Microcrystallography. *Crystallogr. Rev.* **17,** 105–142 (2011).

185. Smith, A. G. & Tom, L. research papers Threonine 57 is required for the post-translational activation of Escherichia coli aspartate a -decarboxylase research papers. 1166–1172 (2014). doi:10.1107/S1399004713034275

186. Clayden, J., Greeves, N., Warren, S. & Wothers, P. *Organic chemistry*. (Oxford University Press, 2001).

187. Diederichs, K. & Karplus, P. A. Better models by discarding data? *Acta Cryst* **D69,** 1215–1222 (2013).

188. Brock A. and Zare R.,, R. N. Characterization of a Hadamard transform time-of-flight mass spectrometer. *Rev. Sci. Instrum.* **71,** 1306 1318 (2000).

189. Fernandez, F. *et al.* Hadamard Transform Time-of-Flight Mass Spectrometry: A High-Speed Detector for Capillary-Format Separations. *Anal. Chem.* **74,** 1611 (2002).

190. Harwit, M. & Sloane, N. J. A. *Hadamard Transform Optics*. (Academic Press, 1979).

191. Freeman, R. & Kupˇ, E. New methods for fast multidimensional NMR. 101–113 (2003).

192. Brunswick, N. Application of the Hadamard Transform to NMR Spectrometry with Pseudonoise Excitation. **63,** 44–63 (1974).

193. Sloane, N. J. & Harwit, M. Masks for Hadamard transform optics, and weighing designs. *Appl. Opt.* **15,** 107–14 (1976).

194. Waterman, D. SUMSUB. *Pers. Commun.*

195. Evans, P. R. & Garib, N. research papers How good are my data and what is the resolution ? research papers. 1204–1214 (2013). doi:10.1107/S0907444913000061

196. Dodson, E. J. & Terry, H. MTZutils. at <http://www.ccp4.ac.uk/html/mtzutils.html>

197. R Core Team. R: A Language and Environment for Statistical Computing. (2014). at <http://www.r-project.org>

198. Warren, M. >. *Pers. Commun.*

199. Holton, J. M. & Frankel, K. A. The minimum crystal size needed for a complete diffraction data set. *Acta Cryst* **D66,** 393–408 (2010).

200. Sun, C., Portmann, G., Hertlein, M., Kirz, J. & Robin, D. S. A new operation mode for synchrotron light sources. *Phys. Rev. Lett.* **109,** 264801 (2012).

201. Graceffa, R. *et al.* Sub-millisecond time-resolved SAXS using a continuous-flow mixer and X-ray microbeam. 820–825 (2013). doi:10.1107/S0909049513021833

202. Nesmelov, Y. E. *et al.* Structural kinetics of myosin by transient time-resolved FRET. *Proc. Natl. Acad. Sci. U. S. A.* **108,** 1891–6 (2011).

203. Batson, P. E. Unlocking the time resolved nature of electron microscopy. *Proc. Natl. Acad. Sci. U. S. A.* **108,** 3099–100 (2011).

204. Zewail, A. H. Four-dimensional electron microscopy. *Science* **328,** 187–93 (2010).

205. Barnard, D. *et al.* Time Resolved Cryo-Electron Microscopy Of Ribosome Assembly using Microfluidic Mixing. *Microsc. Microanal.* **15,** 942–943 (2009).

206. Selenko, P. *et al.* In situ observation of protein phosphorylation by high-resolution NMR spectroscopy. *Nat. Struct. Mol. Biol.* **15,** 321–9 (2008).

207. Bartlett, A. I. & Radford, S. E. An expanding arsenal of experimental methods yields an explosion of insights into protein folding mechanisms. **16,** 582–588 (2009).

208. Tonge, P. J. *et al.* Characterization of trans- and cis-5-methylthienylacryloyl chymotrypsin using Raman difference spectroscopy, NMR, and kinetics: carbonyl environment and reactivity. *J. Am. Chem. Soc.* **115,** 8757–8762 (1993).

209. Szöllősi, D. *et al.* Discrete molecular dynamics can predict helical prestructured motifs in disordered proteins. *PLoS One* **9,** e95795 (2014).

210. Guvench, O. & MacKerell Jr., A. D. in *Mol. Model. proteins* 63–88 (Humana Press, 2008).

211. Shalashilin, D. V, Beddard, G. S., Paci, E. & Glowacki, D. R. Peptide kinetics from picoseconds to microseconds using boxed molecular dynamics: Power law rate coefficients in cyclisation reactions. *J. Chem. Phys.* **137,** (2012).

212. Owen, R. L. *et al.* Outrunning free radicals in room-temperature macromolecular crystallography. *Acta Cryst* **D68,** 810–818 (2012).

213. Van Der Spoel, D. *et al.* GROMACS: fast, flexible, and free. *J. Comput. Chem.* **26,** 1701–18 (2005).

214. Reddy, A. D., Suh, S. B., Ghaffari, R. & Singh, N. J. Bioinformatics Analysis of SARS Proteins and Molecular Dynamics Simulated Structure of an Alpha-helix Motif. **24,** 899–900 (2003).

215. Kortemme, T., Kim, D. E. & Baker, D. Computational alanine scanning of protein-protein interfaces. *Sci. STKE* **2004,** pl2 (2004).

216. Kabsch, W. XDS. *Acta Crystallogr. Sect. D Biol. Crystallogr.* **66,** 125–132 (2010).

217. Evans, P. R. An introduction to data reduction: space-group determination, scaling and intensity statistics. *Acta Cryst Crystallogr. Sect. D* **67,** 282–292 (2011).

218. Paithankar, K. S. & Garman, E. F. Know your dose: RADDOSE. *Acta Cryst* **D66,** 381–388 (2010).

219. Weiss, M. S. & Hilgenfeld, R. On the use of the merging {\it R} factor as a quality indicator for X-ray data. *J. Appl. Crystallogr.* **30,** 203–205 (1997).

220. Weiss, M. S. Global indicators of X-ray data quality. *J. Appl. Crystallogr.* **34,** 130–135 (2001).

221. Howell, L. & Smith, D. Normal probability analysis. *J. Appl. Cryst* **25,** 81–86 (1992).

Appendices

1.1 Bacterial Media

1.1.1 LB

LB Broth, Miller (Sigma-Aldrich) was prepared by dissolving 25 g of the broth powder in 1 Litre of milliQ water. The solution was autoclaved at 121 °C and allowed to cool before use. Solid media was prepared by the addition of 15 g /L agar.

1.1.2 Autoinduction Media

Reagent	**Amount per L**
Yeast Extract	5 g
Tryptone	10 g
50x Salts	20 mL
$MgCl_2$	0.4 mg
1000x Metals	200 μL
50% Glycerol w/v	8 mL
25% Glucose *w/v*	2 mL
Lactose	2 g

1.2 Purification Buffers

1.2.1 Lysis Buffer

Reagent	Concentration
Potassium Phosphate buffer pH 7.5	50 mM
NaCl	300 mM
Imidazole	10 mM

1.2.2 Wash Buffer

Reagent	Concentration
Potassium Phosphate buffer pH 7.5	50 mM
NaCl	300 mM
Imidazole	50 mM

1.2.3 Elution Buffer

Reagent	Concentration
Potassium Phosphate buffer pH 7.5	50 mM
NaCl	300 mM
Imidazole	250 mM

1.2.4 High Imidazole Elution Buffer

Reagent	Concentration
Potassium Phosphate buffer pH 7.5	50 mM
NaCl	300 mM
Imidazole	500 mM
TCEP (Tris(2-carboxyethyl)phosphine)	1 mM

1.3 SDS-Page Buffers and Gel

Tris-tricine PAGE was carried out using the following materials, the electrophoresis was run at 35 mA for 3 hours.

1.3.1 Gel Buffer

Reagent	Concentration
Tris pH 8.45	3 M
SDS (Sodium dodecyl sulfate)	0.3% w/v

1.3.2 Cathode Running Buffer

Reagent	Concentration
Tris pH 8.25	0.1 M
Tricine	0.1 M
SDS	0.1 % w/v

1.3.3 Anode Running Buffer

Reagent	Concentration
Tris pH 8.90	0.2 M

1.3.4 Stacking Gel

Reagent	Volume
Gel Buffer	3.1 mL
30% w/v bis-Acrylamide	1.66 mL
milliQ H_2O	7.74 mL
25% w/v APS	100 μL
TEMED	10 μL

1.3.5 Separating Gel (10%)

Reagent	**Volume**
Glycerol	2.52 mL
Gel Buffer	5 mL
30% w/v bis-Acrylamide	5 mL
milliQ H_2O	2.48 mL
25% w/v APS	100 μL
TEMED	10 μL

1.3.6 SDS Loading Buffer

Reagent	Concentration
Tris-HCL pH 6.8	50 mM
SDS	2 %
Glycerol	10 %
β-mercaptoethanol	1 %
EDTA	12.5 mM
Bromophenol blue	0.02 %

1.3.7 Staining Solution

Reagent	**Volume**
Coomassie blue R350	1 mL
Methanol	400 mL
milliQ H_2O	500 mL
Acetic Acid	100 mL

1.3.8 Destaining Solution

Reagent	Volume
Methanol	400 mL
milliQ H_2O	500 mL
Acetic Acid	100 mL

1.4 Stock Crystallization Buffers

The following solutions were prepared as stocks, for use in the crystallisation screens described in section 4.3.3.

Ammonium Sulfate 3M

Tris 1M

Sodium Citrate 1M

2 HATRX Results tables

Time point	1	2	3	4	5	6	7	8	9	10	11	12	13	14
Resolution (Å)	45.8-1.80 (1.84-1.80)													
Unit cell	*a*=57.9 Å, *b*=57.9 Å, *c*=150.2 Å, α=90°, β=90°, γ=90°													
R_{merge} (%)	6.7 (8.7)	6.6 (8.2)	6.6 (9.2)	6.7 (8.8)	6.5 (8.6)	6.6 (8.4)	6.3 (8.4)	6.4 (7.9)	6.4 (8.9)	6.4 (9.0)	6.9 (9.0)	6.2 (9.1)	6.4 (9.0)	6.2 (9.1)
$R_{p.i.m.}$ (%)	5.3 (7.1)	5.2 (6.6)	5.2 (7.5)	5.3 (7.1)	5.1 (6.9)	5.2 (6.7)	5.0 (6.8)	5.1 (6.8)	5.0 (7.1)	5.0 (7.3)	5.2 (7.3)	4.9 (7.4)	5.1 (7.4)	4.9 (7.3)
# reflections	37901 (2053)	38072 (2047)	38096 (2060)	38057 (2030)	38320 (2073)	38147 (2074)	38169 (2046)	38359 (2067)	38320 (2065)	38479 (2075)	37112 (1986)	38427 (2039)	37239 (1953)	38581 (1940)
# unique reflections	20148 (1120)	20171 (1113)	20177 (1127)	20175 (1103)	20236 (1122)	20194 (1125)	20213 (1107)	20235 (1117)	20248 (1116)	20279 (1120)	20076 (1108)	20309 (1112)	20124 (1096)	20358 (1061)
<I>/sd<I>	29.8 (27.7)	31.5 (34.6)	26.2 (25.5)	27.1 (26.7)	22.0 (21.1)	26.7 (26.4)	22.9 (22.0)	24.9 (17.8)	18.7 (15.8)	27.0 (19.5)	24.8 (21.5)	26.1 (24.2)	20.5 (17.9)	21.5 (21.1)
CC(1/2)	0.982 (0.975)	0.983 (0.978)	0.982 (0.970)	0.984 (0.977)	0.984 (0.978)	0.983 (0.979)	0.985 (0.975)	0.988 (0.976)	0.988 (0.975)	0.988 (0.971)	0.985 (0.970)	0.988 (0.974)	0.989 (0.974)	0.989 (0.971)
Completeness (%)	83.2 (79.9)	83.2 (79.1)	83.2 (79.9)	83.1 (78.6)	83.5 (80.1)	83.3 (80.3)	83.3 (78.9)	83.4 (79.6)	83.4 (79.6)	83.6 (79.8)	82.7 (78.4)	83.6 (78.8)	82.9 (77.3)	83.5 (74.9)

Multiplicity	1.9 (1.8)	1.9 (1.8)	1.9 (1.8)	1.9 (1.8)	1.9 (1.8)	1.9 (1.8)	1.9 (1.8)	1.9 (1.9)	1.9 (1.9)	1.9 (1.9)	1.8 (1.8)	1.9 (1.8)	1.9 (1.8)	1.9 (1.8)
Absorbed Dose (MGy)	1.08	2.16	3.24	4.32	5.40	6.48	7.56	8.64	9.72	10.80	11.88	12.96	14.04	15.12

Table S1, continued: Scaling statistics for the reference data. 31 crystals were used, data were indexed and integrated using XDS[216] and then scaled using AIMLESS [217]. The absorbed dose at each time point was calculated using RADDOSE[218]. Numbers in parentheses report on the highest resolution shell. R_{merge}[219] & $R_{p.i.m.}$[220] were calculated over all reflections as[219]

$$R_{merge} = \sum_{hkl} \left| I_{hkl} - \langle I_{hkl} \rangle \right| / \sum_{hkl} \langle I_{hkl} \rangle \quad \text{and} \quad R_{p.i.m.} = \sum_{hkl} \left(\sqrt{\frac{1}{n_{hkl} - 1}} \right) \sum_{hkl} \left| I_{hkl} - \langle I_{hkl} \rangle \right| / \sum_{hkl} \langle I_{hkl} \rangle .$$

Time point	15	16	17	18	19	20	21	22	23	24	25	26	27
Resolution (Å)	45.8-1.80 (1.84-1.80)												
Unit cell	*a*=57.9 Å, *b*=57.9 Å, *c*=150.2 Å, α=90°, β=90°, γ=90°												
R_{merge} (%)	6.2 (9.0)	6.4 (9.4)	6.2 (9.2)	6.2 (9.3)	6.2 (9.4)	6.4 (9.6)	6.2 (9.7)	6.3 (9.9)	6.1 (9.6)	6.1 (9.4)	6.3 (10.0)	6.5 (10.6)	6.3 (9.7)
$R_{p.i.m.}$ (%)	4.9 (7.3)	5.0 (7.6)	4.9 (7.6)	4.9 (7.5)	4.9 (7.7)	5.0 (7.8)	4.9 (7.8)	4.9 (8.0)	4.9 (7.9)	4.9 (7.7)	4.9 (8.2)	5.2 (8.6)	5.0 (7.7)
# reflections	37192 (1866)	38497 (1910)	38490 (1888)	38528 (1902)	37284 (1836)	38564 (1902)	38664 (1907)	38630 (1939)	37373 (1839)	37395 (1863)	38726 (1925)	37605 (1828)	38746 (1877)
# unique reflections	20134 (1053)	20350 (1049)	20333 (1037)	20356 (1046)	20172 (1034)	20378 (1046)	20391 (1049)	20395 (1066)	20197 (1039)	20207 (1055)	20392 (1060)	20238 (1025)	20418 (1031)
<I>/sd<I>	34.6 (21.9)	25.3 (24.2)	21.0 (18.9)	24.0 (17.1)	22.6 (21.5)	21.3 (14.7)	21.8 (17.8)	21.1 (19.7)	27.7 (16.5)	24.9 (16.2)	26.2 (19.2)	18.1 (11.6)	26.5 (19.1)
CC(1/2)	0.988 (0.971)	0.989 (0.970)	0.989 (0.968)	0.990 (0.969)	0.989 (0.970)	0.987 (0.968)	0.987 (0.963)	0.987 (0.973)	0.991 (0.970)	0.990 (0.972)	0.988 (0.968)	0.989 (0.968)	0.988 (0.974)
Completeness	82.7	83.5	83.4	83.5	82.8	83.6	83.6	83.7	82.9	83.0	83.7	83.1	83.7

(%)	(74.3)	(74.3)	(73.4)	(74.1)	(73.2)	(74.1)	(74.2)	(75.4)	(73.5)	(74.5)	(74.9)	(72.5)	(72.8)
Multiplicity	1.8 (1.8)	1.9 (1.8)	1.9 (1.8)	1.9 (1.8)	1.8 (1.8)	1.9 (1.8)	1.9 (1.8)	1.9 (1.8)	1.9 (1.8)	1.9 (1.8)	1.9 (1.8)	1.9 (1.8)	1.9 (1.8)
Absorbed Dose (MGy)	16.20	17.28	18.36	19.44	20.52	21.60	22.68	23.76	24.84	25.92	27.00	28.08	29.16

Table S1, continued: Scaling statistics for the reference data.

Image	1	2	3	4	5	6	7	8	9
Resolution (Å)	57.8-1.79 (1.83-1.79)								
Unit cell	*a*=57.8 Å, *b*=57.8 Å, *c*=149.9 Å, α=90°, β=90°, γ=90°								
R_{merge} (%)	10.6 (15.6)	10.5 (15.5)	10.4 (15.6)	10.5 (15.6)	10.4 (15.4)	10.2 (15.4)	10.1 (15.3)	10.1 (15.7)	10.0 (15.7)
$R_{p.i.m.}$ (%)	6.0 (8.8)	5.9 (8.7)	5.9 (8.9)	5.9 (8.8)	5.9 (8.7)	5.8 (8.8)	5.8 (8.8)	5.7 (9.1)	5.7 (9.0)
# reflections	87000 (4212)	87211 (4279)	87222 (4143)	87052 (4368)	86615 (4168)	86215 (4107)	85853 (4090)	85499 (3854)	85432 (3985)
# unique reflections	23569 (1196)	23588 (1215)	23604 (1183)	23602 (1241)	23603 (1201)	23597 (1200)	23581 (1206)	23582 (1165)	23557 (1183)
<I>/sd<I>	15.6 (11.2)	39.1 (25.4)	15.6 (10.3)	18.5 (11.8)	19.0 (12.9)	15.1 (9.7)	19.7 (9.2)	19.2 (15.4)	23.3 (12.2)
CC(1/2)	0.986 (0.955)	0.987 (0.957)	0.987 (0.943)	0.987 (0.955)	0.987 (0.953)	0.988 (0.956)	0.988 (0.953)	0.988 (0.951)	0.989 (0.951)
Completeness (%)	96.4 (85.0)	96.4 (86.3)	96.3 (83.6)	96.5 (88.1)	96.3 (85.0)	96.2 (84.8)	96.2 (85.3)	96.0 (82.3)	96.1 (83.7)

Multiplicity	3.7 (3.5)	3.7 (3.5)	3.7 (3.5)	3.7 (3.5)	3.7 (3.5)	3.7 (3.4)	3.6 (3.4)	3.6 (3.3)	3.6 (3.4)
Absorbed Dose (MGy)	3.24	6.48	9.72	12.96	16.2	19.44	22.68	25.92	29.16

Table S2: Scaling statistics for the *n*=3 HATRX data, images encoded with [1 0 1]. 72 crystals were used, data were indexed and integrated using XDS[216] and then scaled using AIMLESS[217]. The absorbed dose at each time point was calculated using RADDOSE[218]. Note, this experiment mimics one in which the HATRX encoding is done on the detector. Therefore, even though each HATRX image contains information from only 2 probe pulses, the crystal was exposed over all three pulses. Numbers in parentheses report on the highest resolution shell. R_{merge} & $R_{p.i.m.}$ were calculated over all reflections as in Table S3.

Image	1	2	3	4	5	6	7	8	9
Resolution (Å)	57.8-1.79 (1.83-1.79)								
Unit cell	*a*=57.8 Å, *b*=57.8 Å, *c*=149.9 Å, α=90°, β=90°, γ=90°								
R_{merge} (%)	10.7 (13.9)	10.6 (14.0)	10.5 (13.8)	10.5 (13.9)	10.4 (14.0)	10.2 (14.1)	10.2 (14.2)	10.1 (14.3)	10.1 (15.0)
$R_{p.i.m.}$ (%)	5.9 (7.8)	5.9 (7.8)	5.8 (7.6)	5.8 (7.7)	5.7 (7.8)	5.6 (7.8)	5.6 (8.0)	5.6 (8.0)	5.6 (8.4)
# reflections	88218 (3731)	88539 (3839)	88706 (3200)	88521 (3235)	88443 (3256)	88336 (3230)	87980 (3792)	87794 (3124)	87762 (3795)

# unique reflections	23468 (1061)	23491 (1072)	23517 (915)	23528 (929)	23519 (940)	23511 (933)	23481 (1086)	23482 (931)	23460 (1099)
<I>/sd<I>	19.6 (10.9)	15.6 (9.0)	15.7 (8.6)	17.9 (9.1)	17.0 (10.2)	16.8 (9.6)	19.8 (13.0)	14.5 (7.4)	20.1 (9.9)
CC(1/2)	0.984 (0.962)	0.985 (0.968)	0.985 (0.968)	0.986 (0.968)	0.986 (0.969)	0.987 (0.969)	0.988 (0.966)	0.988 (0.970)	0.988 (0.967)
Completeness (%)	95.3 (74.4)	95.3 (75.1)	94.9 (66.6)	95.0 (67.6)	94.9 (68.4)	94.9 (67.9)	95.3 (76.9)	94.8 (67.9)	95.2 (77.1)
Multiplicity	3.8 (3.5)	3.8 (3.6)	3.8 (3.5)	3.8 (3.5)	3.8 (3.5)	3.8 (3.5)	3.7 (3.5)	3.7 (3.4)	3.7 (3.5)
Absorbed Dose (MGy)	3.24	6.48	9.72	12.96	16.2	19.44	22.68	25.92	29.16

Table S2 continued: Scaling statistics for the *n*=3 HATRX data, images encoded with [1 1 0]. 76 crystals were used.

Image	1	2	3	4	5	6	7	8	9
Resolution (Å)	57.8-1.79 (1.83-1.79)								
Unit cell	*a*=57.8 Å, *b*=57.8 Å, *c*=149.9 Å, α=90°, β=90°, γ=90°								
R_{merge} (%)	10.2 (13.9)	10.2 (13.8)	10.1 (14.2)	10.0 (14.0)	9.9 (14.1)	9.9 (14.4)	9.9 (14.9)	9.9 (15.0)	9.8 (14.9)
$R_{p.i.m.}$ (%)	5.8 (8.1)	5.8 (8.0)	5.8 (8.3)	5.7 (8.2)	5.7 (8.3)	5.7 (8.5)	5.7 (8.8)	5.7 (8.9)	5.6 (8.7)
# reflections	83487 (3901)	83586 (3947)	83512 (3846)	83251 (3854)	82913 (3874)	82468 (3826)	82213 (3649)	82163 (3588)	82153 (3522)
# unique reflections	23528 (1184)	23523 (1193)	23531 (3846)	23523 (1178)	23517 (1186)	23488 (1182)	23489 (1155)	23474 (1131)	23467 (1119)
<I>/sd<I>	16.0 (11.3)	16.1 (12.6)	14.6 (10.1)	15.2 (10.3)	14.7 (8.9)	17.0 (13.0)	14.0 (8.2)	22.4 (15.3)	19.8 (13.4)
CC(1/2)	0.987 (0.963)	0.987 (0.961)	0.987 (0.962)	0.987 (0.962)	0.988 (0.963)	0.988 (0.956)	0.988 (0.956)	0.988 (0.953)	0.989 (0.958)
Completeness (%)	96.0 (83.9)	96.0 (84.3)	95.9 (83.0)	95.8 (83.6)	95.8 (84.1)	95.7 (83.8)	95.5 (81.0)	95.4 (79.3)	95.4 (78.4)
Multiplicity	3.5 (3.3)	3.6 (3.3)	3.5 (3.3)	3.5 (3.3)	3.5 (3.3)	3.5 (3.2)	3.5 (3.2)	3.5 (3.2)	3.5 (3.1)

Absorbed Dose (MGy)	3.24	6.48	9.72	12.96	16.2	19.44	22.68	25.92	29.16

Table S2 continued: Scaling statistics for the *n*=3 HATRX data, images encoded with [0 1 1]. 70 crystals were used.

Resolution (Å)	W_{rel}1	W_{rel} 2	W_{rel} 3	W_{rel} 4	W_{rel} 5	W_{rel} 6	W_{rel} 7	W_{rel} 8	W_{rel} 9	W_{rel} 10	W_{rel} 11	W_{rel} 12	W_{rel} 13	W_{rel} 14	W_{rel} 15	W_{rel} 16	W_{rel} 17	W_{rel} 18
11.20	0.020	0.001	0.024	0.006	0.002	0.070	0.007	0.001	0.035	0.017	0.011	0.099	0.205	0.009	0.043	0.036	0.051	0.007
6.60	0.009	0.056	0.006	0.008	0.001	0.007	0.023	0.011	0.008	0.000	0.004	0.006	0.014	0.001	0.008	0.009	0.035	0.005
5.10	0.028	0.016	0.007	0.001	0.000	0.004	0.003	0.042	0.033	0.000	0.014	0.009	0.002	0.004	0.006	0.003	0.005	0.010
4.30	0.025	0.000	0.038	0.001	0.003	0.003	0.013	0.003	0.058	0.019	0.001	0.068	0.005	0.007	0.012	0.009	0.003	0.120
3.78	0.008	0.004	0.022	0.006	0.003	0.005	0.005	0.011	0.004	0.003	0.000	0.005	0.004	0.005	0.006	0.000	0.001	0.007
3.41	0.020	0.004	0.006	0.000	0.007	0.011	0.001	0.001	0.007	0.016	0.014	0.017	0.009	0.056	0.019	0.005	0.019	0.009
3.15	0.002	0.008	0.015	0.000	0.000	0.016	0.011	0.006	0.021	0.005	0.001	0.009	0.000	0.000	0.010	0.002	0.002	0.024
2.92	0.015	0.006	0.015	0.008	0.001	0.011	0.001	0.003	0.014	0.004	0.001	0.013	0.009	0.010	0.007	0.000	0.005	0.033
2.75	0.007	0.002	0.022	0.011	0.015	0.014	0.006	0.003	0.015	0.000	0.018	0.034	0.001	0.001	0.020	0.003	0.009	0.013
2.60	0.001	0.003	0.021	0.004	0.002	0.023	0.089	0.005	0.010	0.002	0.002	0.011	0.003	0.002	0.009	0.010	0.001	0.011
2.47	0.000	0.007	0.010	0.000	0.001	0.013	0.006	0.004	0.009	0.004	0.000	0.008	0.005	0.009	0.018	0.003	0.000	0.008
2.36	0.009	0.005	0.026	0.043	0.003	0.011	0.000	0.000	0.012	0.001	0.004	0.011	0.002	0.001	0.008	0.013	0.005	0.013
2.26	0.005	0.004	0.011	0.002	0.001	0.021	0.001	0.012	0.016	0.022	0.005	0.009	0.000	0.000	0.016	0.011	0.005	0.020
2.18	0.017	0.000	0.013	0.000	0.001	0.016	0.000	0.002	0.019	0.006	0.001	0.011	0.007	0.002	0.020	0.004	0.004	0.020
2.10	0.000	0.010	0.008	0.001	0.000	0.018	0.000	0.001	0.012	0.001	0.001	0.015	0.009	0.007	0.012	0.013	0.000	0.014
2.04	0.005	0.000	0.017	0.002	0.004	0.025	0.004	0.003	0.011	0.005	0.003	0.013	0.007	0.001	0.018	0.008	0.010	0.011
1.97	0.000	0.000	0.015	0.000	0.004	0.013	0.002	0.002	0.017	0.014	0.000	0.030	0.000	0.002	0.019	0.000	0.000	0.032
1.91	0.004	0.005	0.015	0.000	0.000	0.032	0.000	0.008	0.015	0.001	0.005	0.017	0.002	0.010	0.019	0.017	0.002	0.015
1.86	0.000	0.008	0.032	0.009	0.006	0.027	0.001	0.006	0.020	0.001	0.004	0.023	0.002	0.005	0.016	0.003	0.001	0.024

1.81	0.001	0.011	0.015	0.001	0.007	0.008	0.008	0.002	0.019	0.010	0.007	0.014	0.002	0.004	0.014	0.002	0.002	0.020

Table S3: Weighted Rfactors (W_{rel}) by resolution shell[221] for the comparison of the reference data (R) at each time point with the HATRX data.

$$W_{rel} = \frac{\sum \frac{\left|f_R^2 - f_M^2\right|}{\sigma_R^2} + \frac{\left|f_H^2 - f_M^2\right|}{\sigma_H^2}}{\sum \left(\frac{f_R}{\sigma_R}\right)^2 + \left(\frac{f_H}{\sigma_H}\right)^2}, \text{ where } f_M^2 = \left[\left(\frac{f_R}{\sigma_R}\right)^2 + \left(\frac{f_H}{\sigma_H}\right)^2\right] / \left(\frac{1}{\sigma_R^2} + \frac{1}{\sigma_H^2}\right), \ \sigma_R = 2 f_R \sigma_{f_R} \text{ and } \sigma_H = 2 f_H \sigma_{f_H} .$$

Resolution (Å)	W_{rel} 19	W_{rel} 20	W_{rel} 21	W_{rel} 22	W_{rel} 23	W_{rel} 24	W_{rel} 25	W_{rel} 26	W_{rel} 27
11.20	0.025	0.005	0.005	0.002	0.016	0.004	0.007	0.008	0.012
6.60	0.023	0.006	0.002	0.000	0.028	0.007	0.014	0.007	0.012
5.10	0.002	0.015	0.014	0.002	0.003	0.008	0.004	0.009	0.006
4.30	0.003	0.005	0.016	0.005	0.011	0.003	0.015	0.000	0.010
3.78	0.004	0.013	0.013	0.001	0.003	0.010	0.010	0.001	0.007
3.41	0.001	0.017	0.010	0.004	0.002	0.018	0.006	0.023	0.026
3.15	0.009	0.001	0.009	0.000	0.007	0.012	0.008	0.014	0.013
2.92	0.001	0.007	0.008	0.001	0.005	0.010	0.003	0.003	0.004
2.75	0.003	0.000	0.020	0.000	0.004	0.015	0.000	0.011	0.009
2.60	0.000	0.001	0.013	0.000	0.000	0.015	0.003	0.000	0.016
2.47	0.003	0.009	0.011	0.016	0.012	0.010	0.003	0.010	0.009
2.36	0.000	0.005	0.029	0.003	0.001	0.014	0.017	0.002	0.022
2.26	0.002	0.008	0.013	0.000	0.008	0.016	0.013	0.000	0.017
2.18	0.002	0.001	0.017	0.001	0.001	0.024	0.000	0.010	0.010
2.10	0.002	0.000	0.013	0.005	0.001	0.018	0.002	0.001	0.009
2.04	0.001	0.005	0.014	0.028	0.001	0.022	0.001	0.000	0.010
1.97	0.009	0.006	0.010	0.001	0.000	0.022	0.000	0.001	0.009
1.91	0.000	0.004	0.012	0.001	0.002	0.007	0.002	0.015	0.011
1.86	0.005	0.000	0.027	0.001	0.013	0.014	0.000	0.002	0.014

1.81	0.030	0.007	0.011	0.000	0.000	0.010	0.012	0.004	0.014

Table S3, continued: Weighted Rfactors (W_{rel}) by resolution shell for the comparison of the reference data (R) at each time point with the HATRX data.

Thaumatin refined against HATRX time-point 1

Resolution (Å)	45.9-1.8 (1.85-1.80)
R_{work} (%)	17.4 (18.5)
R_{free} (%)	20.2 (23.2)
Number of atoms	1724
Protein	1549
Ligand	10
Water	165
r.m.s. deviations	
Bond angles (°)	1.950
Bond lengths (Å)	0.021
Average B factors	
Protein (Å^2)	6.88
Ligand (Å^2)	5.35
Water (Å^2)	13.78
Ramachandran Plot	
Allowed regions (%)	98
Generously allowed regions (%)	2
Disallowed regions (%)	0
Cruickshank's DPI (Å)	0.105
PDB Code	4C3C

Table S4: Refinement statistics for thaumatin refined against the HATRX time-point 1 data. HATRX data derived from summed images. Numbers in parentheses represent the highest resolution shell. Ramachandran plots were calculated using MOLPROBITY[181] 5% of reflections were selected randomly as the free set. R_{work} and R_{free} were calculated as $R = \sum \| F_o | - | F_c \| / \sum | F_o |$.